2009

INVESTIGATION OF THERMO-FLUID BEHAVIOR OF A DISH-TYPE CONCENTRATED SOLAR ENERGY SYSTEM

Mo Wang

INVESTIGATION OF THERMO-FLUID BEHAVIOR OF A DISH-TYPE CONCENTRATED SOLAR ENERGY SYSTEM

(Spine title: Investigation of a dish-type solar thermal energy system)

(Thesis format: Monograph)

By

Mo Wang

Graduate Program in Engineering Science
Department of Mechanical & Materials Engineering

A thesis submitted in partial fulfillment
of the requirements for the degree of
Master of Engineering Science

The School of Graduate and Postdoctoral Studies
The University of Western Ontario
London, Ontario

ABSTRACT

A three-dimensional model of parabolic dish-receiver system with argon gas as the working fluid is designed to simulate the thermal performance of the concentrated solar energy system using commercial software FEMAP-TMG. A comprehensive parametric study is conducted to investigate the impact of several geometrical, radiative and operational parameters on the performance of the dish-receiver system. The results show that the aperture size, different inlet/outlet configurations, reflectivity of the parabolic dish, flow rate and working fluids have considerable impacts on the receiver wall and gas temperatures, while the rim angle of the dish, emissivity and absorptivity of the interior wall of the receiver have negligible impacts. An optimal configuration of the system is proposed based on the parametric study.

Keywords: **solar energy, reactor, receiver, parabolic dish, concentrator, radiation, thermal performance, aperture, reflectivity, emissivity, absorptivity, rim angle, argon.**

ACKNOWLEDGMENTS

I would like to express my gratitude to my supervisor, Dr. Kamran Siddiqui, whose patience, support and expertise, added to my graduate experience. His vast knowledge guided me throughout the research and his great assistance in writing reports (i.e., proposals, conference papers, journal papers and this thesis) made me learn a lot more in these two years. I would like to thank the other members of the examination committee, Dr. Chao Zhang, Dr. Roger Khayat and Dr. Rajiv Varma, for taking time out from their busy schedules to serve as my readers and examiners.

Very special thanks go out to Dr. Tutunea-Fatan, O.R., for his great help and suggestions in using NX5.0.

I would also like to thank my family for the support they provided me through my entire life.

TABLE OF CONETENTS

LIST OF TABLES

LIST OF FIGURES

Page

CHAPTER 1: INTRODUCTION

Hydrocarbon-based fuels have been the primary source of energy for mankind for centuries and the energy produced by such fuels accelerated the civilization of mankind. However, during the last few decades there has been an exponential increase in the utilization of energy and the demand for fuels is growing continuously. With the increasing need for energy, there is a growing concern about its over-use and impact on the environment and natural resources. As a result, there is an enhanced interest in seeking alternative energy sources. While the debate on the overall benefits of alternative energy sources on environment continuous between many governmental and industrial quarters, there seems no disagreement on developing alternative energy systems to conserve depleting energy resources. Solar energy is a potential source of alternative energy that has the capability to fulfill the global energy demand as the amount of solar energy incident on the earth is about 15,000 times the energy utilized worldwide [Berman et al., 2006]. Currently, solar energy is utilized as an auxiliary source of energy mainly in small-scale applications, to share the energy requirements with the conventional energy suppliers and hence partially reduces the conventional energy load, for example, photovoltaic cells and solar water heaters. On the other hand, due to the unpredictable nature of the solar radiation availability in different regions and the constantly variable climate conditions, the development of efficient solar energy systems has to take these factors into consideration to ensure reliability of energy supply. This could be achieved by converting solar energy during its availability period into another form of storable energy, which can then be supplied on a continual basis even when the solar energy is not available, for example, during night.

As mentioned above, the rapid depletion of hydrocarbon-based fuels results in growing concern about searching alternative fuels that can fully substitute the conventional fuels. Of the alternative fuels tested or proposed, hydrogen is a potential candidate. There are two advantages of using solar energy for hydrogen production. First, it allows the storage of solar energy in the form of a fuel which makes solar energy a continuous and hence

reliable energy resource. Second, the production of hydrogen is neither hazardous to the environment, nor harmful to humans. Particularly, the production of hydrogen from water-splitting does not involve any process or chemicals with hydrocarbons. Therefore, hydrogen production from water splitting by utilizing solar energy is the best way of the hydrogen production. The present research is a part of a larger project which is focused on the use of solar energy for clean hydrogen production.

1.1 Solar Energy

Generally, the earth receives only 70% of incoming solar radiation at the upper atmosphere and 30% is reflected back to the space (see Fig. 1.1). A portion of this 70%

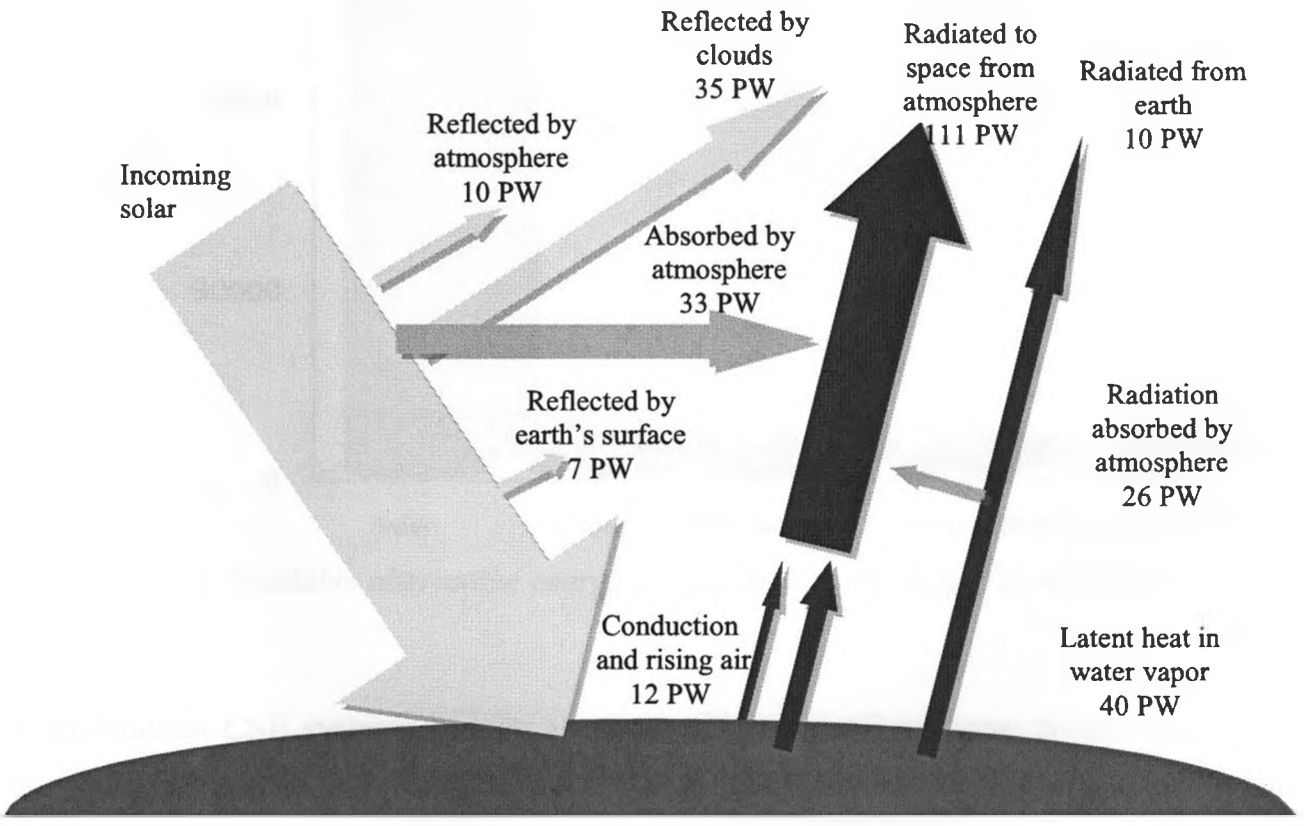

Fig. 1.1: Breakdown of the incoming solar energy (Source: http://en.wikipedia/org)

is absorbed by clouds, oceans and lands. However, the amount of the solar radiation incident on the earth surface is still very large comparing with other renewable energy resources (see Fig. 1.2). It is approximately 15,000 times the energy consumption worldwide annually. Fig. 1.2 also shows the amount of available solar energy is much larger than any other alternative energy resource currently used. Majority of energy in the solar rays is distributed within 250 nm to 1500 nm wavelength radiation at sea level. The spectrum of sunlight on the earth surface is mostly distributed in visible and near-infrared range. Only about 6.4% of the total incident energy on the earth surface is distributed in ultraviolet region; about 48% is contained in the visible region and the rest is contained in the infrared region [Tiwari, 2002].

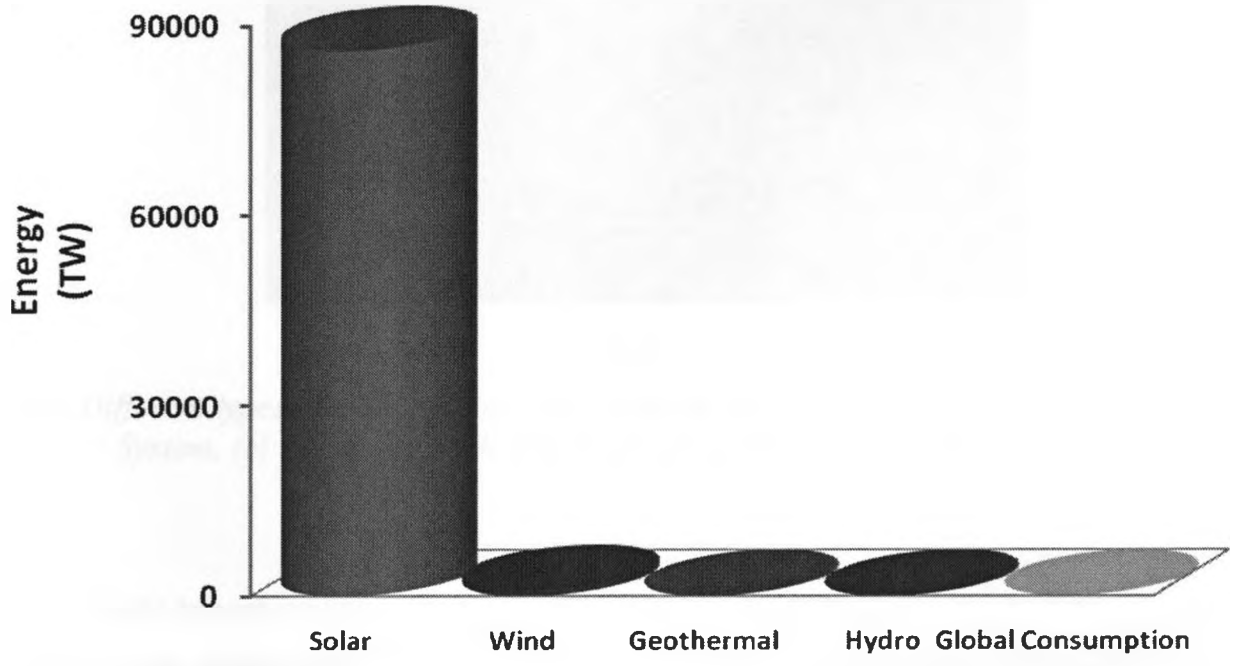

Fig. 1.2: Available alternative energy resources (Source: http://en.wikipedia/org)

Conventional CSE systems consist of three different configurations: parabolic trough, central tower and parabolic dish (see Fig. 1.3). Unlike photovoltaic systems operating on the combination of direct and diffuse solar radiations, the CSE systems only rely on direct beam radiations (or collimated rays). Therefore, intensity of direct solar irradiance has a significant effect on the overall efficiency.

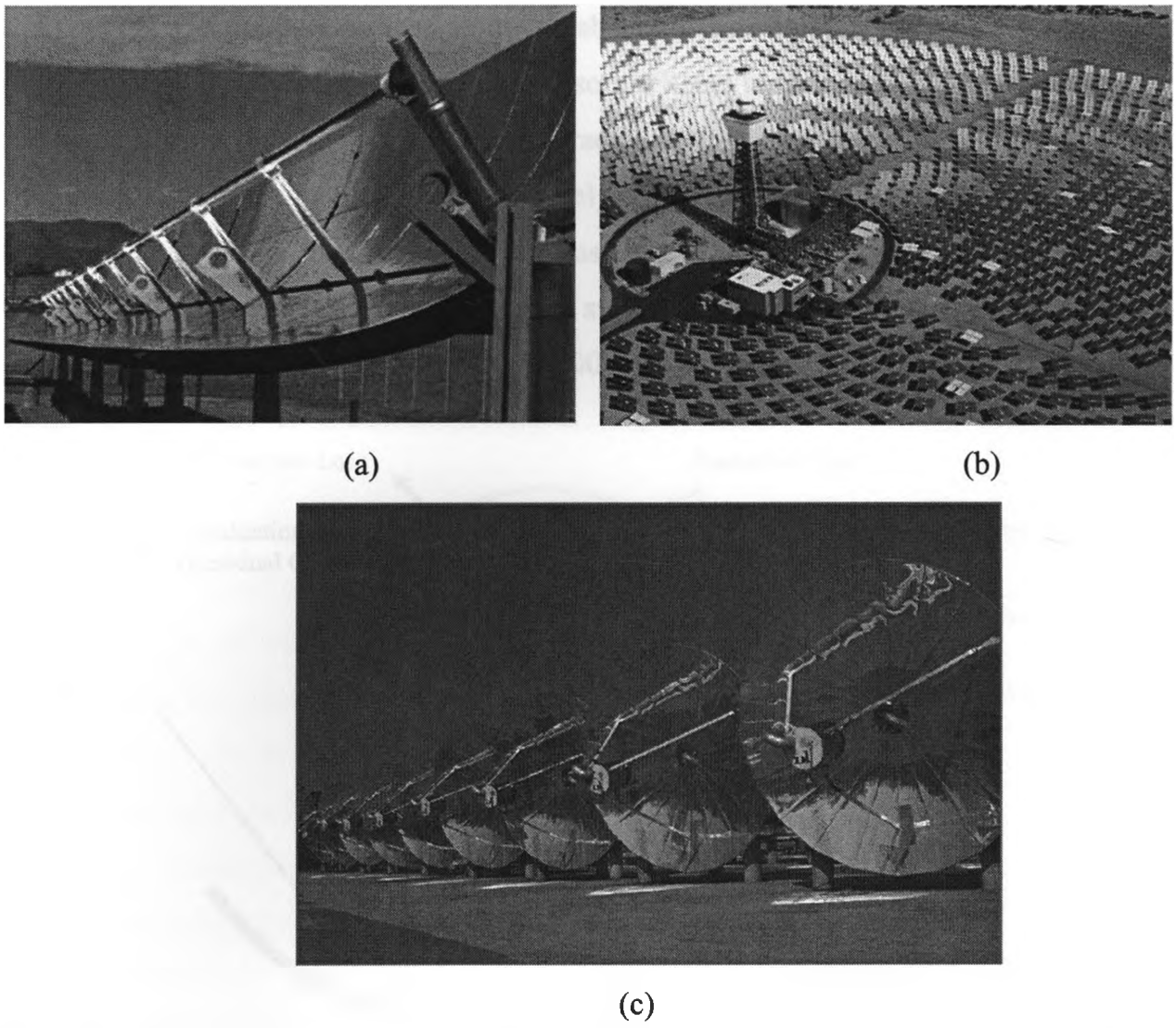

Fig. 1.3: Different types of CSE systems. (a) Parabolic Trough System, (b) Central Tower System, (c) Parabolic Dish System (Source: http://www.nrel.gov/)

1.2.1 Parabolic trough system

Parabolic trough system (see Fig. 1.3a) consists of a large, modular array of single-axis-tracking system with a cylindrical parabolic reflector and a metal tube receiver, also called heat collection element (HCE). A heat transfer fluid is heated up to certain degree as it circulates through the receiver and exchange heat with a series of heat exchangers in the thermal power plant. Heat conversion process occurs in the tubular receiver.

A model of heat loss from an evacuated tubular absorber was developed using a combination of the thermal loss from radiation, convection and conduction (see Fig. 1.4) [Price et al., 2002]. Three heat loss paths are summarized as following: (1) radiation loss

and residual gas conduction loss from the absorber tube outer surface to the evacuated glass envelop. (2) Heat loss from the absorber tube to the surrounding through the metallic bellows. (3) Convection loss and radiation loss from the glass outer surface to the surrounding air and the sky, respectively. Some problems are associated with the operation of parabolic trough system, such as large temperature gradient caused by flow stratification when phase change fluids (e.g. steam) are used, and bending of the absorber tube caused by thermal stress [Price et al., 2002].

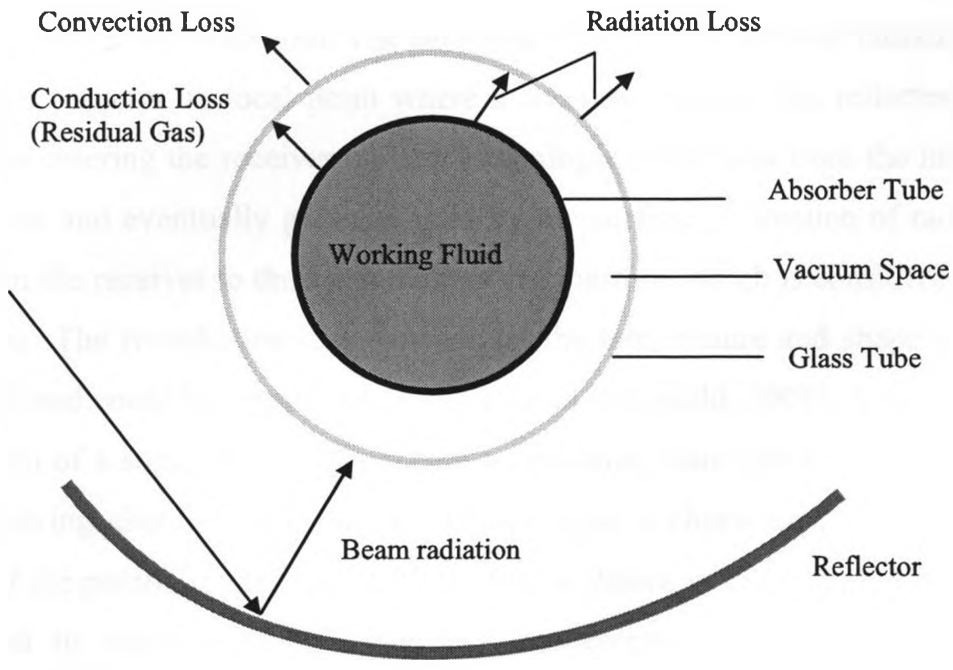

Fig. 1.4: Model of heat loss paths from an evacuated absorber

1.2.2 Central tower system

Central tower system (see Fig. 1.3b) consists of a large array of mirrors fixed to a supporting frame (heliostats) which can track the sun, and a central stationary receiver. The central stationary receiver is used to capture the solar radiation reflected by heliostats. The heliostats are placed in the open area and they perform collectively like a dilute paraboloid. Since the central tower is fixed, all the incident rays are focused on the receiver, so a large amount of absorbed energy can be extracted from the receiver to drive turbines for massive power generation. The advantage of this system is that it does not

need to deliver the working fluid over large distances which results in considerable reduction of heat losses due to convection and conduction, thus, the need for insulation is eliminated. However, larger number of heliostats and thus, larger open area is required. But the concentration ratio is relatively smaller than a parabolic-shape system.

1.2.3 Parabolic dish system

A parabolic-dish system consists of a parabolic dish with mirrors, and a receiver located at the focal point of the paraboloid. The parabolic dish reflects the solar radiation incident on its surface towards its focal point where a receiver captures the reflected radiation. The radiation entering the receiver undergoes multiple reflections from the inner surface of the receiver and eventually gets absorbed by the surface. A fraction of radiation also radiated from the receiver to the surroundings via aperture, which is considered as the re-radiation loss. The re-radiation loss depends on the temperature and shape of the inner receiver wall and could be significant in some cases [Steinfeld, 2001]. A solar receiver is a combination of a solar-capture device and a converter, also called solar reactor. In the process involving chemical reaction, it also serves as a chemical reaction chamber. A schematic of the parabolic-dish type CSE system is shown in Fig. 1.5. A few terms have been defined to characterize parabolic-dish concentrating collectors (see Fig. 1.6). Aperture area (A_a) is the optical opening of the receiver through which the incident solar flux enters the receiver. It can be defined by the physical extremities of the receiver. Acceptance angle ($2\Phi_{rim}$) is the limiting angle over which incident ray path deviates from normal to the aperture plane and still reaches the receiver (see figure 1.6). In a parabolic dish system, rim angle (Φ_{rim}) is half of the acceptance angle. Although a parabolic shape can focus rays to its focal plane or focal point which is parallel to its axis, but sun rays are not parallel. Despite the fact that incoming sun rays have some rays scattered by the aerosols, incoming beam radiation also has a small angle to each other since the sun is not a perfect point source. As a good approximation, sun rays can be assumed to originate from a small disk which subtends the angle β=0.0093 radian. When an ideal paraboloid with focal length f and rim angle Φ_{rim} is aligned to the sun, the focusing image, also

called solar image, at the focal plane forms a circular shape centered at the focal point [Shuai, et al., 2008].

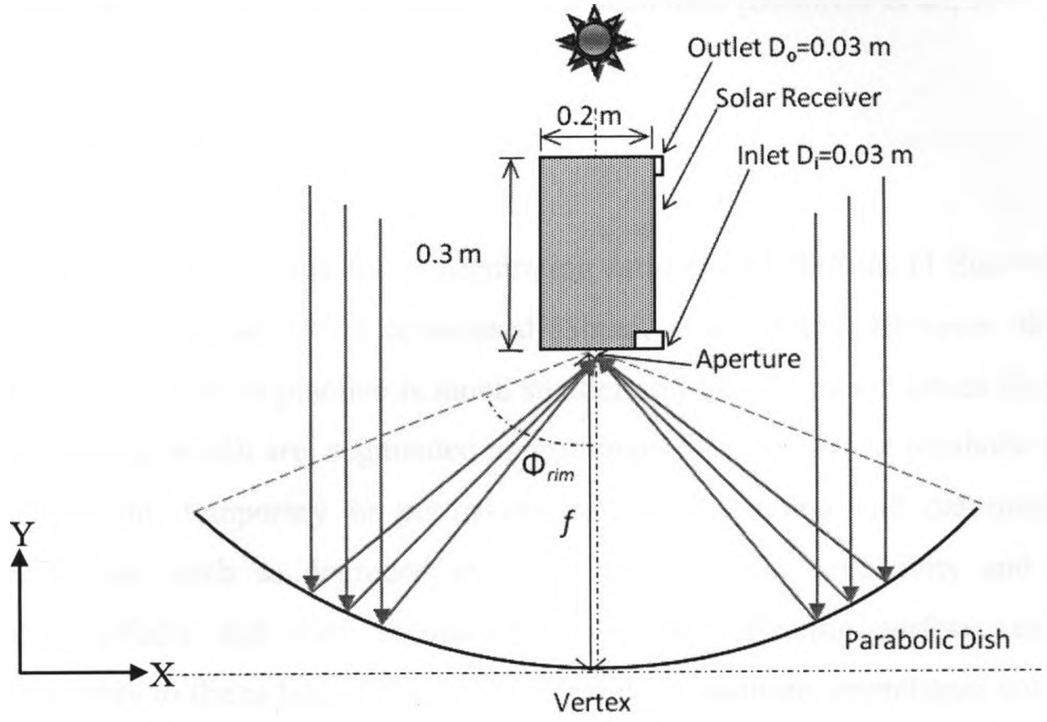

Fig. 1.5: Schematic of the parabolic-dish CSE system

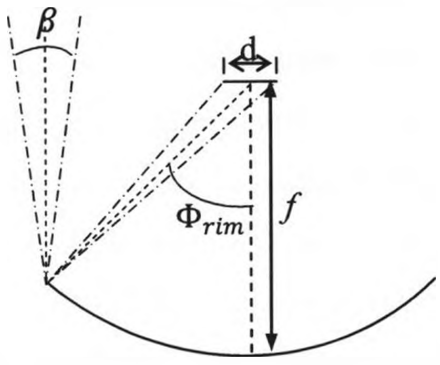

Fig. 1.6: An ideal paraboloid of focal length f and rim angle Φ_{rim}. A circular image is formed at the focal plane.

The diameter of the solar image can be computed as [Steinfeld et al., 2001],

$$d = \frac{f \times \beta}{\cos \Phi_{rim} \, (1+\cos \Phi_{rim})} \tag{1.1}$$

The radiation flux intensity is maximum in the paraxial solar image. The theoretical concentration ratio C at the centre of the focal plane is defined as the ratio of the radiation intensity on the hot spot to the normal beam insolation [Steinfeld et al., 2001],

$$C \approx \frac{4}{\beta^2} \sin^2 \Phi_{rim} \tag{1.2}$$

For instance, theoretically the concentration ratio is 23,000 Suns (1 Sun = 1000 W/m^2) when a rim angle of 45° is considered [Shuai, et al., 2008]. However, the achievable concentration ratio in practice is much smaller and limited by the losses like geometrical imperfections which are, segmented approximation to the perfect parabolic profile, facet misalignment, temporary or permanent structural bending and deformation. Optical imperfection, such as degraded materials causing poor reflectivity and absorptivity, shadow effects and dust accumulation on the reflecting surface, can contribute considerably to the radiation loss in some cases. In addition, operational and surrounding conditions influence the performance of the system by different locations, different seasons and so on. The thermal losses from a paraboloid are primarily radiative and can be reduced by proper controlling of the absorber aperture area. Comparing to parabolic trough system with the concentration ratio of 100 Suns and central tower system with the concentration ratio of 1000 Suns, parabolic dish system can be operated at 10,000 Suns [Steinfeld, 2005]. Therefore, high collection efficiencies can be achieved in a parabolic dish system due to its high concentration ratio. In addition, the quality of thermal energy in this system is high because the receiver has very small opening and could be assumed as a blackbody [Melchior et al., 2008]. Thus, the temperatures inside the receiver are considerably higher than other types of CSE systems. In the hydrogen production process, the parabolic dish has been suggested to have a superior performance because of more concentrated energy and high achievable temperatures comparing to the other two types [Steinfeld, 2005]. Receiver fluid temperature over 2000 K has been suggested by Steinfeld [2005]. Due to the concentration on a smaller volume, the heat losses are also expected to be low. Furthermore, the thermal mass is smaller than flat plate collector and hence transient effects are small. This type of system can help reducing the overall cost

by substituting an expensive large receiver. With these features parabolic dish systems can be used in a variety of applications.

1.3 Applications of Parabolic Dish System

Most of the applications of parabolic dish system involve thermochemical process. This is due to its unique features, mainly attributed to its high achievable temperatures. Nevertheless, conventional industrial processes and civilian applications associated with solar energy, such as solar water heating system, solar air heaters and solar distillation, can still be implemented through parabolic dish systems.

1.3.1 Solar hydrogen production

Several different methods have been proposed to produce hydrogen, for instance, the direct thermal dissociation of H_2O, thermal decomposition of H_2S and H_2O splitting thermochemical cycles.

The direct thermal dissociation of H_2O is also known as thermolysis of water, i.e.

$$H_2O \rightarrow H_2 + \frac{1}{2}O_2 \tag{1.3}$$

This process occurs when a zirconia surface is heated above 2500 K. In order to avoid recombination of the reactants or generating an explosive mixture, the gaseous mixture produced from water thermolysis has to be separated at high temperatures. To achieve secured process of thermolysis, some of the earliest works in solar thermochemistry proposed for separating H_2 are effusion separation [Fletcher et al., 1977] and electrolytic separation [Ihara, 1980]. However, the very high temperatures required by the thermodynamics of the process induces some material problems and can lead to significant reradiation from the solar receiver, and causing lower thermal efficiency [Steinfeld et al., 2001].

The thermal decomposition of H_2S was introduced by Noring et al. [1982]. H_2S is highly toxic industrial product in the sweetening of natural gas and can also be generated in

large quantities during the removal of organically bound sulfur from coal and petroleum. The current process to recover sulfur from H_2S, wastes H_2 by oxidizing it to H_2O and produces low grade process heat. Nevertheless, the amount wasted in the US and Canada alone was estimated to the equivalent of 17 million barrels of gasoline in 1979 [Steinfeld et al., 2001]. In addition, some research studies have shown that many natural gas wells are very rich in H_2S but they are not utilized [Steinfeld et al., 2001]. Therefore, an innovating process that let H_2S to be fed to a solar thermal chemical reactor operating at temperature close to 1800 K and pressures between 0.03 -0.5 bar, could convert this highly toxic material into a useful fuel so that the energy is conserved [Steinfeld et al., 2001]. This process uses sulfide to crack into H_2 and S on hot Al_2O_3 surface, i.e.

$$H_2S \rightarrow H_2 + \frac{1}{2}S_2 \tag{1.4}$$

The gas mixture is then quenched in a water-cooled heat exchanger to produce liquid and eventually solid sulfur [Steinfeld et al., 2001].

Hydrogen can be produced from water-splitting through thermo-chemical process. An efficient thermo-chemical process is the one that utilizes metal oxides and is carried out in the following two-step reaction,

$$M_xO_y \rightarrow xM + \frac{y}{2}O_2 \tag{1.5}$$

$$xM + yH_2O \rightarrow M_xO_y + yH_2 \tag{1.6}$$

The first step, which is the extraction of metal from the metal oxide is endothermic and carried out at very high temperatures [Steinfeld et al. 1998]. The second step is the hydrolysis of metal to obtain hydrogen. The metal oxide used in the reaction is recycled and thus, the net reaction is,

$$H_2O \rightarrow H_2 + \frac{1}{2}O_2 \tag{1.7}$$

Due to the two separate steps in the water-splitting process, H_2 and O_2 gases can be separately recovered. CSE systems which are capable to maintain the conventional high temperature environment for water-splitting process and to achieve high rate hydrogen production are still at the developing stage and have not been fully commercialized yet. Hydrogen production from water is without question a clean process and by combining the benefit of concentrated solar energy system, this technology is promising and can be qualified as one of the most suitable hydrogen production process as both water and solar energy are abundantly available. A simple conceptual picture of this technology is illustrated in Fig. 1.7. The concentrated solar energy is converted into high temperature heat which provides required energy for the metal reduction in reaction (Eq. 1.5) carried out in a solar reactor chamber. The reduced metal then enters another chamber where the water-splitting process occurs at a temperature relatively lower than that for the metal reduction process. The metal oxide produced during reaction (Eq. 1.6) is recycled. Thus, the net reaction in the reactor is the decomposition of water as described in reaction (Eq. 1.7).

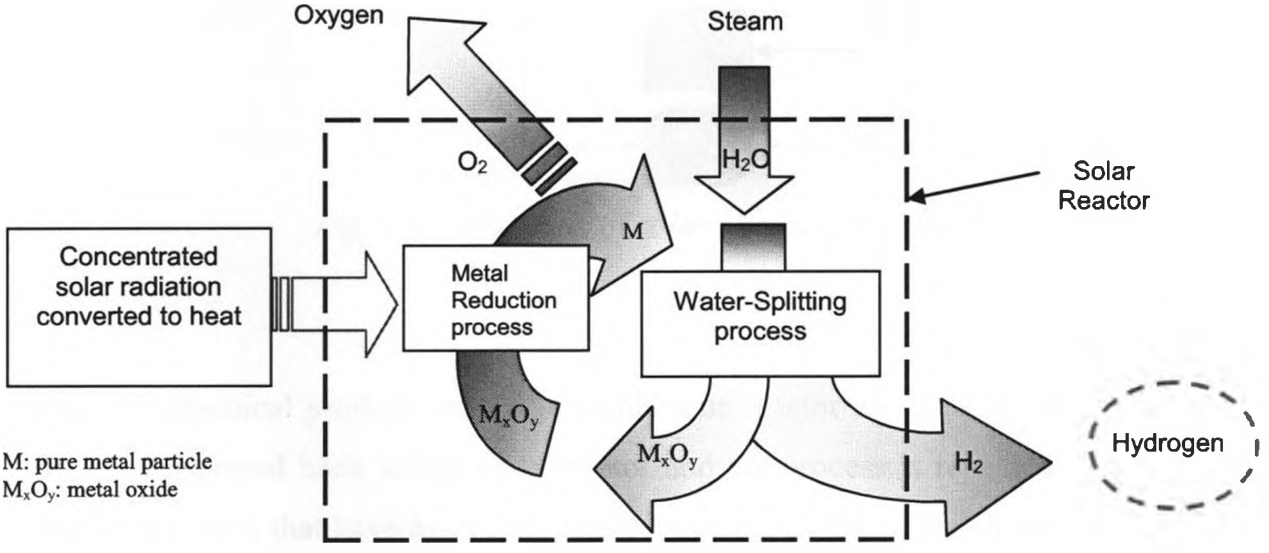

Fig. 1.7: A schematic showing the hydrogen production by water-splitting reaction using a solar energy system.

1.3.2 Solar chemical heat pipes

High temperature process heat from solar radiation is used to drive an endothermic reversible reaction in the solar chemical reactor. At the location where the energy is needed, the exothermic reverse reaction takes place, yielding process heat in an amount equal to the stored solar energy [Steinfeld et al., 2001]. Fig. 1.8 illustrates this energy conversion concept. The products can be stored for long-term usage and transported to distant sites. The high temperature heat can be used to generate electricity through a Rankine cycle.

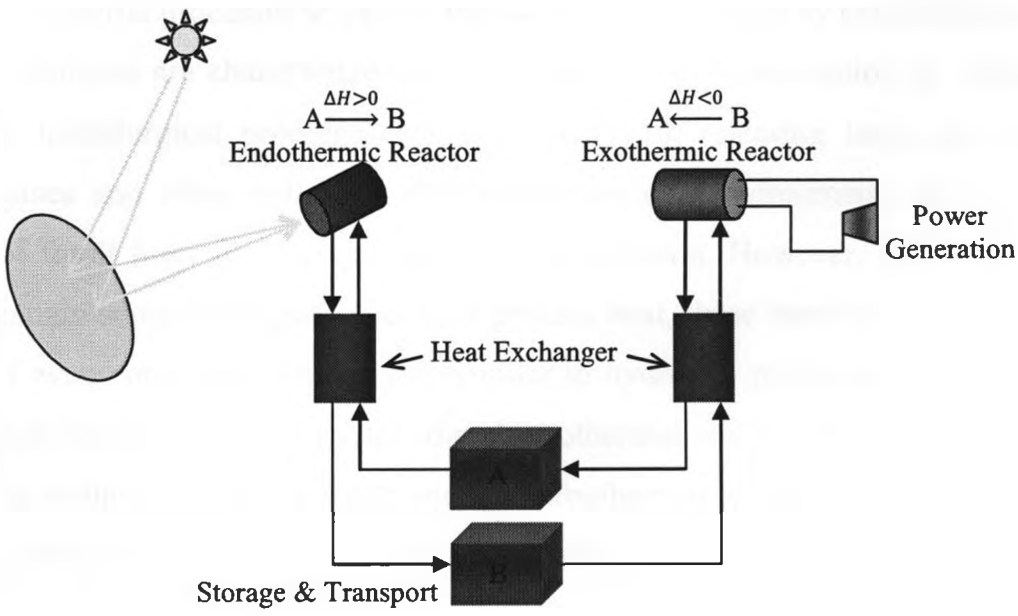

Fig. 1.8: Schematic of solar chemical heat pipes

Since the chemical products from the exothermic reactor are the original reactants, they can be transported back to the solar reactor and the process is repeated. There are two reverse reactions that have been proposed for such application which are CH_4 reforming-methanation and NH_3 dissociation-synthesis [Steinfeld et al., 2001]. Methane is reformed to synthesis gas (syngas), a mixture of primarily H_2 and CO, when using either H_2O or CO_2 as the partial oxidizing agent as follows,

$$CH_4 + H_2O \leftrightarrow 3H_2 + CO \tag{1.8}$$

$$CH_4 + CO_2 \leftrightarrow 2H_2 + 2CO \quad (1.9)$$

These two reactions are endothermic by 206 and 247 kJ/mol, respectively, and proceed catalytically above 1100 K. The dissociation of ammonia is endothermic by 70 kJ/mol and proceeds catalytically at 50-200 bar and 700 K as follows

$$NH_3 \leftrightarrow \frac{3}{2}H + \frac{1}{2}N_2 \quad (1.10)$$

1.3.3 Solar electrothermal and carbothermal reduction of metal oxides

Conventional industrial processes to extract metals from their oxides by carbothermic and electrolytic techniques are characterized by their high energy consumption. In addition, the extractive metallurgical processes are associated with releasing large amount of greenhouse gases and other pollutants that jeopardize our environments through the combustion of fossil fuels for heat and electricity generation. However, by using solar energy as the main source of high-temperature process heat, these harmful emissions can be reduced or even completely eliminated. Similar to hydrogen production from water-splitting through thermo-chemical cycles, the electrothermal and carbothermal reduction of metal oxides without a reducing agent and the carbothermal reduction with C and CH_4 as reducing agents are as follows [Steinfeld et al., 2001]:

$$M_xO_y \rightarrow xM + \frac{y}{2}O_2 \quad (1.11)$$

$$M_xO_y + yC \rightarrow xM + yCO \quad (1.12)$$

$$M_xO_y + yCH_4 \rightarrow xM + y(2H_2 + CO) \quad (1.13)$$

1.3.4 Solar upgrade and decarbonization of fossil fuel

The development of novel solar technologies will allow us to replace fossil fuels by solar fuels in the future. Since it is a long-term goal, we must consider a mid-term goal that aims at developing hybrid solar-fossil fuels. Fig. 1.9 shows the research strategy which

includes both the long-term goal of using solar fuels and the mid-term goal of using hybrid solar-fossil fuel [Steinfeld et al., 2001].

Solar thermal decomposition and solar thermal steam-reforming/gasification for the decarbonization of fossil fuels have been considered for producing hybrid solar-fossil fuel [Steinberg et al., 1999]. Fig. 1.10 illustrates these two concepts.

Since many fossil fuel reserves are located in the region with high solar irradiation, thermochemical processes stated above are important intermediate options for the sustainable energy-supply systems.

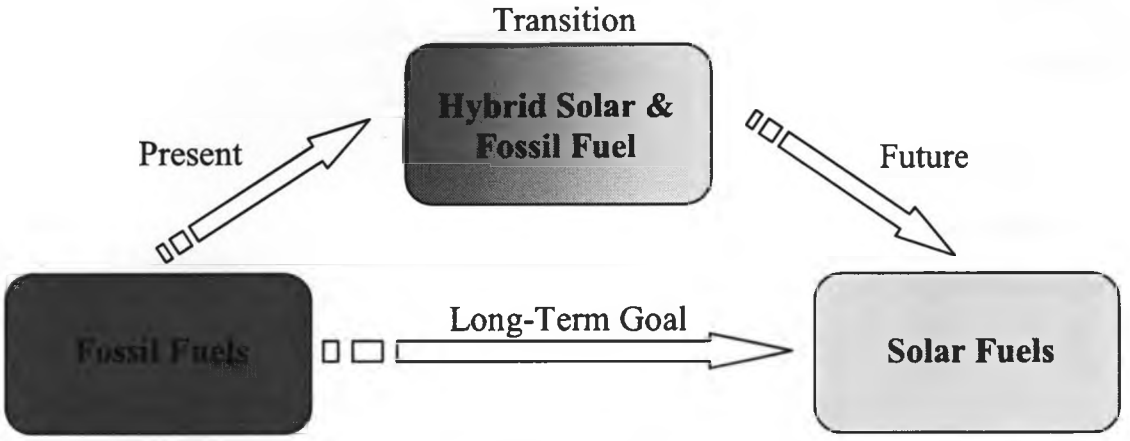

Fig. 1.9: Strategy for the replacement of fossil fuels by solar fuels [Steinfeld et al., 2001]

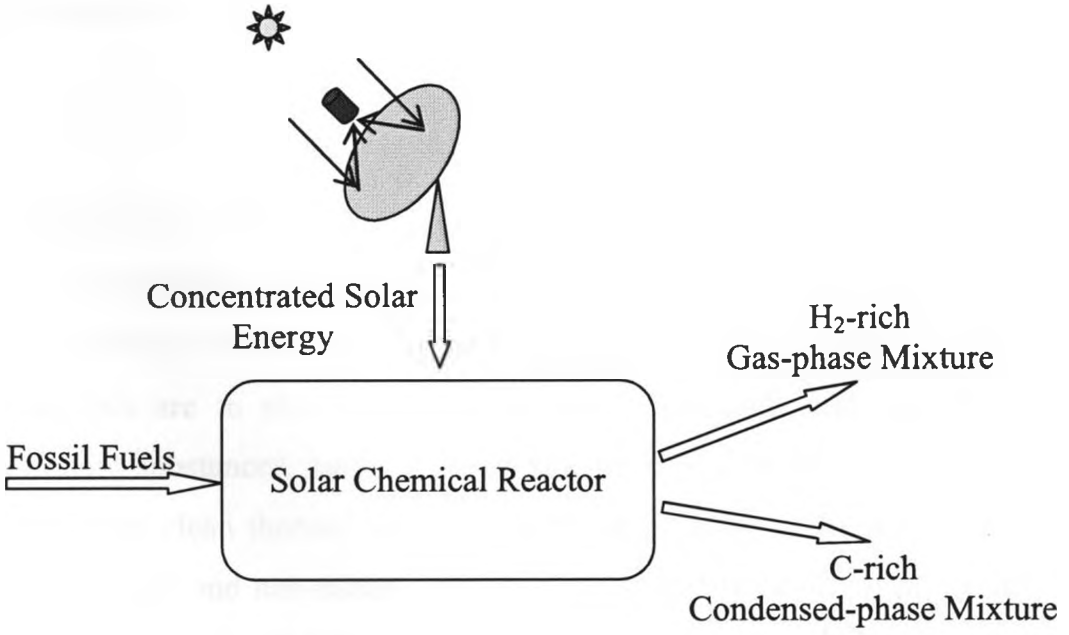

(a)

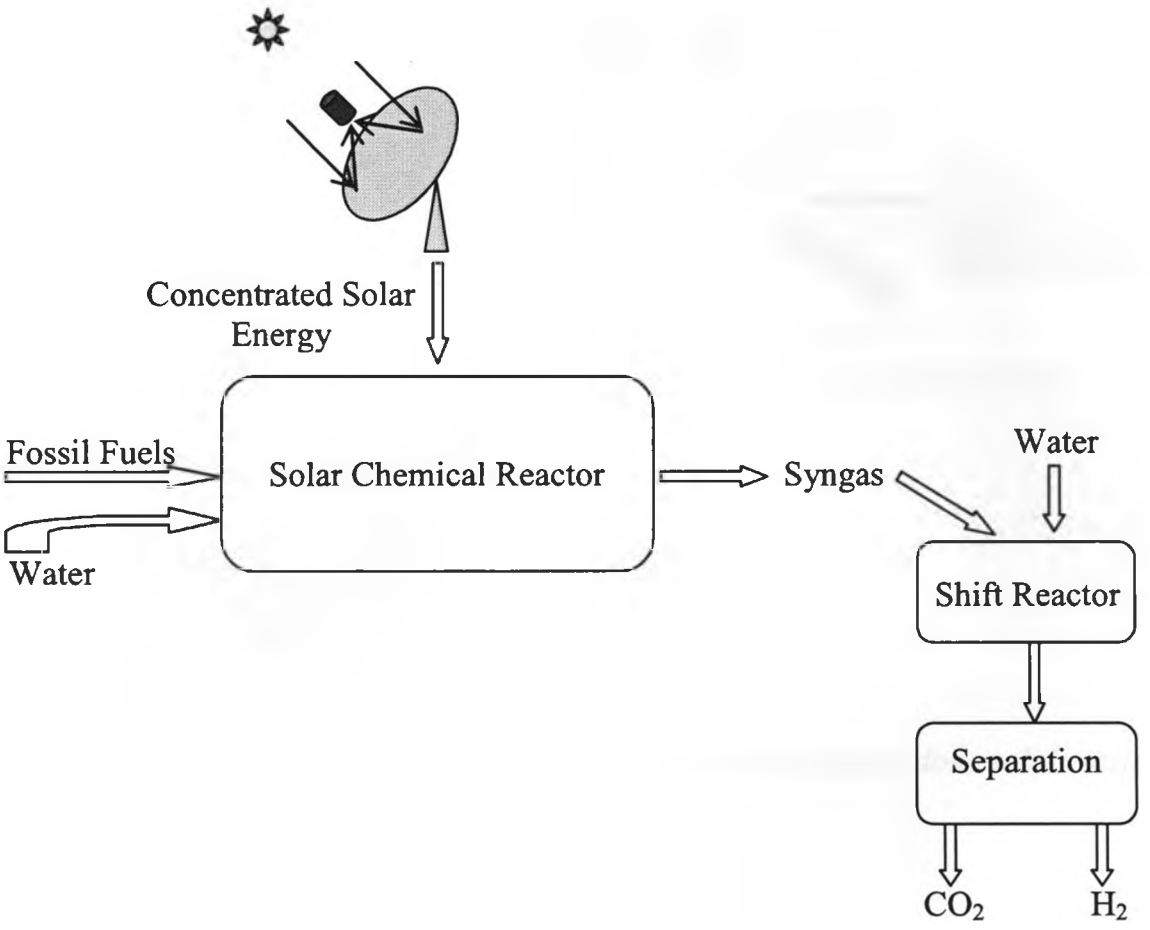

(b)

Fig. 1.10: Flow diagrams for the solar thermal decarbonization of fossil fuels. (a) Solar thermal decomposition and (b) solar thermal steam-reforming/gasification [Steinberg et al., 1999]

1.3.5 Solar thermal detoxification and recycling of waste materials

The treatment of hazardous residues from industrial processes frequently requires high temperature and intensive energy. The main purposes of high temperature treatment of hazardous materials are to eliminate toxic organic compounds and immobilize bio-available inorganic substances, such as water soluble heavy metal salts. Concentrated solar energy supplies clean thermal energy at high temperature to drive these processes involving gases, metals and non-metals. Fig. 1.11 illustrates the concept of a rotary kiln for treatment of solid and liquid wastes proposed by Funken et al. [1999].

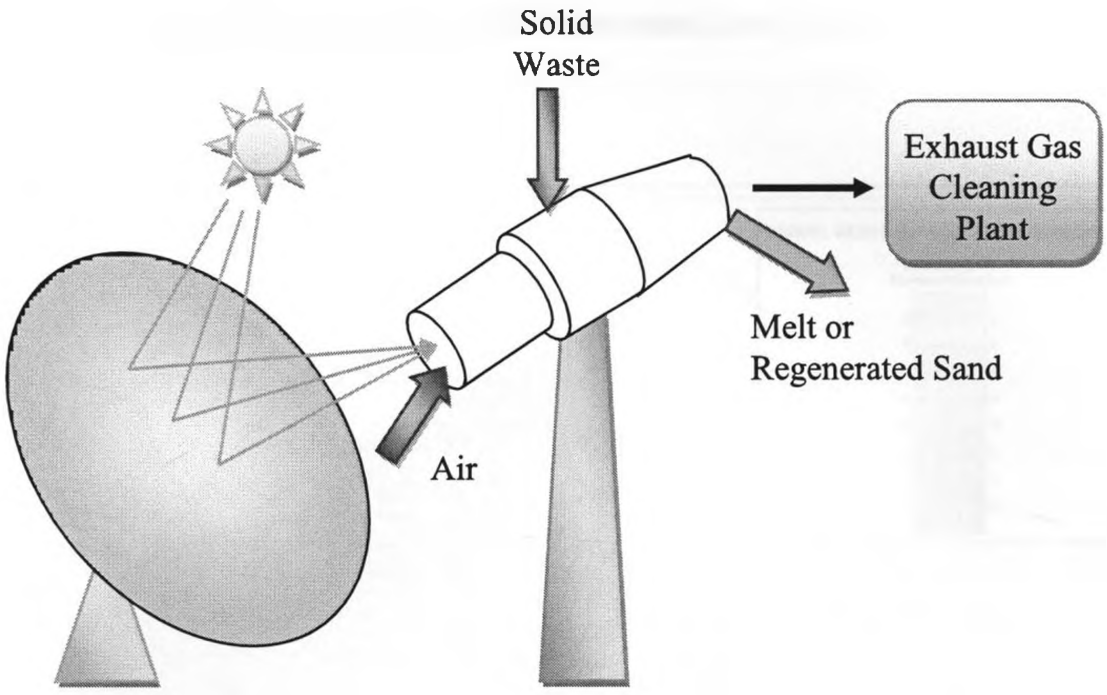

Fig. 1.11: Simplified sketch of a solar plant for treatment of hazardous solid wastes

1.4 Applications of Solar Energy in Canada

Currently, major applications of solar energy in Canada are focused on photovoltaic power systems. According to National Survey Report of Canada [2006], the total PV power installed capacity increased by 31% in 2006 to 20.5 MW compared to 16.75 MW at the end of 2006. The most common applications of PV in Canada (about 93%) are stand-alone systems consisting of PV array as the sole generator or as a hybrid system combined with a small wind turbine or diesel generator. The intensity of solar irradiance in Canada varies significantly from the values in the range of 13-14 MJ/m^2 in the southern region of the country to about 9 MJ/m^2 the arctic region (see Fig. 1.12). These values are, however, lower than that in the so-called sun-belt area that covers the central and southern regions of the United States in the North American continent. Therefore, the CSE systems are more advantageous in Canada as compared to the PV or collector systems, due to their ability to concentrate solar energy and obtain high quality heat at high temperatures. However, since the maximum temperature achieved in CSE systems could be relatively low in Canada, due to the lower solar influx, as compared to the

sunbelt region, CSE systems with high thermal efficiency must be designed that will be beneficial not only to Canada but also to the Europe which also has lower solar influx.

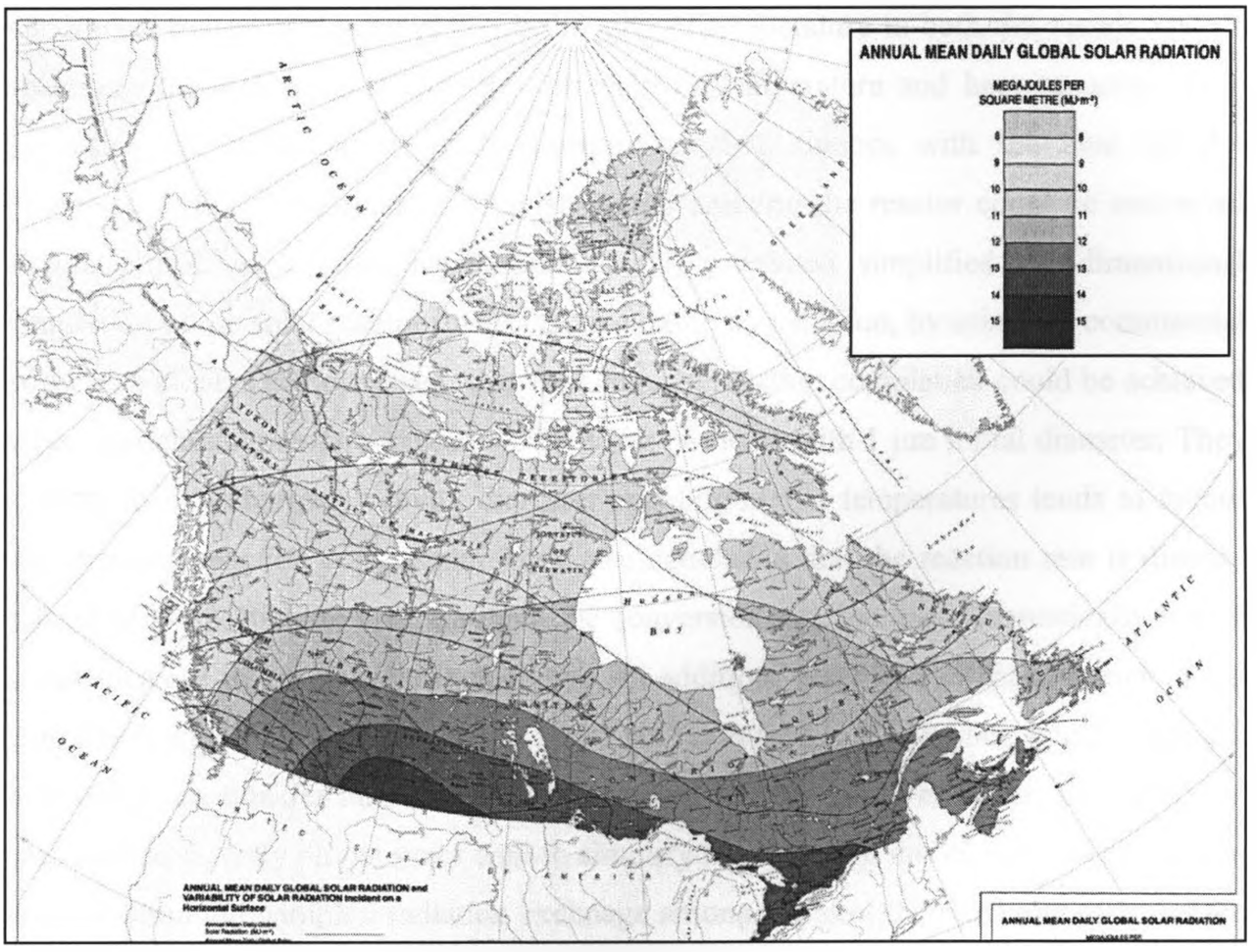

Fig. 1.12: Annual mean daily solar radiation in Canada (Source: Natural Resources Canada)

1.5 Literature Review

There are relatively few studies on the parabolic dish type CSE system which are focused only on the receiver section of the system. Meier et al. [1996] simulated the fluid particle flow and convective heat transfer in a high-temperature solar chemical reactor by using CFD code CFDS-FLOW3D. The converged solutions were found by using the standard k-ε turbulence model and the maximum temperature reached 1900 K. Air was considered as the working fluid. Convergence difficulites were encountered by applying the

renormalization group (RNG) k-ε turbulence model. Furthermore, they did not demonstrate the grid independence test and three-dimensional effects of the parabolic concentrator. Palumbo et al. [2004] analytically and conceptually illustrated the parameters for designing good solar thermal chemical reactors, such as geometry, feed conditions, materials' emissivity as a function of temperature in both the visible and IR spectrum, thermal conductivity as a function of temperature and heat capacity. They suggested the matching of decomposition reaction kinetics with the heat transfer processes so that large fraction of solar energy entering the reactor could be converted into chemical energy. Stephane et al. [2007] presented simplified two-dimensional simulation of the solar reactor involving zinc oxide dissociation, by using the commercial software Fluent. They observed that the chemical reaction completion could be achieved when particle temperature exceeds 2200 K for particles with 1 μm initial diameter. They suggest that the narrower cavity diameter enabling higher temperatures tends to favour the chemical reaction completion. They also concluded that the reaction rate is directly related to the particle temperature and the conversion rate increases dramatically with a slight increase in the particle temperature. In addition, when the initial diameter of fed particles is small, the available surface area per mass feed rate is higher, which enhances heat and mass transfer and chemical conversion. In their study however, the solar flux was applied directly on the inner wall to simplify the radiation model without taking into consideration the complex radiation exchnage among the sun, the parabolic dish and the solar receiver.

The Monte-Carlo ray-tracing method has been applied numerically to CFD code and coupled with optical properties to investigate radiation performance of parabolic dish with simplified cavity receivers by Shuai et al. [2008]. They suggested that the spherical receiver had relatively good radiation performance and proposed a upside-down pear shape receiver which could achieve almost uniform flux distribution. They also found that the surface slope error broadens the flux distribution and reduces the peak value of the distribution to maintain the energy balance.

In most of the previous studies on parabolic-dish type CSE, working fluids were not taken into consideration to examine the thermal performance. Very few studies have reported the thermo-fluid behavior inside the receiver in the presence of a working fluid.

An experimental model of solar chemical reactor consisting of a cylindrical cavity-receiver containing a tubular ceramic absorber coupled with elliptical mirror as concentrator is proposed by Melchior et al. [2008]. They found that the inner absorber surface of the receiver could reach up to 2500 K in the presence of Argon gas at a flow rate of 1 l/min. Their results show a good agreement with numerical simulations developed using Monte Carlo and finite difference techniques in two-dimensional domain. In addition, the thermal dissociation of ZnO into its elements, which reacts endothermically at temperatures above 1800 K was simulated numerically. The results show that the maximum solar-to-chemical energy conversion efficiency could reach up to 28.5% at a reactor temperature of 2300 k for an input solar power per unit length of absorber of 40 kW/m. Nepveu et al. [2009] presented a thermal model of energy conversion of Eurodish dish/Stirling. The results from their numerical model were in good agreement with the experimental measurements. The net conversion solar-electricity efficiency in their case was about 21% at a direct normal insolation value of 900 W/m^2 and at an ambient temperature of 20°C. They sugguested that the most important heat losses in the receiver cavity are spillage, reflection and IR-emission.

1.6 Motivation and Objectives

There are several issues associated with solar energy collection due to the nature of the solar irradiation. For instance, solar radiation on the surface of the earth is dilute and diffuse (only about 1 kW/m^2). Therefore, high energy conversion device has to be introduced in order to collect dilute solar rays. On the other hand, the sun is only available during day-time, so the intermittent nature hinders the continuous operation of solar energy systems. In addition, solar radiation is unequally distributed mostly between ±30 degrees from the equator. Thus, some fundamental understandings must be drawn before designing a high efficiency system.

No detailed investigation of thermal and radiative behavior of parabolic dish-receiver system in the presence of the working fluid has been reported. As a result, the influence of different geometrical, optical and operating parameters on the net radiation influx into the receiver is not well understood. The fundamental understanding of the flow behavior

and temperature distribution in such system is vital in order to improve the design of the solar reactor. Some important parameters, such as the aperture size of the receiver which allows concentrated solar radiation to enter the receiver, could have a significant influence on the radiant heat flux. The surface radiation properties of the materials could also have a considerable impact on the thermal performance. As the above literature review shows, very limited work has be conducted on the thermo-fluid behavior of parabolic-dish type CSE system. Previous studies focused only on the receiver and no attention has been paid to the parablic dish which is a crucial part of the system. That is, there is no detailed investigation of the behavior of coupled dish-receiver system. Furthermore, previous studies that simulated the behavior of the receiver were restricted to the 2D domain. The present research is focused on investigating the effects of different geometrical, optical and operating parameters on the thermofluid behavior in the coupled dish-receiver system in a 3D domain.

1.7 Thesis Layout

This thesis is comprised of five chapters. Chapter 1 includes an introduction of solar energy and solar energy systems, current applications of CSE systems, literature review and the objectives. Mathematical model is discussed in Chapter 2. The procedure of the development of parabolic dish model and the associated grid independent test is included in Chapter 3. Model validation process is also presented in Chapter 3. The results are presented and discussed in Chapter 4. The results are presented as a systematic parametric study by analyzing the influence of geometrical parameters, thermal radiative properties and operational parameters on the thermal performance of the receiver. Chapter 5 gives the conclusion and future recommendations.

CHAPTER 2: MATHEMATICAL MODEL

The flow solver in FEMAP computes a solution of the non-linear, partial differential equations for the conservation of mass, momentum and energy in a 3D geometry by using an element-based finite volume method and a coupled algebraic multigrid method to discretize and solve the governing equations [FEMAP-TMG User's Guide, 2006]. The governing equations are the time-averaged Navier-Stokes equations for 3D flows, expressed in Cartesian coordinates using the tensor notation as,

$$\frac{\partial \rho}{\partial t} + \frac{\partial (\rho U_j)}{\partial x_j} = S_m \tag{2.1}$$

$$\frac{\partial (\rho U_j)}{\partial t} + \frac{\partial (\rho U_i U_j)}{\partial x_i} = -\frac{\partial P}{\partial x_j} + \frac{\partial}{\partial x_i}\left(\mu\left(\frac{\partial (\rho U_i)}{\partial x_j} + \frac{\partial (\rho U_j)}{\partial x_i} - \overline{\rho u_i u_j}\right)\right) + S_{u_j} \tag{2.2}$$

$$\frac{\partial (\rho h)}{\partial t} + \frac{\partial (\rho U_j h)}{\partial x_j} = \frac{\partial}{\partial x_j}\left(\frac{k}{C_p}\frac{\partial T}{\partial x_j} - \overline{\rho u_j h'}\right) + S_h \tag{2.3}$$

Where, $i, j, k = 1, 2, 3$, ρ is the density of the working fluid, S_m, S_{u_j} and S_h are the source terms of the mass, momentum and energy equations, respectively, U_j and u_j are the components of the mean and the fluctuating velocity in the x_j direction, P is the pressure, μ is the dynamic viscosity of the fluid, k is the thermal conductivity, C_p is the specific heat at constant pressure, h and h' are the mean and the fluctuating static enthalpies. Eq. (2.1) expresses the conservation of mass of the fluid, Eq. (2.2) represents the conservation of momentum for general flows, and Eq. (2.3) represents the conservation of the total energy of the fluid and is valid for low speed flows. When the buoyancy effects are significant, the gravity force (ρg_j) is included in the source term S_{u_j} of Eq. (2.3).

In order to assess if the buoyancy effects are significant in the present study, the Grashof number Gr is calculated from the following equation:

$$Gr = \frac{g\beta (T_f - T_\infty) D^3}{v^2} \tag{2.4}$$

where g is the gravitational vector, β is the volumetric thermal expansion coefficient ($\sim 1/T_s$), T_f is the film temperature evaluated as $T_f = (T_w + T_\infty)/2)$ where, T_w is the solid wall temperature and T_∞ is the bulk temperature of the working fluid, D is the diameter of the receiver, v is the kinematic viscosity of the working fluid [Kreith et al., 2000]. Since high temperatures are expected in this study, we can assume a temperature range for T_w and T_∞, in order to estimate the Gr range. Based on the temperatures observed in the previous studies, we assume $500 < T_w < 2500$ K, $500 < T_\infty < 2000$ K. The simulation results at the later stage confirm these values. Based on the given range of temperatures, the Grashoff numbers are estimated to be in the range $10^7 < Gr < 10^8$. Reynolds number is calculated at the inlet conditions, by assuming the velocity of working fluid between 0.025 m/s and 0.8 m/s. The corresponding range of Reynolds number is $25 < \mathrm{Re} < 811$. The heat transfer theory indicates that if $Gr/Re^2 >> 1$, the buoyancy effects are significant [Kreith et al., 2000]. From the present analysis it is fond that $Gr/Re^2 > 152$ which implies that the buoyancy effects (i.e. turbulent convection) are significant in the present study. Thus, the buoyancy effects are considered in the governing equations using the Boussinesq approximation. Due to the smaller flow velocities (less than 1 m/s) the compressibility effects are not taken into consideration.

Three turbulence models are available to model the Reynolds stresses and fluxes: the fixed viscosity model, the mixing length model and the standard two equation k-ε model. Due to the presence of the swirling flow, the mixing length model is selected as our turbulence model because it can provides more accurate predictions for flows with rotation than K-ε model, and it is more robust and less computationally intensive [FEMAP-TMG User's Guide, 2006]. The Reynolds stresses and fluxes are evaluated using a Boussinesq eddy viscosity assumption [FEMAP-TMG User's Guide, 2006]. It states that the Reynolds stress can be expressed as the product of an effective eddy viscosity and the mean flow strain rate,

$$\tau_w = \mu_t \frac{dU}{dy} \tag{2.5}$$

The mixing length turbulence model is a zero-equation model which uses the following relationship to calculate the turbulent viscosity:

$$\mu_t = \rho l^2 S \tag{2.6}$$

where l is the mixing length and S is the modulus of the mean strain rate [FEMAP-TMG User's Guide, 2006]. The mixing length l is defined as:

$$l = \min(f_l \kappa y_n, 0.09 y_{max}) \tag{2.7}$$

where f_l is the damping factor given by

$$f_l = 1 - \exp(-\frac{y_n^+}{26}) \tag{2.8}$$

κ is the Von Karman constant (κ =0.41), y_n is the normal distance from the node to the wall and y_{max} is a characteristic length scale for the model [FEMAP-TMG User's Guide, 2006]. For cylindrical duct, the above length scale is equivalent to half the hydraulic diameter. For internal nodes (i.e. nodes which are not touching a wall), the modulus of the mean strain rate is given by [FEMAP-TMG User's Guide, 2006]:

$$S = \sqrt{2 S_{ij} S_{ij}} \tag{2.9}$$

$$S_{ij} = \frac{1}{2}(\frac{\partial U_i}{\partial x_j} + \frac{\partial U_j}{\partial x_i}) \tag{2.10}$$

For wall nodes, the strain rate is based on the logarithmic wall function:

$$S = \frac{dU}{dy_n} = \frac{u_*}{\kappa y_n} \tag{2.11}$$

where u_* is the shear velocity [FEMAP-TMG User's Guide, 2006].

To express the overall effect of convection heat transfer inside the receiver, Newton's law of cooling is used,

$$Q = h \cdot A(T_w - T_a) \tag{2.12}$$

where, Q is the rate of convection heat transfer, h is the heat transfer coefficient, A is the heat transfer surface area, T_w is the wall temperature and T_a is the bulk fluid temperature. The thermal simulation requires the solution of coupled 3-D flow and thermal phenomena. By utilizing the element-based finite difference method, a hybrid approach has been used [FEMAP-TMG User's Guide, 2006]. Control volumes are established on convecting faces and convective conductance are calculated from the thermal model to the faces of the flow model. Therefore, Newton's law of cooling is transformed to

$$Q = G_{ij} \cdot (T_w - T_f) \tag{2.13}$$

where G_{ij} is the convective conductance from the convecting element i to the fluid face j, T_w is the wall temperature and T_f is the film temperature [FEMAP-TMG User's Guide, 2006]. The conductive conductance is calculated as [FEMAP-TMG User's Guide, 2006],

$$G_{ij} = h_c A \tag{2.14}$$

where h_c is the convective heat transfer coefficient and A is the overlapping surface area between the convecting solid element and the fluid surface element. This technique can couple dissimilar element meshes during solving [FEMAP-TMG User's Guide, 2006]. Convective heat transfer coefficient is computed by using the local physically based flow solution and model geometry. For the region in the boundary layer or near wall region, a semi-analytical approach is used whereby the effects of the near-wall region are modeled using near-wall relations or wall functions for accurate prediction [FEMAP-TMG User's Guide, 2006]. That is, the thermal and velocity profiles near the wall are assumed to be logarithmic and the associated logarithmic relations for the velocity and temperature are used to estimate wall shear stress and convective heat transfer. The wall functions in the flow are assumed to be linear in the laminar sub-layer and a blending function is used for the transition between laminar and log-law regions. The equation for h_c is

$$h_c = \Theta_y \cdot \Theta_r \times h_w \tag{2.15}$$

where Θ_y is a mesh correction factor, Θ_r is a roughness factor and h_w is the near-wall heat transfer coefficient calculated using the log-law wall function,

$$h_w = \frac{\rho C_p u^*}{T^+} \tag{2.16}$$

where u^* is the friction velocity and T^+ is a dimensionless term calculated from the thermal wall function [FEMAP-TMG User's Guide, 2006]. The equation for T^+ is

$$T^+ = \frac{\rho C_p u^* (T_w - T_f)}{q_w} \tag{2.17}$$

where q_w is the heat flux between the wall and the fluid, it is related to wall and fluid temperatures through

$$q_w \approx -k \frac{T_w - T_f}{y_f} \tag{2.18}$$

where y_f is the distance from the wall at which T_f is evaluated [FEMAP-TMG User's Guide, 2006].

The radiation modeling is divided into two main categories: heat exchange through radiation within the model, and heating from a solar source. The general procedure as outlined in the FEMAP-TMG User's Guide, 2006 is described below. The enclosure(s) is defined first, i.e. a space that encloses the entire model. Once the enclosure is defined, view factors of all the elements within the enclosure are calculated. A shadow check is also performed on all elements to determine if they have obstructed or unobstructed view of each other. For obstructed viewing, the shadowed view factors are calculated by Hemicube method. The Hemicube method uses graphics to draw the sketches of elements as seen from each other element in the model, and then it post processes these images to determine the view factors. As this method computes all possible view factors, it

occupies too much computer resources which results in longer computation time. A new algorithm has been used which removes insignificant view factors and thus, reduces the computational time when applying the Hemicube method. This algorithm first computes all view factors (VF_{ji}) from each emitting element i, sorts them in ascending order, and then removes the first n view factors from list such that

$$\sum_{i=1,n} VF_{in} < C \tag{2.19}$$

where C can be defined by the user [FEMAP-TMG User's Guide, 2006]. The larger value of C means less accurate results. Typically, the value of C smaller than 0.05 shows negligible impact on the results [FEMAP-TMG User's Guide, 2006]. Black body view factors are used to calculate IR radiative exchanges between elements and are functions of surface geometry only. That is,

$$A_i F_{ij} = A_j F_{ji} = \frac{1}{\pi} \iint_{A_j A_i} \cos\phi_i \cos\phi_j \frac{dA_i dA_j}{r^2} \tag{2.20}$$

where F_{ij} is the black body view factor from surface i to surface j, ϕ is the angle between the axis normal to the corresponding surface and the direction of incident radiation [FEMAP-TMG User's Guide, 2006]. Radiative conductance is calculated with Oppenheim's method, which utilizes the radiosity approach. Radiosity is the total radiation (reflected plus emitted) leaving a surface. In a cavity consisting of several surfaces, a matrix calculation method is used to solve for temperature and heat exchange between all of the surfaces at steady state. TMG creates an additional non-geometric surface element for each radiating element within the space enclosure, and couples it to its parent with a conductance equal to $\rho A\varepsilon/(1-\varepsilon)$, where ρ is the reflectivity and ε is the emissivity of the element. The black body view factor matrix is then used to create coupling between the new surface elements equal to ρAVF_{ij}. This approach allows efficient and accurate modeling of temperature dependent emissivity values. Since diurnal heating is defined and used to create a solar spectrum source, the calculation of solar spectrum view factors is also performed. TMG determines which elements have a

direct view to the solar heat source in order to calculate the heat loads on the elements. Solar view factors reflect the amount of energy an element receives from the sun which is modeled as a distant point source. Ray-tracing is performed automatically if any solar specular surface is defined in the model. Only collimated rays are launched from specular or transmissive elements with direct solar view factors greater than zero.
The steady-state energy balance for the system yields

$$\sum Q = 0 = Q_{solar} - Q_{reradiati\ on} - Q_{convection} - Q_{conduction} \quad (2.21)$$

where, Q_{solar} is the total solar energy input to the system, $Q_{reradiation}$ is the power lost by re-radiation, which cannot be captured by the inner wall, $Q_{convection}$ is the energy transferred by convection to the gas stream inside the solar reactor, $Q_{conduction}$ is the energy stored within the wall at the steady state. If the wall is assumed to be adiabatic, the energy stored in the wall by conduction is negligible, therefore, $Q_{conduction} = 0$. The radiation and re-radiation on the outer surface are also negligible in this case. The energy transfer to the flow is through conduction and convection only, since elementary gases such as O_2, N_2, H_2 and dry air have a symmetrical molecular structure and they neither emit nor absorb radiation unless they are heated to extremely high temperatures at which they become ionized plasmas and electronic energy transformations occur [Kreith et al., 2000].

CHAPTER 3: NUMERICAL SIMULATIONS

The radiation source is the sun with constant beam flux and the sun is assumed as a point source. The solar radiation is only distributed in the visible band. The back of the mirror is considered adiabatic due to insignificant effects of conduction and convection. The walls of the solar receiver are also considered to be adiabatic. Thus, no convection and conduction heat transfer outside the solar receiver are considered. It is also assumed that the sun illuminates parabolic dish only i.e. the solar radiation directly incident on the receiver is neglected.

3.1 CFD Software Selection

Since the simulation involved complex radiation and solar loads models, CFD software must be selected based on the functions of two different state-of-the-art software, Fluent and FEMAP with TMG. The primary selection criterion is the capability of the software to model complex radiation with adjustable solar loads. There are two different solar loads models available in Fluent, solar ray tracing model and discrete ordinates (DO) irradiation model [Fluent 6.3 User's Guide, 2006]. The solar ray tracing model includes only boundary zones that are adjacent to fluid zones in the ray tracing calculations. In other words, boundary zones that are attached to solid zones are ignored. Because the parabolic dish is a solid part not in the vicinity of fluid zones, thus this part cannot be considered by the solar ray tracing model in Fluent. Therefore, this model is not capable of simulating three-dimensional reflection on the solid surface. Unlike the ray tracing solar load option, the DO irradiation method does not compute heat fluxes and apply them as heat sources to the energy equation. Thus, the irradiation flux is applied directly to semi-transparent walls (that you specify) as a boundary condition, and the radiative heat transfer is derived from the solution of the DO radiative transfer equation. However, the system has no semi-transparent wall, thus, the reflection on the inner surface of both the solar reactor and the parabolic dish cannot not be computed. Therefore, DO irradiation is not suitable either. The radiation model in FEMAP with advanced thermal

and fluid module is based on the material optical properties to calculate the solar and infrared performance. It is integrated with diurnal heating model to calculate direct solar view factors for selected elements for a fixed sun position or at selected calculation points along the sun's trajectory. The absorptivity, reflectivity and other optical parameters must be defined for diurnal heating [FEMAP-TMG User's Guide, 2006]. The radiation model from FEMAP satisfied the criterion for this simulation, hence, it is selected.

3.2 Configuration

The model consists of two components; a parabolic dish concentrator and a cylindrical solar receiver. The vertex of the parabolic dish is set as origin for the global coordinate system. The coordinates of the parabolic dish and the receiver are defined based on this global coordinate system. The parabolic dish is designed from the standard parabolic equation,

$$y = \frac{X^2}{4 \times f} \tag{3.1}$$

Where, f *is* the focal distance. The focal distance and the concentration angle are set equal to 1 m and 90°, respectively (see Fig. 3.1). This resulted in the surface area of 2.3 m^2, calculated from the following equation:

$$A_s = \frac{8\pi f^2}{3}\{[(\frac{d}{4f})^2 + 1]^{\frac{3}{2}} - 1\} \tag{3.2}$$

where, d is the diameter of the dish, which is equal to 1.675 m. The solar receiver is cylindrical in shape with the diameter of 0.2 m and height of 0.3 m. The aperture of the cylinder is located at the focal point of the parabolic dish. The inlet and outlet connecting pipes are 0.03 m in diameter and 0.1 m long. For the initial configuration, the inlet and outlet are attached tangentially at the lower and upper ends of the solar receiver, respectively (see Fig. 3.2). Argon is considered as the working gas.

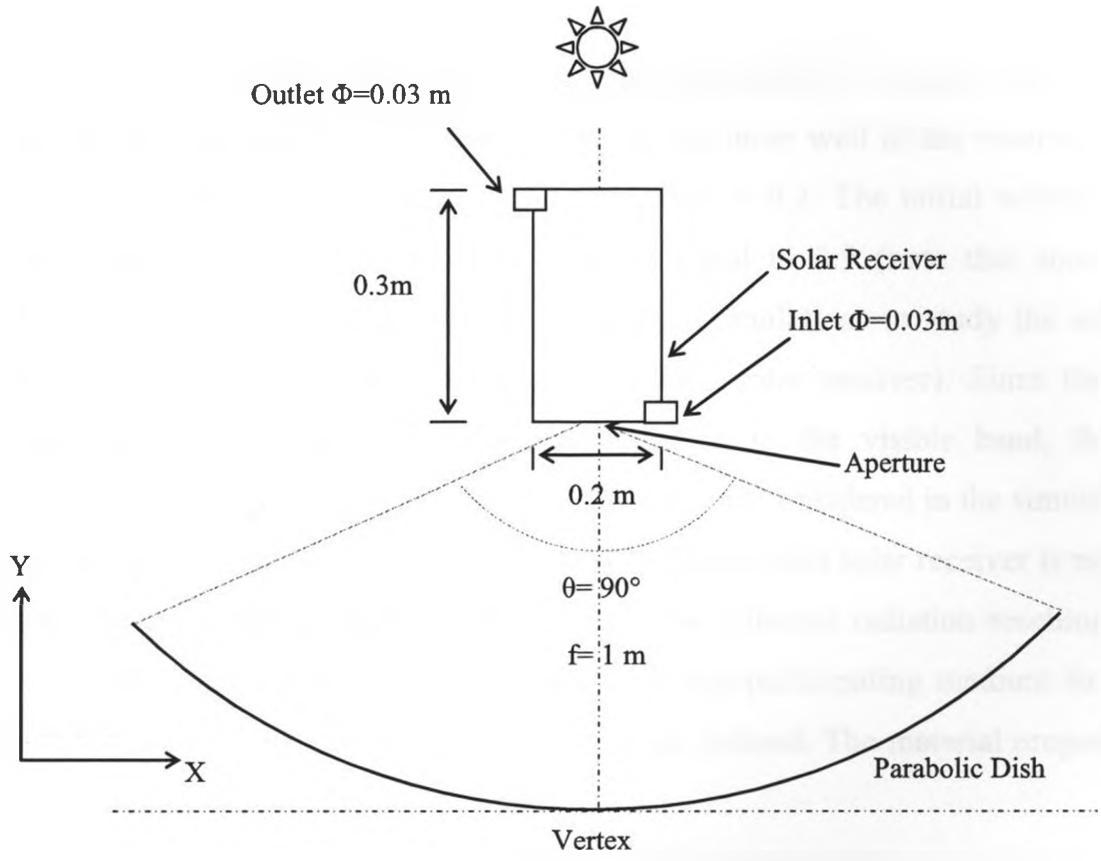

Fig 3.1: Schematic of the parabolic-dish CSE system

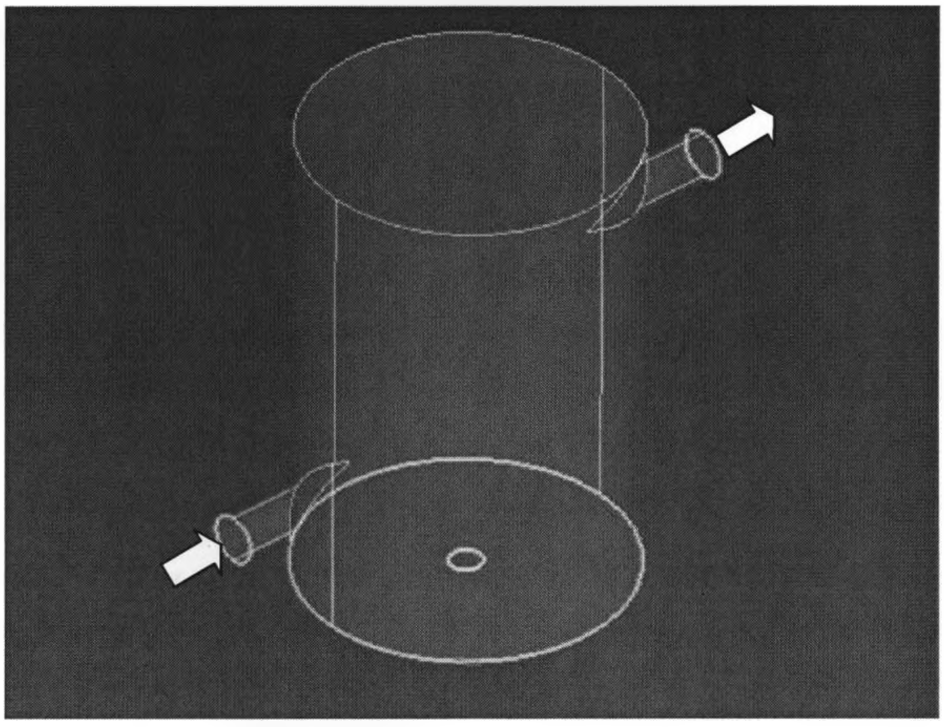

Fig. 3.2: Geometry of the solar receiver

3.3 Materials and their Properties

The receiver wall is made of ceramic material (Al_2O_3), which has low thermal conductivity. The initial radiation properties of the inner wall of the receiver are set as, emissivity = 0.8, absorptivity = 0.8 and reflectivity = 0.2. The initial reflectivity of the parabolic-dish reflective surface has been set equal to 0.9 (note that some of these radiation properties are varied at a later stage of simulations to study the influence of their variation on the thermal performance of the solar receiver). Since the radiation source i.e. the sun, only emits thermal radiation in the visible band, the infrared emissivity and reflectivity of the parabolic dish are not considered in the simulations. The infrared radiation emitted by the parabolic-dish that reaches solar receiver is neglected as its magnitude would be significantly less than the reflected radiation reaching the solar receiver. Because argon gas is considered as a non-participating medium for radiation inside the receiver, its radiation properties are not defined. The material properties of the given materials are listed in Table 3.1.

Materials	ρ (kg/m^3)	c_p (J/kgK)	k (W/mK)	Solar Absorptivity	Solar Reflectivity	Infrared Emissivity
Mirror	7850	400	40	0.1-0.5	0.5-0.9	N/A
Ceramic	3900	1274.5	40	0.5-0.9	0.1-0.51	0.5-0.9
Argon	1.623	520.6	0.0158	N/A	N/A	N/A

Table 3.1 Materials properties

3.4 Component Properties

Since the walls of both parabolic-dish and solar receiver are considered as adiabatic, they are defined as plate type with the thickness of 0.001 m and meshed as surface. Argon is defined as volume type with tetrahedral mesh. The component properties are shown in Table 3.2.

Component	Material	Mesh Type	Element Type	Property
Parabolic dish	Mirror	Surface	Quadratic	Plate type with thickness =0.001 m
Receiver wall	Ceramic	Surface	Triangle	Plate type with thickness =0.001 m
Fluid	Argon	Solid	Tetrahedral	Solid volume element

Table 3.2 Mesh setting summary

3.5 Operating Conditions and Solver Control

The location is defined as Mexico City with latitude 19 degrees at local solar time 12:00 AM on 1st day of January. The corresponding maximum solar flux on the ground (clear sky) is 1412 W/m^2. The orientation of the model is set in a way that the focal point of the dish aligns with the sun. Thus theoretically, all the beam radiation is focused at the aperture. The interior of the solar receiver is defined as convection flow surface with 10 micron surface roughness. Argon gas, initially at ambient conditions (298.15 K temperature and 101325 Pa pressure), enters through the tangential inlet with constant a velocity of 0.8 m/s, and leaves through the outlet which exposes to the ambient conditions. Iteration limit for thermal solver is set to 10000. The convergence criterion for flow solver is when the residuals of global momentum, mass and energy are smaller than 2×10^{-4}. The Second Order Upwind method is chosen for simulations in the flow domain. In order to ensure the accuracy of the coupled solvers, concurrent solution method is set to communicate every flow iteration. In other words, every flow iteration in the flow domain is followed by a thermal iteration. Some advanced solver options are enabled for radiation to reduce the computation time without compromising the accuracy. First, the dispose of small view factors (C) is set to 0.05. Secondly, tracing bounce limit is set to 10, which means the maximum allowable bounce for a given ray is 10. This results in the elimination of ray after 10 bounces and the corresponding accuracy is promised for the reflectivity of the receiver up to 0.5. The extinction limit of rays during ray-tracing is set to 0.1%, which implies that a ray will be eliminated if its energy becomes smaller than 0.1% of its original value before 10 bounces. Patch elements method temporarily merges adjacent elements for the purposes of calculating radiative exchange, so for view factors calculations, this method is selected to accelerate the computation since the model contains large amount of radiative elements.

3.6 Grid Independence Test

The complex nature of the CSE system necessitates the test of different grid sizes. Since the grid size of the parabolic dish has a significant impact on the accuracy of the simulation, thus grid independent tests are conducted for the parabolic dish and the solar

receiver separately. For the grid independent test of the parabolic dish, a 4 cm × 4 cm square piece of ceramic with the absorptivity of 0.9 is placed at the focal plane in order to capture the reflected rays and to quantify the influx of concentrated radiation (see Fig. 3.3). The reflectivity of the parabolic dish is set to 1.0 throughout the grid independence test. The focal plane contains 1600 quadratic elements. In order to make a uniform mesh distribution on the parabolic surface, several methods were tested. The surface, divided into eight identical pieces and meshed individually, showed more uniform mesh (see Fig. 3.4). The materials, component properties, operation control and solver control are the same as defined in the earlier sections except the flow solver which is disabled since there is no flow involved. The total energy received by the ceramic material (E_f) is set as the criterion for the grid independence.

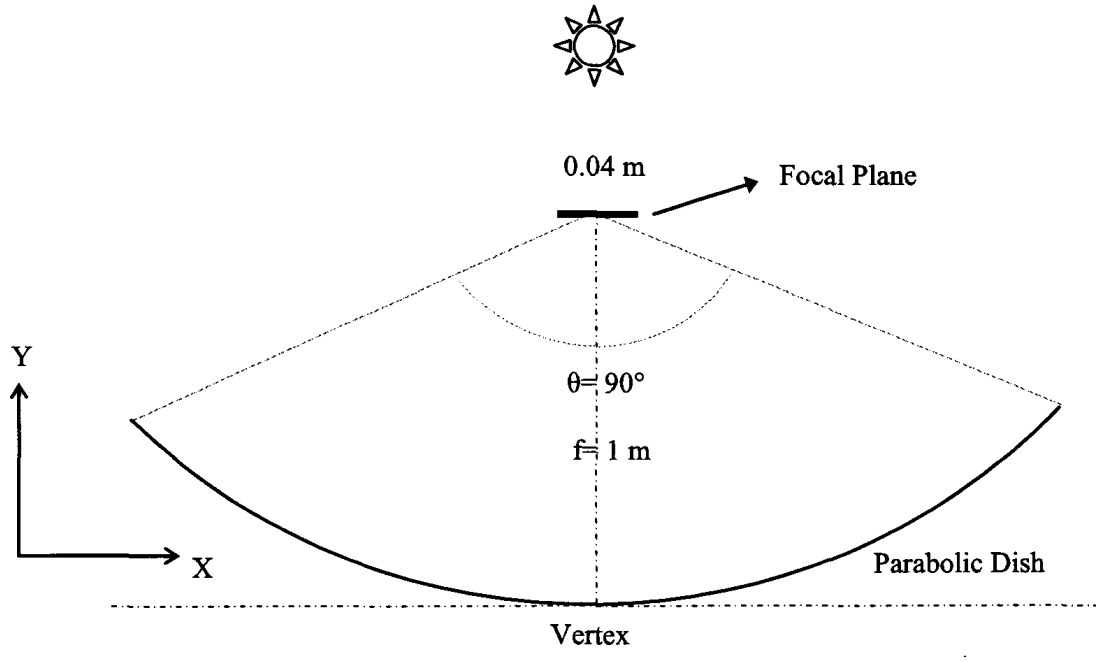

Fig. 3.3: Schematic of grid independent test for the parabolic-dish

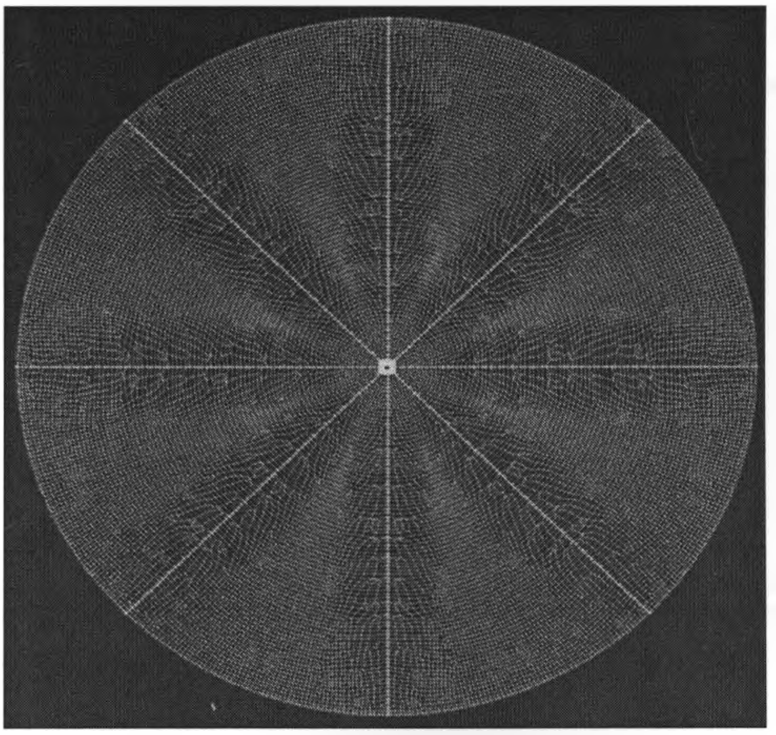

Fig. 3.4: Mesh of the parabolic surface

The total energy from the sun incident on the parabolic dish (E_{total}) is calculated by multiplying the surface area of the dish by the solar flux, which for the given conditions is equal to 3245.77 W. The percent difference between the total energy of incident solar flux (E_{total}) from the sun on the dish and the total energy captured by the focal plane (E_f) is defined as,

$$\theta = \frac{E_{total} - E_f}{E_{total}} \times 100 \tag{3.3}$$

The summary of grid independence test for the parabolic dish along with the values of E_f and are listed in Table 3.3. The percentage of energy captured at the focal plane is plotted versus the number of elements in Fig. 3.5 to further illustrate the mesh dependency. The results indicate that by increasing the number of elements, the difference becomes essentially close to 4.4%. The 4.4% loss could be due to the imperfect parabolic surface (the parabolic surface is comprised of many small flat elements) deflects some rays

which cannot be focused on the focal plane. The results also show that E_f starts to converge with the variations of less than 0.1% when the number of elements is 19,857.

Mesh size on the parabolic dish (m)	No. of elements on the parabolic dish	E_f (W)	θ (%)	CPU time (s)
0.020	6,406	3048.41	6.08	3257.5
0.015	10,736	3096.95	4.59	7327.4
0.011	19,857	3104.24	4.36	21197.4
0.010	23,507	3100.01	4.49	30768.9
0.009	29,134	3106.89	4.28	42022.8
0.008	37,660	3101.74	4.44	66780.1
0.007	47,962	3102.50	4.41	120341.0

Table 3.3 Total energy captured by the focal plane with increasing number of elements

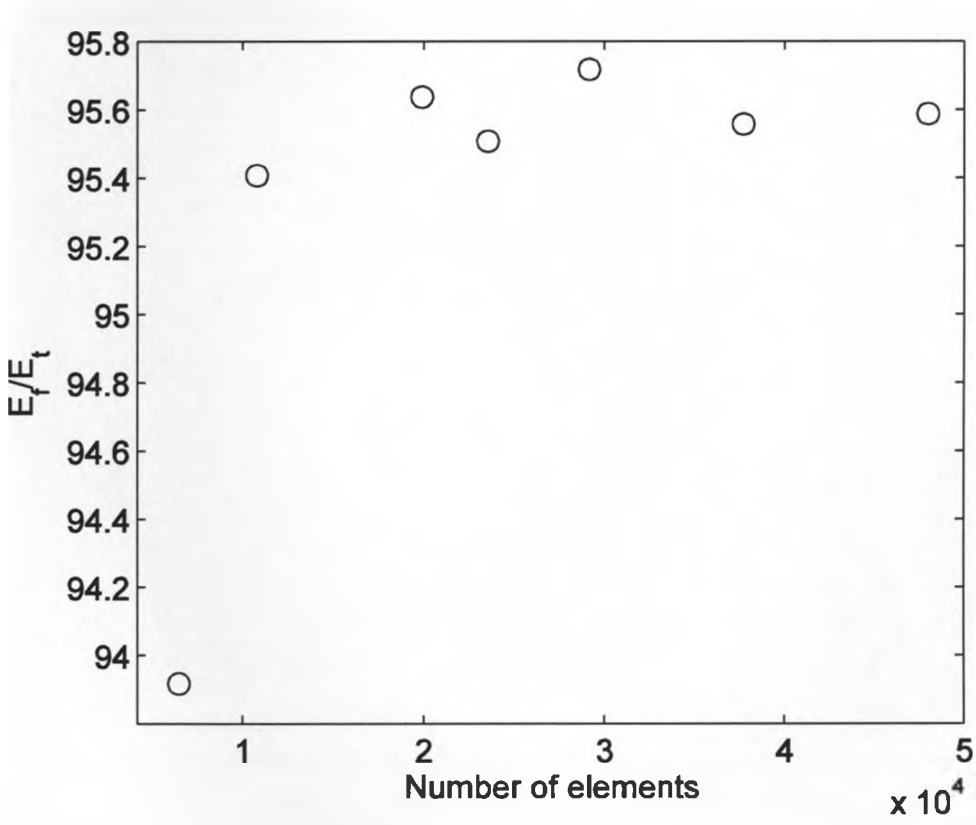

Fig. 3.5: Captured energy on the focal plane with increasing number of elements on the dish

Further investigation on the focusing effect to ensure the accuracy of optical geometry is conducted by visualizing the flux map of the ceramic plate at the focal plane and comparing the concentration ratio with the existing data. Fig. 3.6 presents the solar flux map in the focal plane when the number of elements is 19,857. It shows the symmetrical circle image at the center with a peak flux of 28,045 kW/m^2. The figure clearly shows that the ceramic plate captured almost the entire radiation reflected by the parabolic dish. The value of θ is not expected to zero in the present case due to the reason that the dish comprised small flat reflecting surfaces each equal to the grid size, instead of a continuous parabolic surface. This configuration is closer to the real applications where the parabolic dish is made of several small flat mirrors. Thus, it is likely that a small fraction of radiation reflected by the dish does not reach the 4 cm × 4 cm ceramic plate.

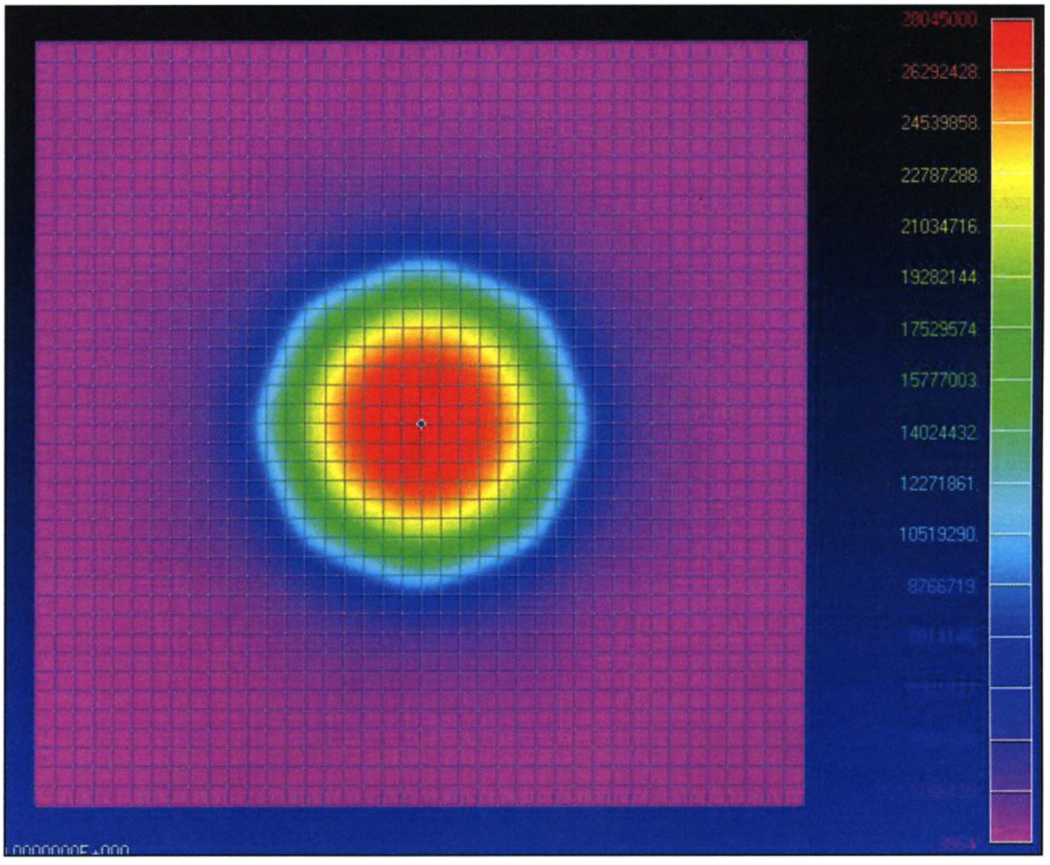

Fig.3.6: Solar flux map in the focal plane

Fig. 3.7 shows the comparison of concentration ratio at the focal plane between the simulation results obtained by Shuai et al. [2007] using the Monte-Carlo ray tracing method and the results from this paper. Since in Shuai's simulation, an ideal parabolic dish was considered instead of defining a parabolic surface consisting of large number of small flat pieces in this paper, therefore, the radiation loss due to the imperfection of the curvature is 0. The peak concentration value is 22,000 in Shuai's results and the peak value from our simulation is recorded with a value of 20,000 approximately. It can be seen that the results are in a good agreement with the data in reference. In addition, we can see that the results are close to the theoretical maximum value calculated from Eq. (1.2), which gives approximate concentration ratio 23,000 when rim angle is 45 degree.

For the grid independent test of the solar receiver, the exact same settings as described above are applied except that the constant heat flux is imposed on the interior cylindrical surface of the solar receiver (for the simulations in Chapter 4, some parameters are changed). The constant heat flux is computed from the total incident energy on the dish

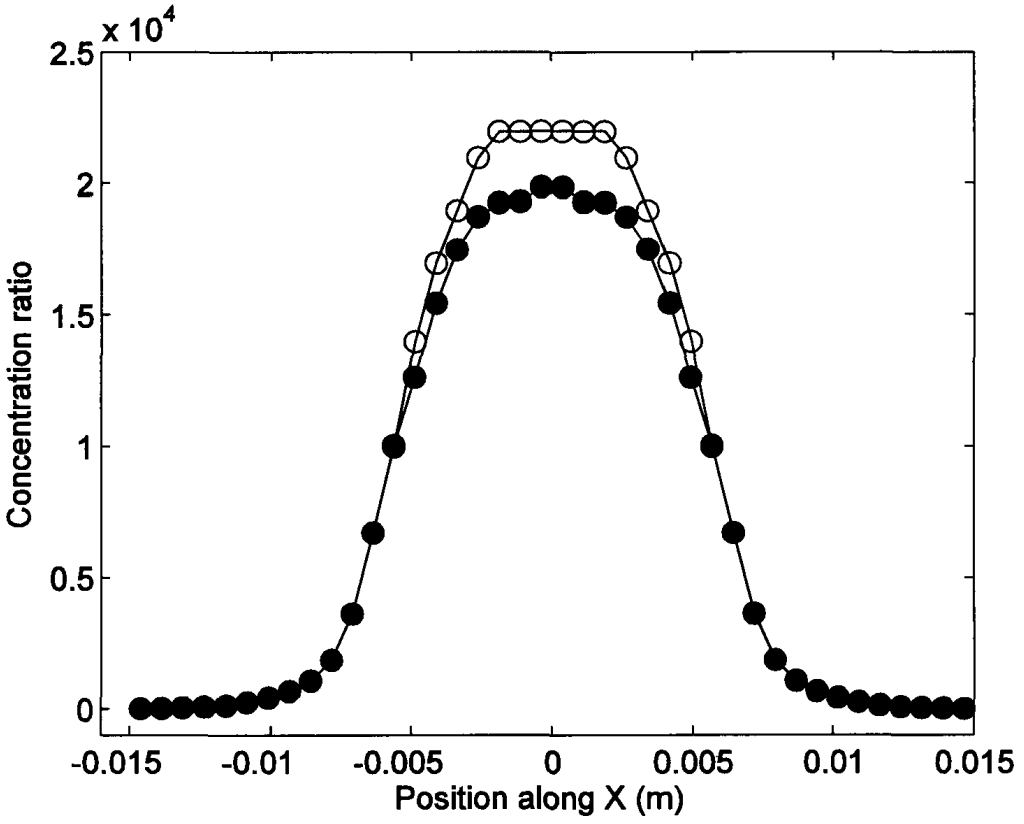

Fig. 3.7: Comparison of concentration ratio at the focal plane. Open circle: Shuai 2008; solid circle: this paper.

divided by the area of the cylindrical surface, which gives a magnitude of approximately 17,000 W/m^2. The direction of the flux is normal to the cylindrical surface. Since we are more concerned about the thermal performance inside the receiver, thus, average wall temperature and average fluid temperature are selected as the evaluating parameters for grid independent test. The grid size on the cylinder surface is kept the same as the mesh size of argon gas. The elements along the inlet and outlet pipes are 20 for all cases.

Fig. 3.8 shows the average wall temperature and average fluid temperature for a range of mesh sizes. Figure shows that the fluid temperature starts to converge at the mesh size of 0.004 m. The plot also shows that the wall temperature is independent of the mesh size. These values along with the number of elements and CPU time are also listed in Table 3.4.

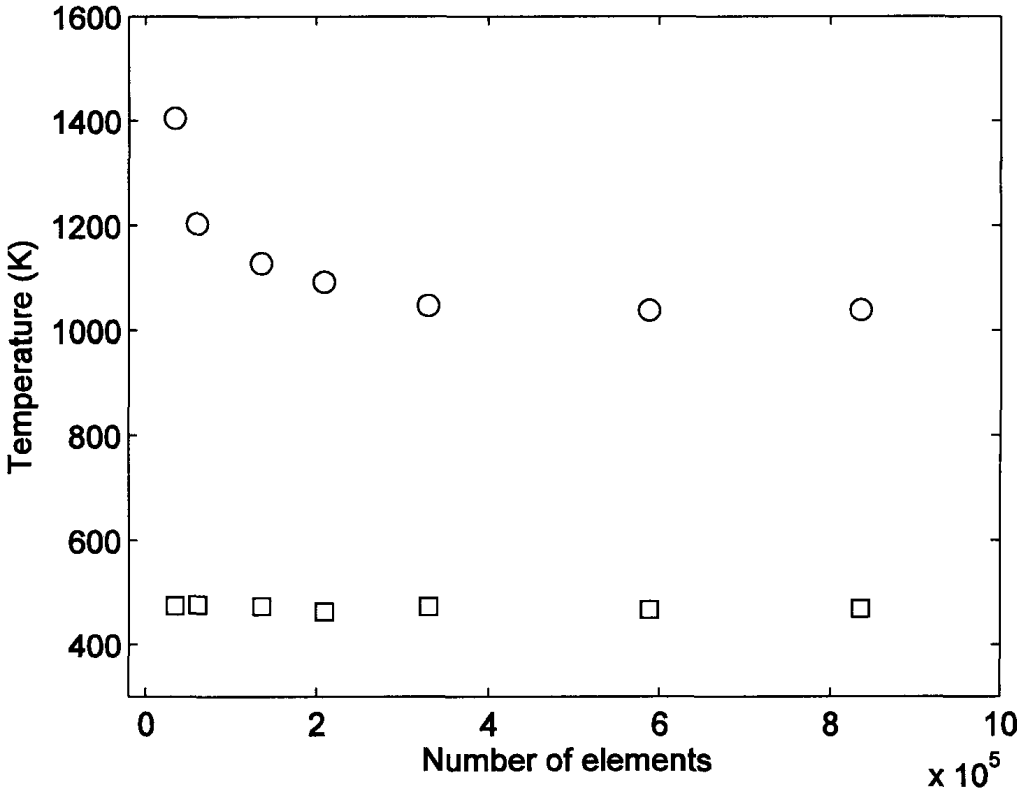

Fig. 3.8: Average wall temperature and average fluid temperature in the solar receiver with increasing number of elements when no parabolic dish. Circle: Average wall temperature; Square: Average fluid temperature.

Mesh size on the solar receiver (m)	No. of elements in the solar receiver	Average wall temperature (K)	Average fluid temperature (K)	CPU time (s)
0.010	33,737	1406.2	476.1	299
0.008	60,342	1204.6	477.8	584
0.006	134,714	1129.4	474.9	1626
0.005	207,891	1093.7	464.8	2586
0.004	329,217	1048.6	473.8	4527
0.003	587,163	1039.4	468.1	4135
0.0025	834,119	1040.1	470.3	6102

Table 3.4 Average wall temperature and average fluid temperature in the solar receiver with increasing number of elements when no parabolic dish present

In summary, with mesh size of 0.01 m for the parabolic dish and 0.003 m for the solar receiver, the accuracy of results is ensured and the computation time is acceptable. Therefore, they are selected to do the actual simulation of the complete CSE system. The selected mesh on the solar receiver is shown in Fig. 3.9.

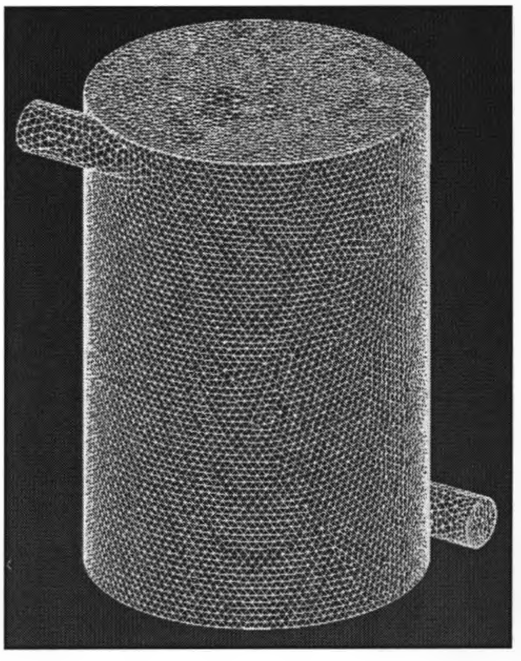

Fig. 3.9: Mesh of the solar receiver

3.7 Model Validation

In order to ensure that the simulation model is developed correctly and the algorithms have been properly implemented, model validation is conducted. Since there is no published work in the literature on the thermo-fluid performance of the three-dimensional parabolic-dish collector, therefore, it is not possible to validate our model in the present geometrical configuration. Since the purpose of validation is to prove the correctness of algorithms, solvers and other related parameters, the process of model validation is performed with the only available experimental study [Melchior et al. 2008] for the similar process although the geometric configuration of the dish-receiver system is not identical. The configuration of the experimental solar reactor is shown schematically in Fig. 3.10.

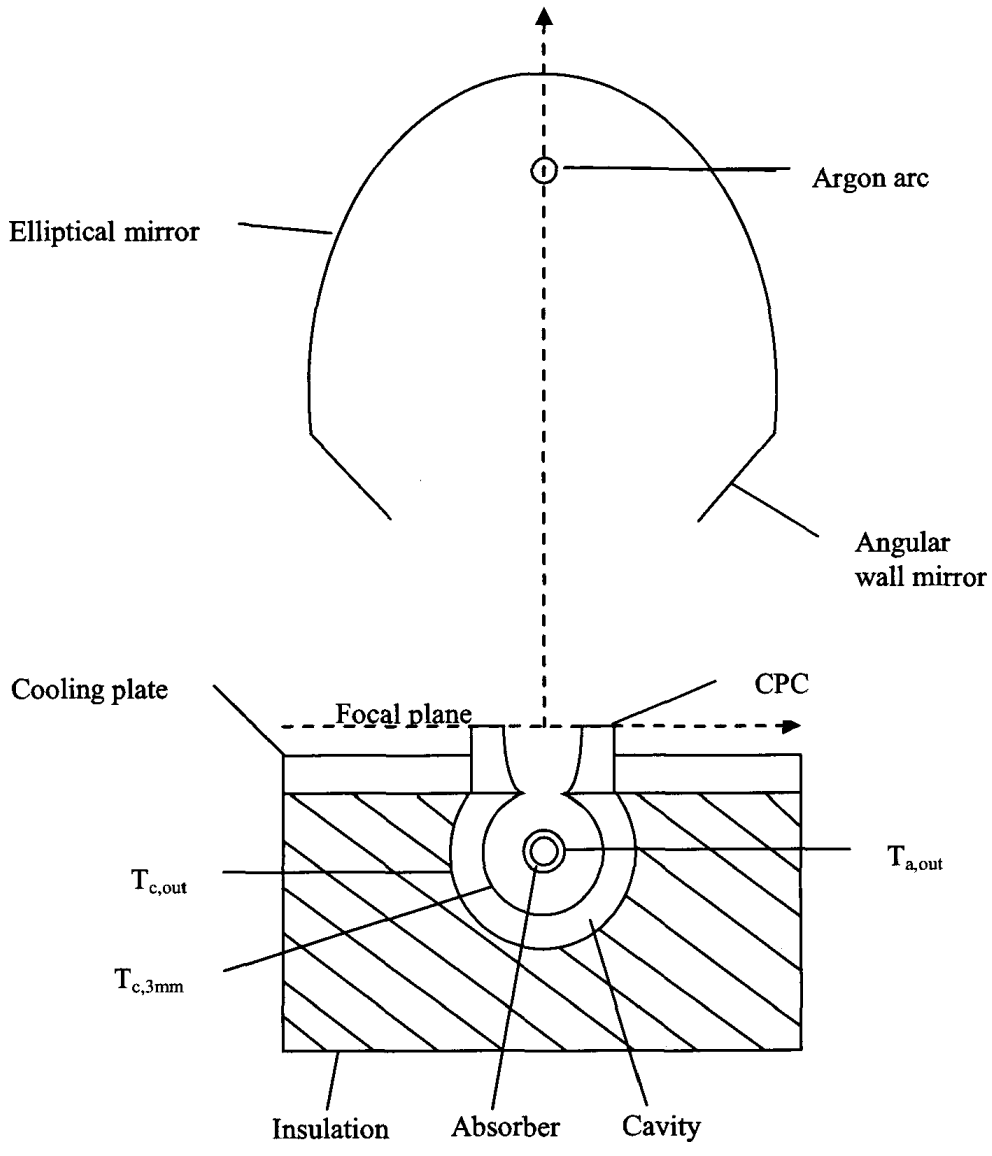

Fig. 3.10: Schematic of the experimental cavity-solar receiver

The radiation source is a high-pressure Argon arc enclosed in a 2.7cm-diameter 20cm long water-cooled quartz envelop and closed-couple to a precision optical reflector to produce an intense beam of concentrated thermal radiation, mainly in the visible and IR spectrum. The arc is positioned at one of the linear foci. The focusing mirror is a horizontal trough with an elliptical cross section and is positioned with the second linear foci. The elliptical mirrors with semi-major axis of length 1.04 m and semi-minor axis of length 0.69 m are truncated so that the reflected beam-down radiation is confined within an angular range of 45 degree. The focal plane is defined as the horizontal plane perpendicular to the ellipse's major axis containing the second linear focus. Power, power fluxes and temperatures of the system are adjusted by simply changing the electrical input power of the Argon arc electrodes.

The cylindrical cavity receiver is made of 10 wt% YO_2-stabilized ZrO_2, with an inner radius of 2.54 cm and an outer radius of 3.81 cm. The cavity is lined with Al_2O_3 insulation layer. The solar cavity also has a windowless slab aperture with rectangular shape of width 1.414 cm and length 15 cm. The tubular absorber has an inner radius of 0.95 cm and an outer radius 1.27 cm. It is positioned concentric with the cylindrical cavity. Compound parabolic concentrators (CPC) are placed at the receiver's aperture in tandem with the primary concentrating system, i.e. the elliptical reflector, and a water-cooled copper plate is incorporated to the CPC. The rectangular entrance of width 2 cm and length 15 cm is at the focal plane of the solar concentrating system. Temperatures are measured at three locations: at the outer surface of the tubular absorber ($T_{a,out}$), at 3 mm behind the inner cavity surface ($T_{c,3mm}$), and at the outer cavity surface ($T_{c,out}$) (see Fig.13). For more details see Melchior et al. [2008].

For validation purpose, a model with exactly the same dimensions as the experimental elliptical-trough reflector and solar reactor is developed. The computational domain includes all the parts of the experimental model except the large insulation layer. The same algorithms and solvers as for the primary model are used in the validation model. In the study of Melchior et al. [2008], the information of cooling plate and insulation is not given. Therefore, the temperature at the outer cavity surface ($T_{c,out}$) will not be computed by the validation model. Since the maximum temperature at the outer cavity surface from the experiments [Melchior et al., 2008] is quite low comparing with the other two

locations, instead of assuming large insulation layer, the constant temperatures at the outer cavity surface measured from the experiments are defined as boundary conditions in our validation model. The conduction heat transfer of the elliptical reflector and CPC are not taken into consideration since they have negligible impacts on the thermal performance of the solar reactor. The convection heat transfer and Buoyancy effect in the hollow area of the solar reactor are negligible in this simulation. Argon arc is defined as a line element radiating flux only on the solar spectrum. The thermophysical and radiative properties of ceramic materials are defined at different temperatures [Touloukian et al., 1970 and Touloukian et al., 1972].

Hemicube method is used to calculate shadowed view factors in order to speed up the simulation without compromising the accuracy by setting fixed subdivision to 2. Shadow checks are enabled to account for shadow effect. The roughness of the surface is ignored. Oppenheim method is used to simulate radiative interchange by using a radiosity approach [FEMAP-TMG User's Guide, 2006]. Space enclosure at 298 K is created to absorb spillage radiation. Stefan-Boltzmann constant is 5.6696E-8. Radiation patch is enabled to significantly reduce computation time on this large model with complex radiative exchange. Iteration limit of thermal solver is 10000. Mixing Length model is used. Second Order Upwind advection scheme is selected. Concurrent solver is set to communicate every flow iteration and the convergence criteria for flow solver is when the residuals of global momentum, mass and energy are smaller than 0.0002. The grid independence tests are conducted to match the mean flux at CPC entrance for the elliptical reflector, and compare the temperature at the inner absorber surface for the solar reactor, respectively.

The first step of validation process is to compare the measured mean flux at CPC entrance from the experiments [Melchior et al., 2008] with the mean flux at CPC entrance from the simulations. These results are shown in Table 3.5. The results show that when electrical power input increases, the mean flux at CPC increases accordingly. The simulation results from our validation model are slightly higher than the measured values with the maximum percent different of 9.0% when electrical power input is 61.458 kW. This is because the arc envelope is internally cooled by a swirling film of de-ionized water that rapidly flows through the plasma arc and the clear quartz lamp tube in the

experimental model; therefore, it results in losing radiative power [Hirsch et al. 2003]. A ± 8% error was recorded in the experiments when the incoming flux at the focal plane was measured optically on a Al_2O_3-plasma-coated Lambertian target with a CCD camera equipped with optical filters and calibrated with a Kendall radiometer [Melchior et al., 2008].

Power input (kW)	Measured mean flux (kW/m^2) [Melchior et al.,2008]	Simulated mean flux (kW/m^2)
15.625	335	337
36.458	745	787
61.458	1215	1325
85.417	1769	1842

Table 3.5 Comparison of measured mean flux and the mean flux from the simulations at CPC entrance

Validation of the reactor model in terms of temperatures at the three different locations in Fig. 3.10 is performed. Fig. 3.11 presents the comparison between the experimentally measured and numerically simulated incident radiative flux at the focal plane for different values of the input radiant flux. A very good agreement is observed between the experimental and simulation results. The average percentage difference between the simulations from the present model and the experimental data is 4.6% for heat flux. Fig. 3.12 shows a set of four representative runs carried out with Argon mass flow rate of 1 L/min at four different input radiant fluxes. The results are shown as a function of the incoming solar power per unit length Q_{solar} at the cavity entrance. It represents the comparison of experimentally measured temperatures and simulation results at the inner absorber surface and 3 mm behind the inner cavity surface. Again, excellent agreement is observed between the experimental and simulation results. The plot shows that the maximum temperature difference between the measured and simulation values at the inner absorber surface is 3.8% when the power input is 36.458 kW. In other words, when the mean flux at focal plane reaches 787 kW/m^2 or the incoming power into the cavity per unit length of the absorber is 11.9 kW/m. The maximum temperature difference between the experimental and simulations values at the location 3 mm behind the inner cavity surface is 8.9% when the Q_{solar} is 5.4 kW/m. However, the overall agreement

between the numerical results and the experimental data is very good. The discrepancy may be attributed to the assumptions used in the numerical simulations and the uncertainty in experimental results as mentioned above.

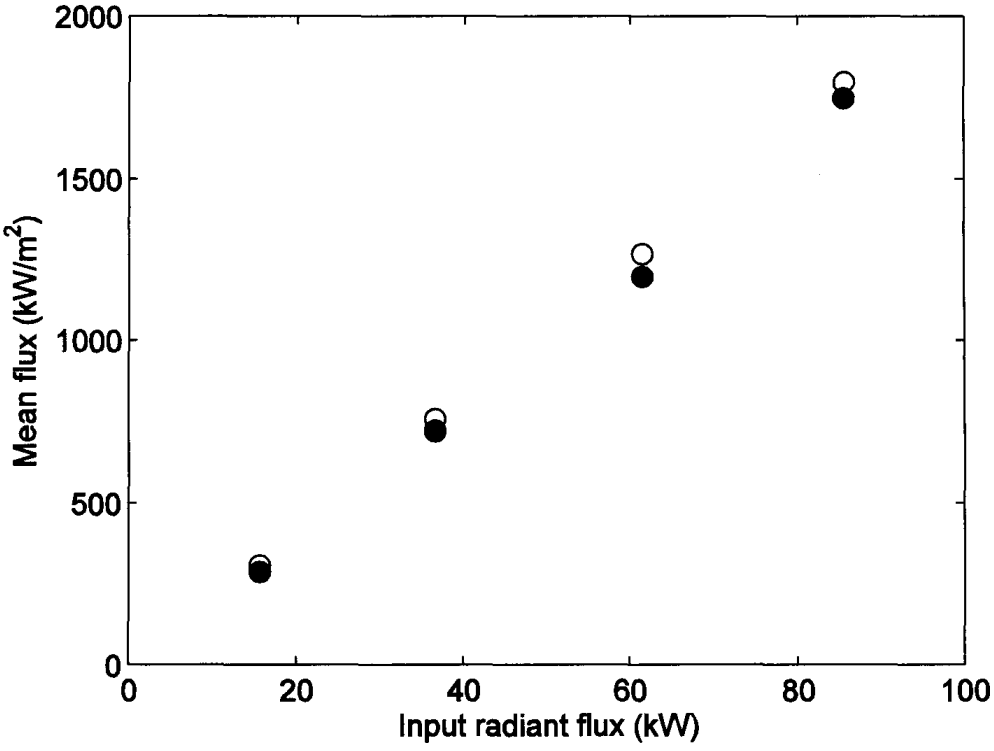

Fig. 3.11: Comparison between the experimentally measured and numerically simulated incident radiative flux at the focal plane for different values of the input radiant flux. Experiment: solid symbol; present model: open symbol.

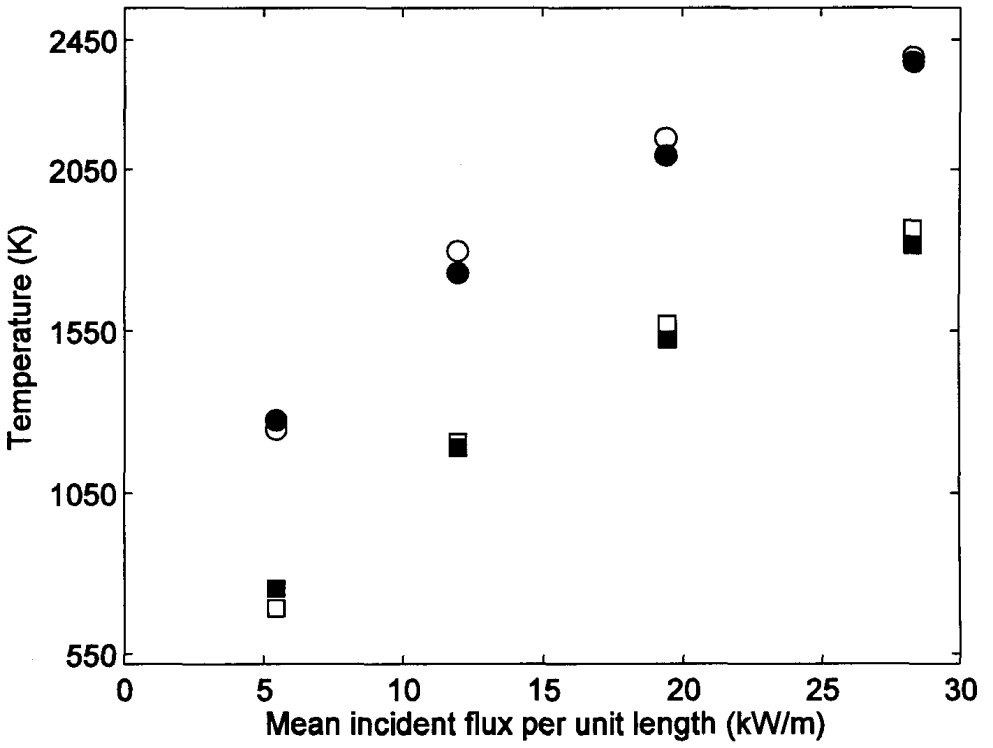

Fig. 3.12: Comparison between the experimentally measured and numerically simulated temperatures at different surfaces versus the mean incident flux per unit length. Circle: Temperature at the inner absorber surface; Square: Temperature at the cavity surface. Experiment: solid symbol; present model: open symbol.

CHAPTER 4: RESULTS AND DISCUSSION

Due to the complex nature of thermo-fluid interactions involved in a parabolic-dish receiver system and the unavailability of detailed study on the thermo-fluid behavior in such system, designing of a parabolic-dish CSE system is challenging. In the present research a detailed parametric study is conducted to examine the influence of different geometric, operating and radiative properties on the performance of a parabolic-dish CSE system.

4.1 Geometrical Parameters

In this section, geometrical parameters such as the aperture size, rim angle and various inlet/outlet configurations are simulated in order to investigate the impacts of these parameters on the temperature distribution of the receiver wall and the working fluid.

4.1.1 The impact of the aperture size

Fig. 4.1 shows the three-dimensional temperature distribution of the receiver wall at different aperture sizes that varies from 0.01 m to 0.05 m The simulations are conducted at the following conditions: reflectivity of the parabolic dish = 0.9, emissivity of the solar receiver=0.8, absorptivity of the solar receiver = 0.8, flow rate of argon gas = 1.15×10^{-4} kg/s, argon enters at ambient conditions from lower tangential inlet and leaves from upper tangential outlet, rim angle of the parabolic dish is 45°. The results show that in the upper three-quarters of the receiver, the wall temperature is nearly uniform for all seven cases. The temperature in the lower portion of the receiver is about 200 K lower than the average wall temperature in the upper section. The results show that aperture size does have an influence on the magnitude of the receiver wall. The circumferentially-averaged incident solar flux on the inner surface of the receiver wall for different aperture sizes is shown in Fig. 4.2. The plot shows a similar trend of incident flux for all cases. That is, the incident solar flux is almost negligible up to a height of 0.08 m and then it increased sharply to the maximum value around 0.11 m and then gradually decreased up to a height of 0.29 m and then increased again at the top surface of the receiver. The negligible flux

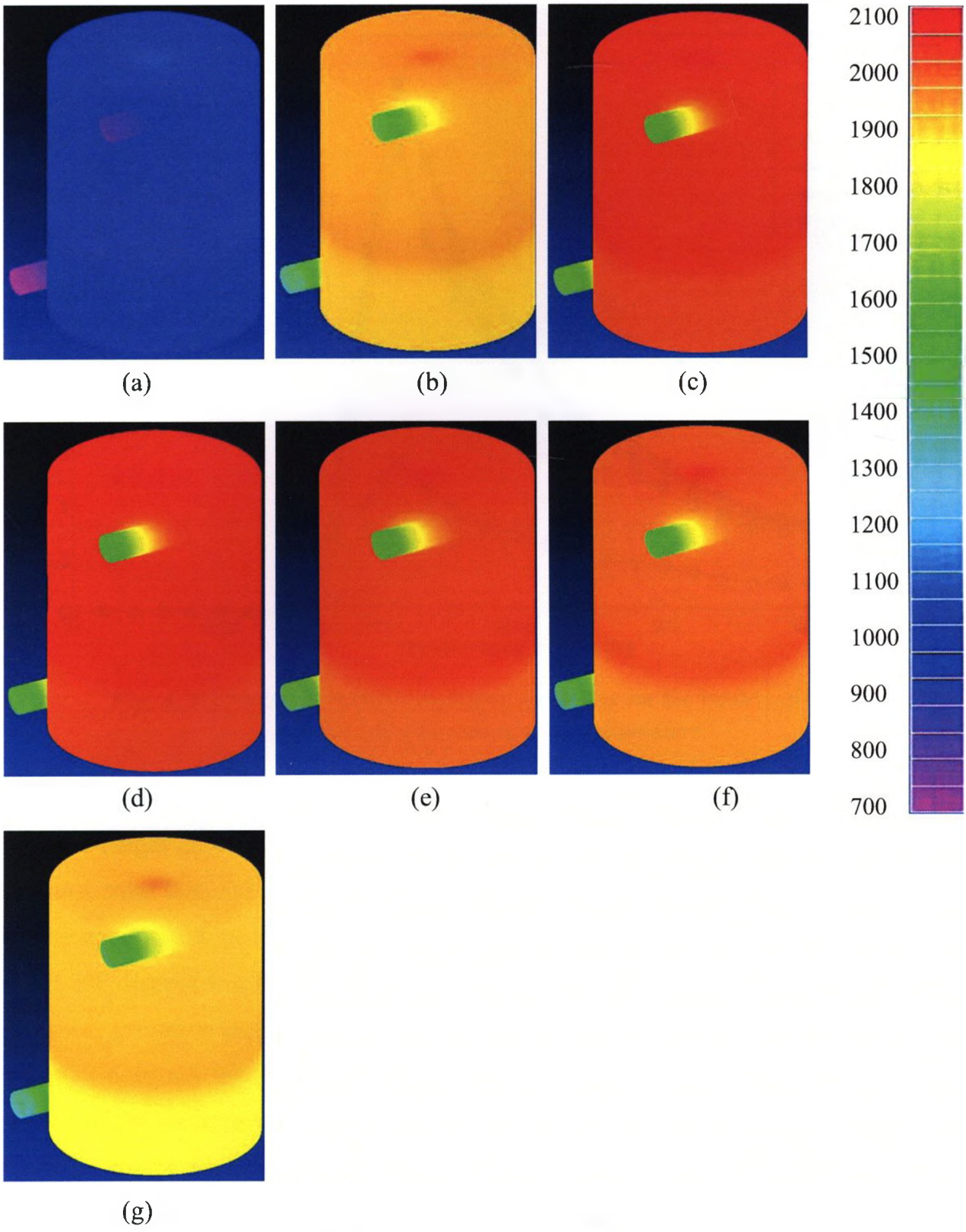

Fig. 4.1: Temperature distribution of the receiver wall at different aperture sizes: (a) 0.01 m; (b) 0.02 m; (c) 0 0.025 m; (d) 0.03 m; (e) 0.035 m; (f) 0.04 m; (g) 0.05 m. The colorbar is in Kelvin.

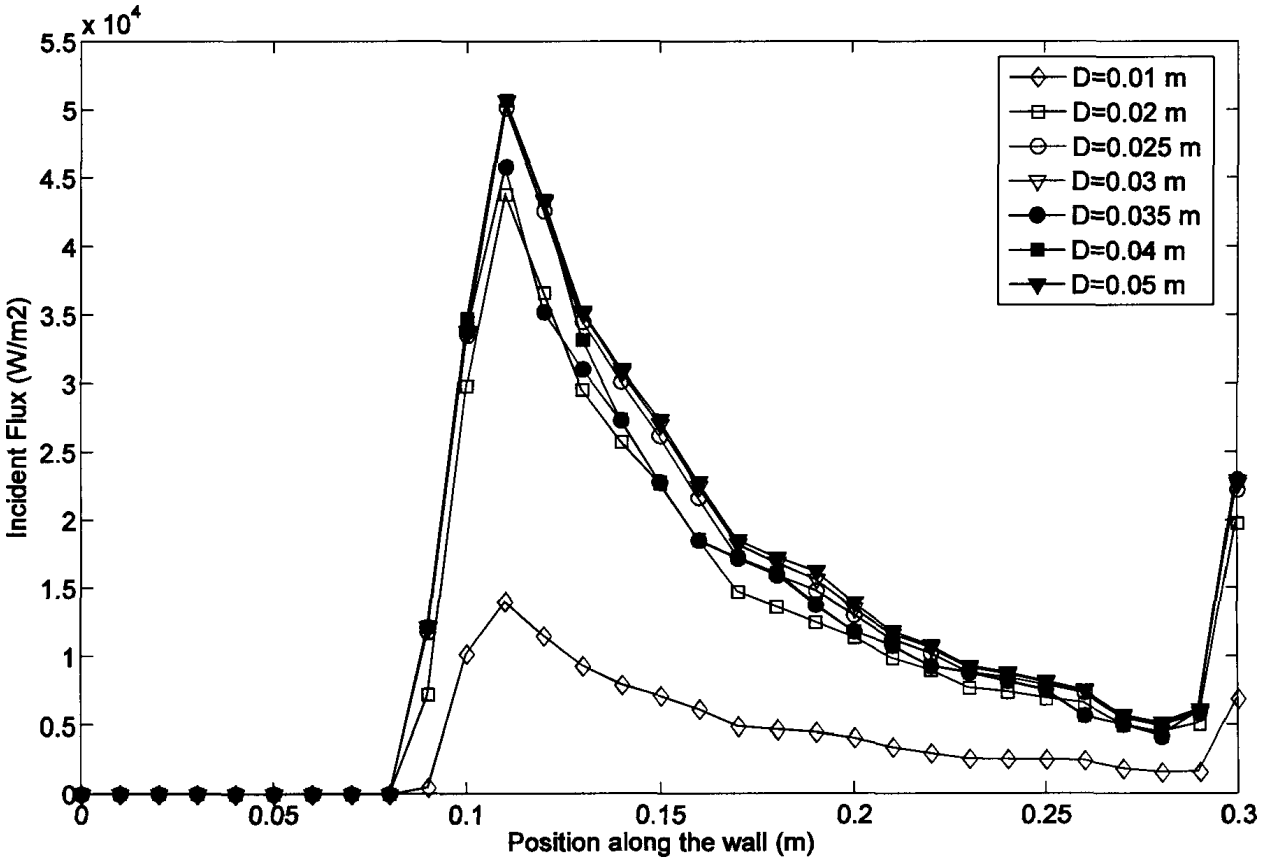

Fig. 4.2: Circumferentially-averaged solar flux on the inner wall of the solar reactor with different aperture diameters.

within a height of 0.08 m is due to the reason that when the radiation enters from the aperture, solar flux could not reach this section of the receiver; due to the shadow caused by the aperture edges. Fig. 4.1 shows that although the temperature in this section is about 200 degrees less the upper section, but it is still significantly high. For most of the cases it is greater than 1700 K. This could be due to the reason that although the incident radiation does not reach this section but due to the multiple reflections from the other section of the receiver, radiation reaches this section. Since the aperture size is relatively small as compared to the diameter of the receiver, the re-radiation loss through the aperture is very small so that most of the rays are captured inside the receiver through multiple reflections. Furthermore, as the maximum incident heat flux occurred slightly above this height, the heat conduction from the high incident flux region also contributes to the increase in temperature in this region. The plot also shows that the maximum incident solar flux along the receiver height occurred at the aperture diameters of 0.025

and 0.03 cm. Except for the peak location, the incident solar flux is quite comparable for different aperture diameters except for the aperture diameter of 0.01 m where the incident solar flux is significantly lower than the other cases over the entire length of the receiver. The peak incident flux for this case is more than a factor of three lower than that for the other aperture sizes. This significant drop is likely due to the reason that the aperture size became smaller than the diameter of the radiation beam focused at the aperture location of the receiver and as a result a fraction of concentrated radiation is blocked from entering the receiver.

The fluid temperature distribution in the multi-parallel horizontal planes of the receiver is shown in Fig. 4.3 for the same cases. The results clearly show gradual heating of the argon gas in the receiver which is an expected behavior. The results show that the argon gas that entered at the ambient conditions is heated up to approximately 1850 K by the solar radiation when the aperture size is 0.025 m, before leaving from the upper tangential outlet. The results also show the effect of flow swirl induced by the tangential inlet. This effect is clearly visible in the top horizontal plane, particularly at the aperture size of 0.025 m and also the bottom plane in Fig. 4.3(h). Due to the swirl, the flow took a longer path along the circumference of the wall. This allowed a longer contact of fluid with the wall which resulted in an enhanced heat transfer from the wall to the gas. The temperature contours in the bottom horizontal plane (i.e. at the inlet level) shows that the argon started to heat up in the tangential inlet pipe even before entering the receiver (see Fig. 4.3h). This is due to the heat conducted from the receiver wall to the inlet pipe whose temperature for most cases reached up to 1500 K (see Figure 4.1). The plots show that the gas heats up from the inlet temperature of about 300 K up to approximately 600 K within the inlet pipe.

The circumferentially-averaged values of the argon gas temperature are plotted in Fig. 4.4 versus the receiver height for different aperture sizes. The results show an almost linear increase in the argon gas temperature with the height except within the bottom 0.01 m height where the gas temperature remained almost constant. The higher temperature of gas in the inlet section of the receiver is due to the heating of gas in the inlet pipe as mentioned above. The results also show that the magnitude of argon temperature varies within about 200 degrees as the aperture size changes from 0.05 m to 0.02 m. However

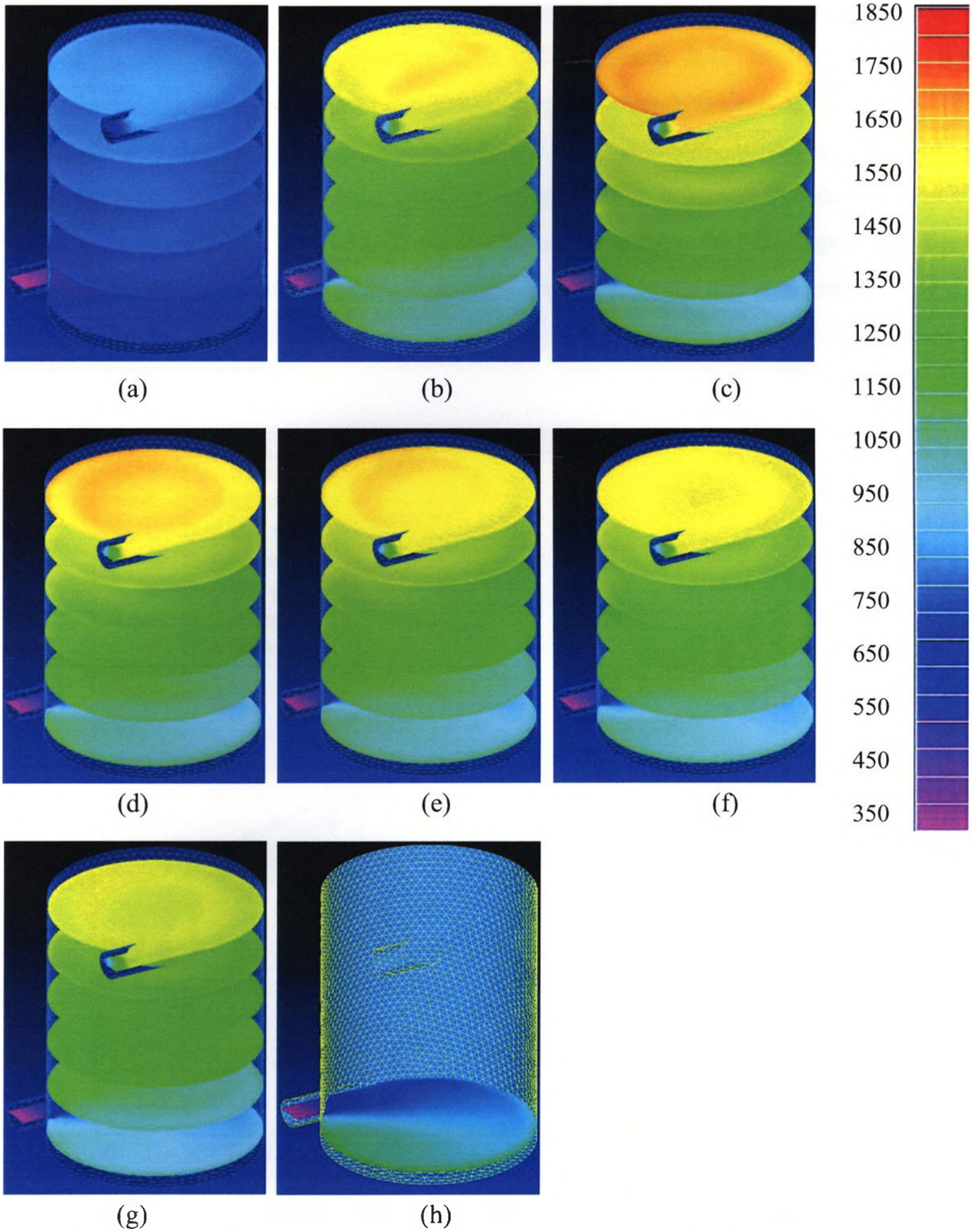

Fig. 4.3: Temperature distribution of the argon gas at different aperture sizes: (a) 0.01 m; (b) 0.02 m; (c) 0 0.025 m; (d) 0.03 m; (e) 0.035 m; (f) 0.04 m; (g) 0.05 m; (h) bottom cutting plane at the aperture size of 0.025 m. The colorbar is in Kelvin.

significant drop in the argon temperature is observed as the aperture size is further reduced to 0.01 m. As the aperture size reduces from 0.02 m to 0.01 m, the circumferentially averaged argon temperature drops by over 300 degrees in the receiver inlet plane and this difference increases with the receiver height. In the receiver outlet plane, the argon temperature at the aperture size of 0.01 m is almost 800 degrees lower than that at the aperture size of 0.02 m. As discussed earlier, the blockage of incident radiation due to the smaller aperture diameter is responsible for this temperature drop of the argon gas.

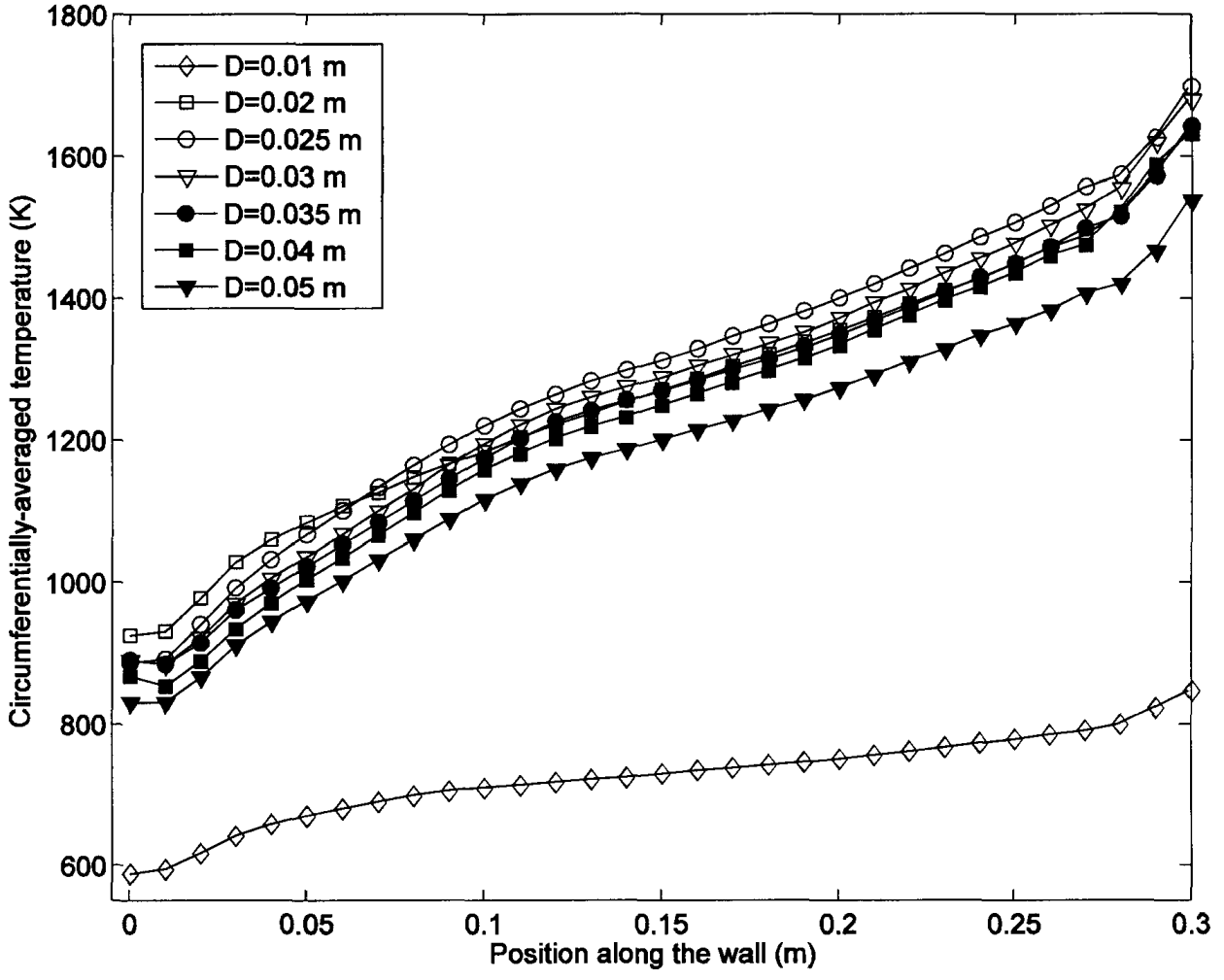

Fig. 4.4: Circumferentially-averaged temperature of argon with different aperture diameters.

Fig. 4.5 presents the average temperature of the receiver wall and the average temperature of argon gas in the receiver and at the outlet. The average argon gas

temperature at the outlet is calculated in the cross-sectional plane at the exit of the cylindrical receiver. Fig. 4.5 shows that as the aperture size reduces from 0.05 cm, the average wall and average argon temperatures gradually increase up to the aperture size of 0.025 cm. With a further decrease in the aperture size, these temperatures started to decrease. This shows that the optimal aperture size for this system is 0.025 cm. The plot also shows that the temperature decrease from the aperture size of 0.025 m to 0.02 m is gradual but as the aperture size further reduced, all temperatures dropped significantly due to the reason discussed earlier. As the aperture size reduces from 0.05 m to 0.025 m, the average wall temperature, and average argon temperature in the receiver and at the exit increased by almost 8%, 9% and 12%, respectively. For the aperture diameter of 0.025 m, the average wall temperature is 1977 K, the average argon temperature in the receiver is approximately 1300 K and the average argon temperature at the exit is 1620 K.

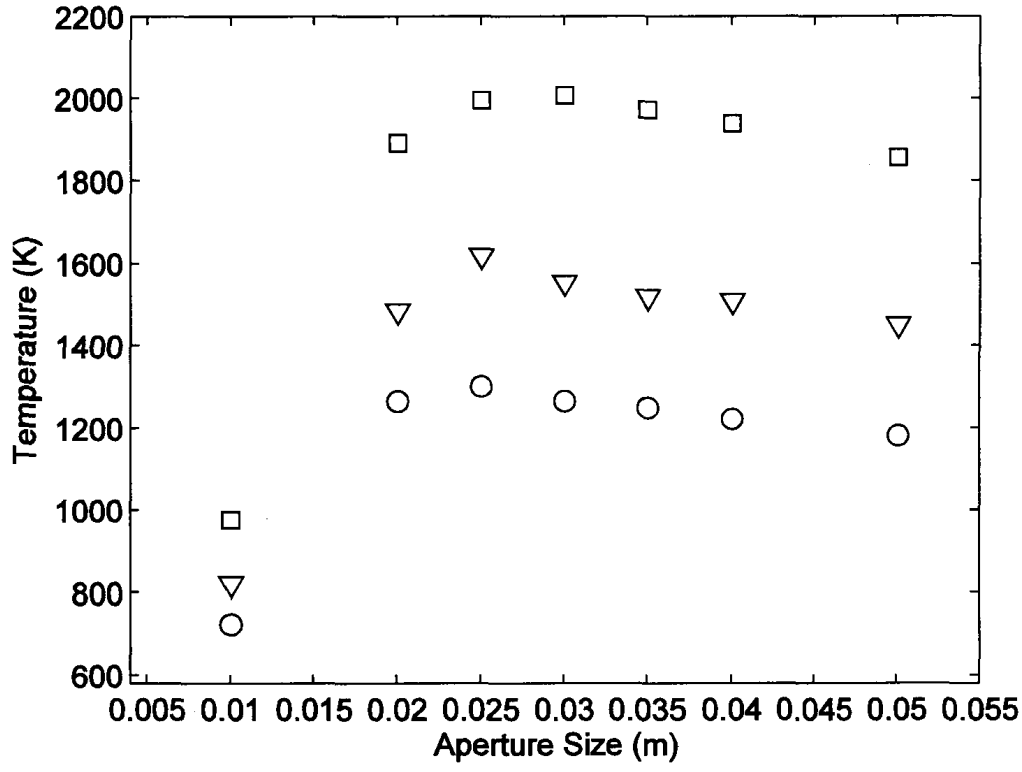

Fig.4.5: Average wall temperature (square), average fluid temperature (circle) and average fluid outlet temperature (triangle) for different aperture sizes of the solar receiver wall.

4.1.2 The impact of the rim angle of the parabolic dish

The impact of the rim angle on the temperature field inside the receiver is investigated for three different rim angles shown schematically in Fig. 4.6. The surface area of the parabolic dish is kept constant for all cases. By varying the rim angle and keeping the same surface area of the parabolic dish the, focal distance is changed accordingly. Therefore, the shape of the paraoblic dish is different for each case, consequently, the distribution of solar flux on the receiver wall is varied. As shown in Fig. 4.6, for larger rim angle, the focal distance is shorter and the curvature of parabolic concentrator is shorter. The schematic in Fig. 4.6 also shows that the height of the lower section of the receiver where the incident solar flux is zero due to the shadow effect increases with a decrease in the rim angle. Thus, the task of changing rim angles is to invesitgate if different solar flux distribution on the receiver wall has an impact on the receiver thermal performance. For this set of simulations, the aperture size of the receiver is set to 0.025 m, the surface radiative properties and the inlet and outlet configuration of the receiver are set the same as in the previous section.

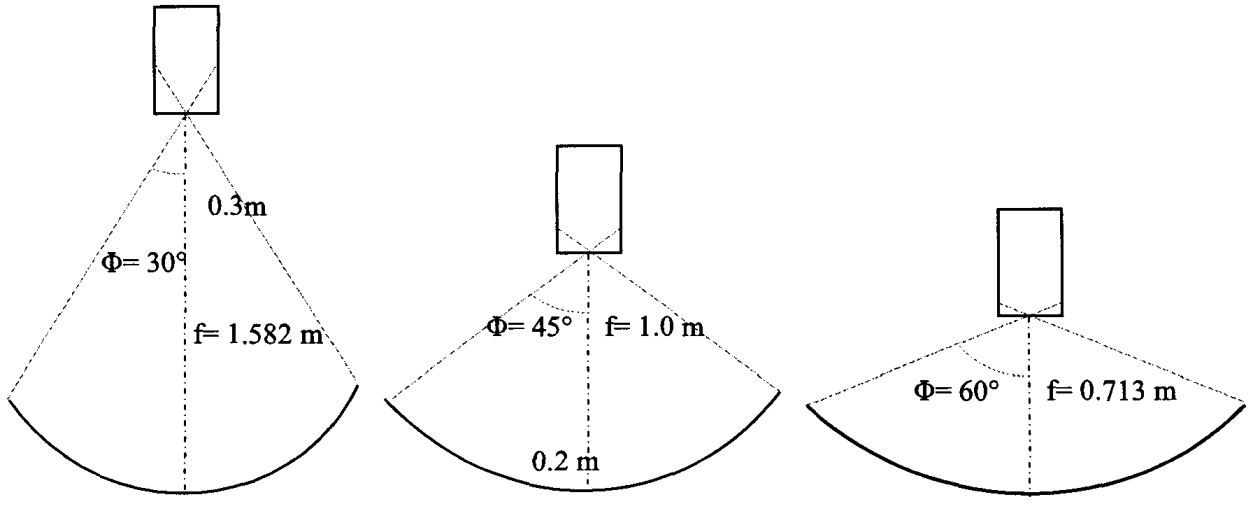

Fig. 4.6: Schematics of different rim angles: (a) 30° (b) 45° (c) 60°.

Fig. 4.7 shows the average temperatures of receiver wall, argon gas in the receiver and argon gas at the outlet for three different rim angles of the parabolic dish. The results show that the rim angle of the parabolic concentrator has negligible effect on the overall thermal performance of the receiver. As mentioned earlier, this could be due to the reason that the radiation loss through the aperture is very small so that most of the radiation is captured inside the reciever through reflection. To further investigate this issue, the circumferentially-averaged incident solar flux on the inner wall of the solar receiver is shown in Fig. 4.8 for different rim angles. The results show that the peak magnitude of the incident flux is largest for the rim angle of 60° which then decreased with a decrease in the rim angle. The peak values occur at 0.06 m, 0.12 m and 0.18 m along the wall for rim angeles of 60°, 45° and 30°, respectively. The figure also confirmed that the height of the bottom region where no incident flux reached, increased with a decrease in the rim angle which is shown schematically in Figure 6. The area under each curve of the solar represents the total amount of the incident flux. The numerical integration shows that the total incident flux is higher for the rim angle of 60° which decreased monotonically with the rim angle. For the rim angles of 45° and 30°, the total incident flux is approximately 10% and 27% lower than that at the rim angle of 60°. The average temperatures however do not show a considerable change with a change in the rim angle. Since the surface area of the dish is kept constant, the same amount of radiant flux is reflected by the dish towards the receiver for all rim angles. As a Thus, any fraction of the radiant flux that is obstructed from entering the receiver is incident on the bottom wall of the receiver and due to the high absorptivity of the wall material, this radiation is mostly absorbed by the bottom wall and conducted to the other sections of the receiver. Futhur investigation must be conducted with the incorpration of optical ray tracing to confirm this behavior.

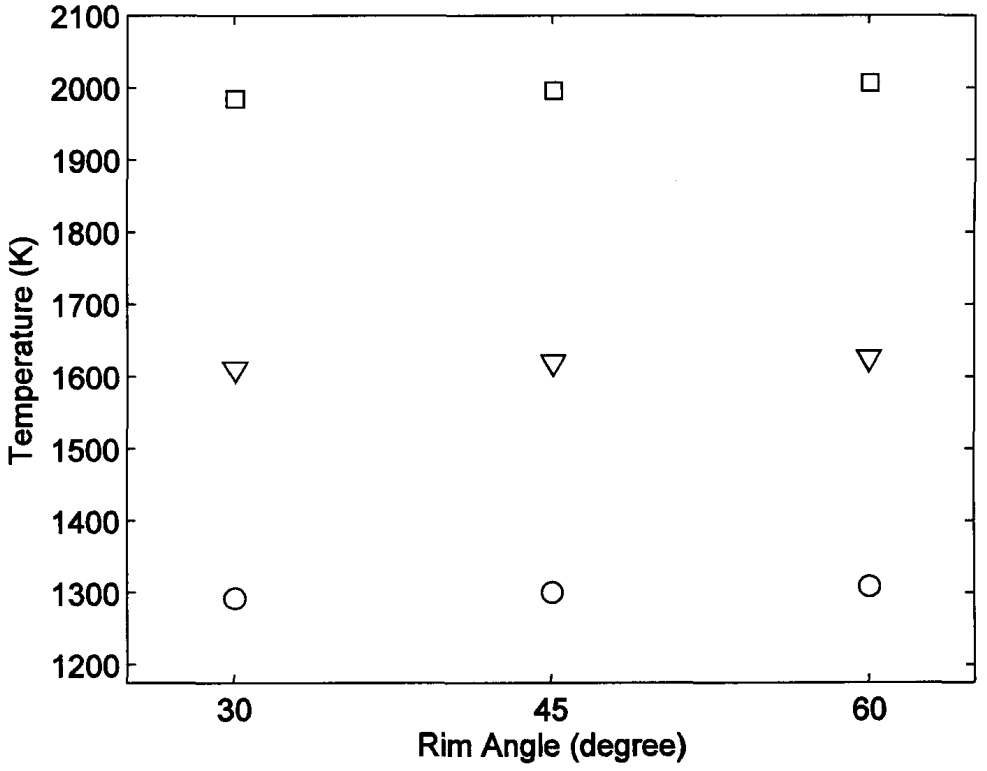

Fig. 4.7: Average wall temperature (square), average fluid temperature (circle), and average fluid outlet temperature (triangle) for different rim angles of the parabolic dish.

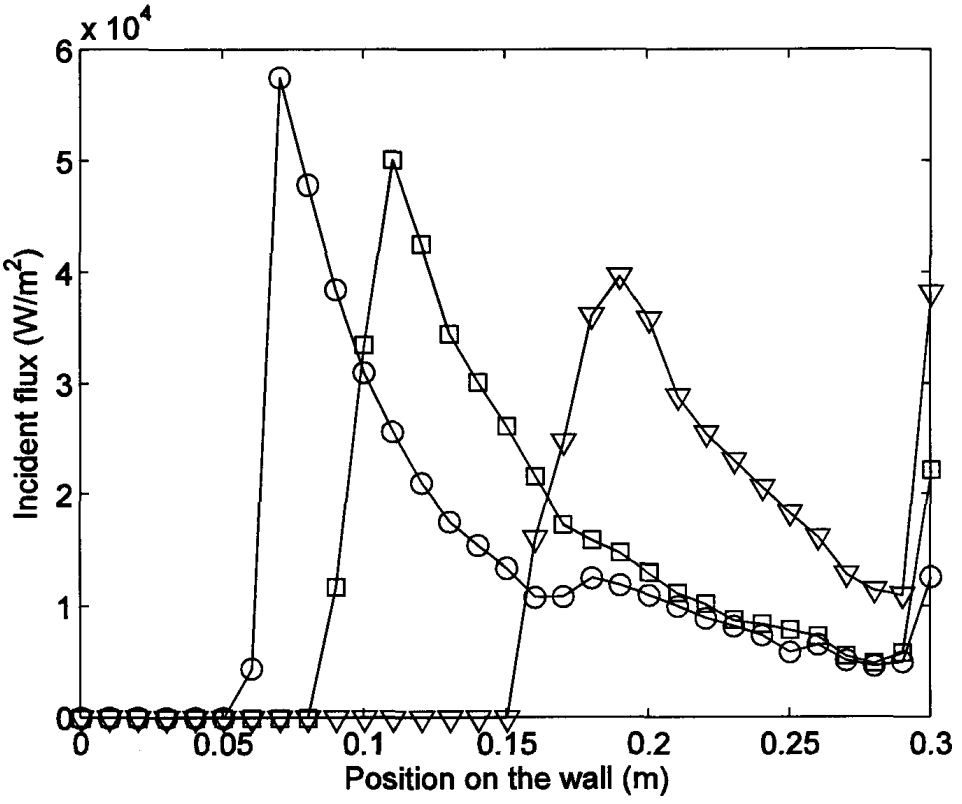

Fig. 4.8: Circumferentially-averaged solar flux on the inner wall of the solar reactor with different rim angles(circle:60°, square:45°, triangle; 30°).

4.1.3 Different inlet/outlet configurations

The impact of the inlet and outlet positions on the performance of the receiver is investigated for different inlet/outlet configurations of the receiver shown in Fig. 4.9. These configurations are: (1) a tangential inlet located at the bottom and a tangential outlet located at the top; (2) a tangential inlet located at the top and a tangential outlet located at the bottom; (3) a tangential inlet located at the bottom and a normal outlet on the top surface; (4) a tubular inlet from the top, extended into the receiver up to a distance equal to half of the receiver height and a concentrical normal outlet located at the top surface; (5) a tubular inlet from the top, extended into the receiver up to a distance equal to three-quarters of the receiver height and a concentrical normal outlet located at the top surface; (6) a tangential inlet located at the bottom and a tangential outlet located at the top; (7) a tangential inlet located at the top and a tangential outlet located at the bottom. Note that the orientation of the tangential inlet/outlet for cases (1) and (2) are different from that for cases (6) and (7). All seven cases are simulated with the following conditions: flow rate = 1.15×10^{-4} kg/s, argon enters at ambient conditions, buoyancy effect is considered, rim angle = 45° and aperture size =0.025 m. The surface radiation properties are the same as in the previous section.

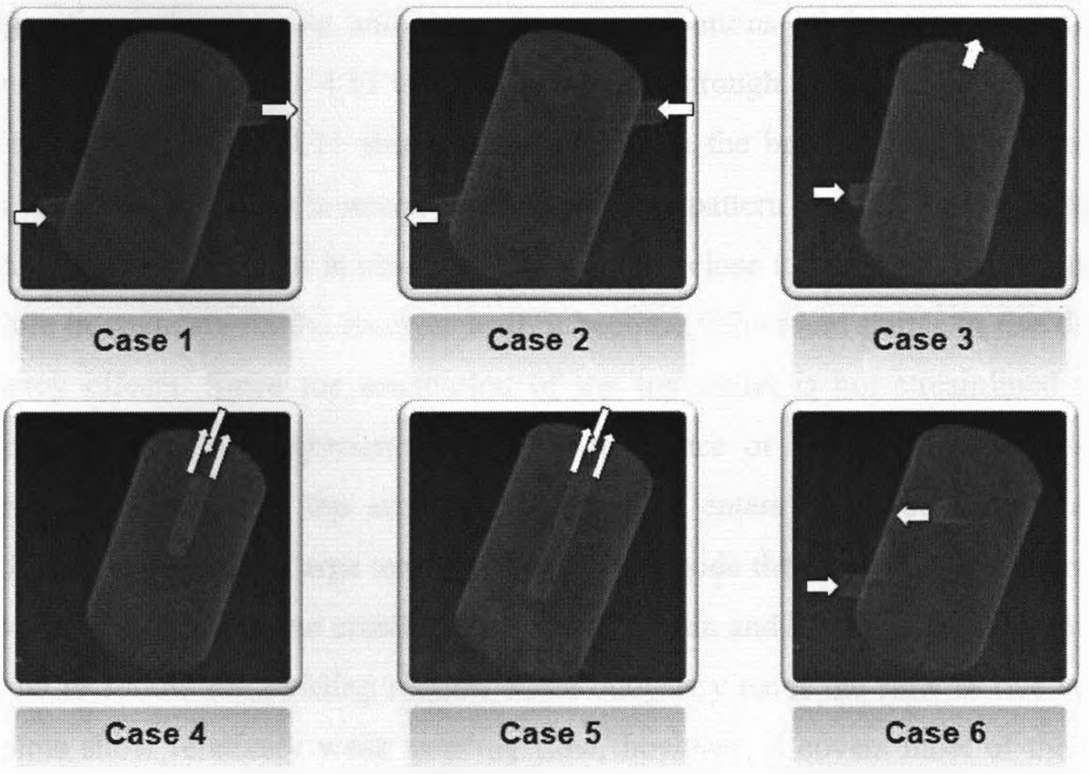

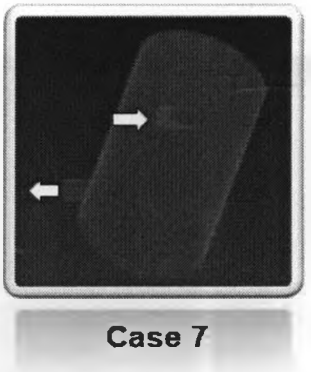

Fig. 4.9: Different inlet/outlet configurations.

Fig. 4.10 shows the temperature distribution on the inner surface of the receiver wall for different inlet/outlet configurations. Cases 1, 2 and 7 show higher temperatures than other four cases. Case 3 shows lowest values of the wall temperature. The wall temperature distributions of seven cases show similar patterns. The upper two thirds section of the receiver wall shows approximately 200 K higher than bottom part and the temperature distribution in each section is almost uniform.

To investigate the thermo-fluid behavior inside the receiver for different inlet/outlet configurations, the velocity and temperature distributions of the argon gas inside the receiver are shown in Fig. 4.11 to 4.17 for cases 1 through 7, respectively. The velocity field for case 1 in Fig. 4.11 shows that the flow in the bottom inlet plane accelerates along the receiver wall as it enters, with the swirling pattern over the half circumferential length. An upward current is observed in the region close to the outlet. As the gas heats up while in contact with the receiver wall, it become lighter and startes to rise due to the buoyancy effects. Since the orientation of the top outlet is not streamlined with the swirling pattern, flow experiences stronger resistance or higher flow losses (see the velocity contours in the top section). As the flow enters the receiver with a certain velocity and experiences large temperature change inside the receiver, the flow inside the receiver is governed by the combined effects of inertia and buoyancy. The inertia forces the flow to follow the swirling motion while buoyancy tends the flow to rise vertically. The plots show relatively weak swirling flow, however, it covers most of the receiver while the buoyancy-driven vertical flow in the region close to the outlet location which is

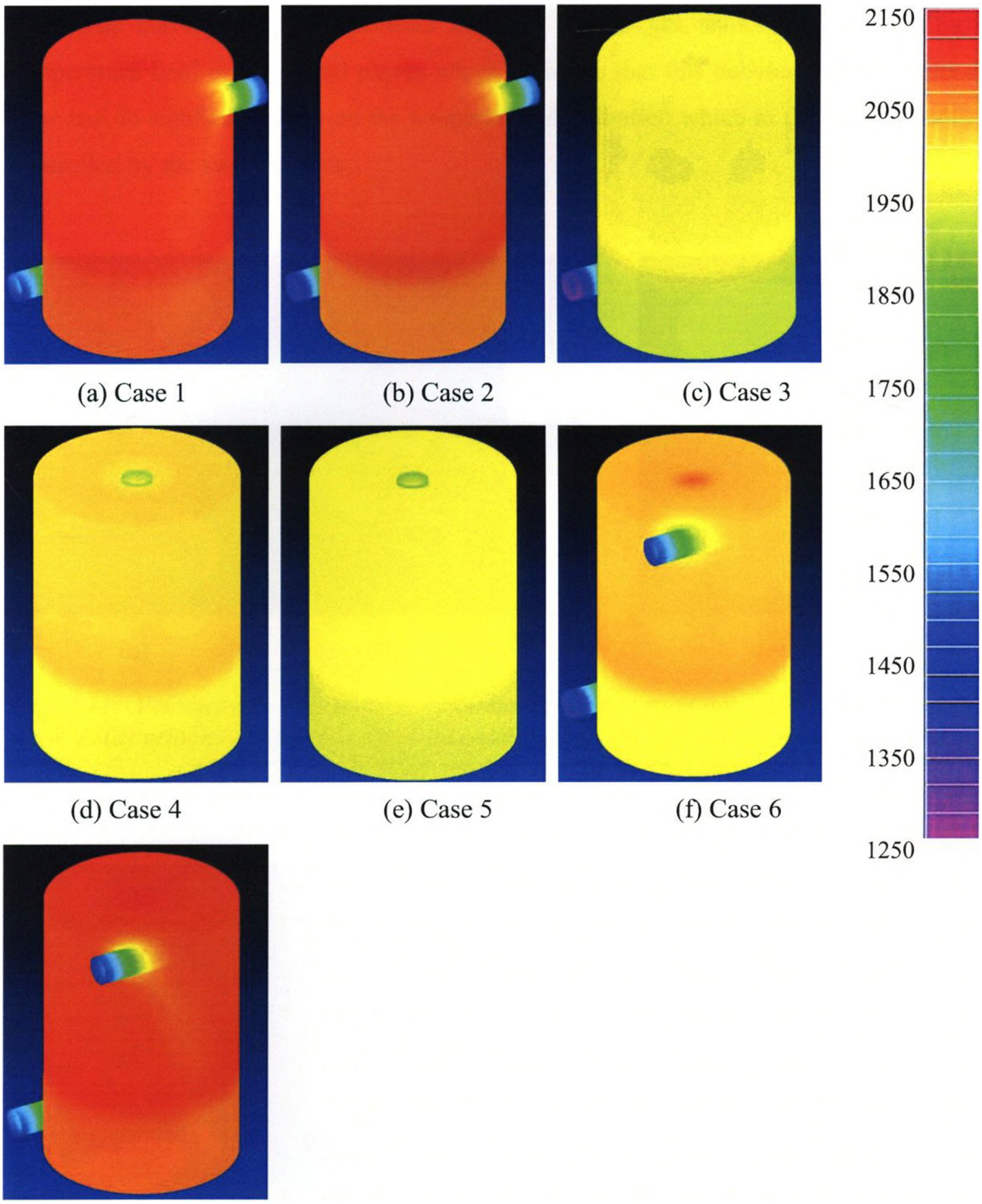

Fig.4.10: Temperature distribution of the receiver wall for different inlet/outlet configurations. The colorbar is in Kelvin.

slightly faster, so the swirling flow is restricted to relatively thin layer adjacent to the wall. The corresponding temperature contours of the gas shows relatively uniform temperature field in horizontal planes which indicates that this buoyancy driven vertical flow has no signficant effect on the temperature distribution which in this case is mainly controlled by the swirling flow.

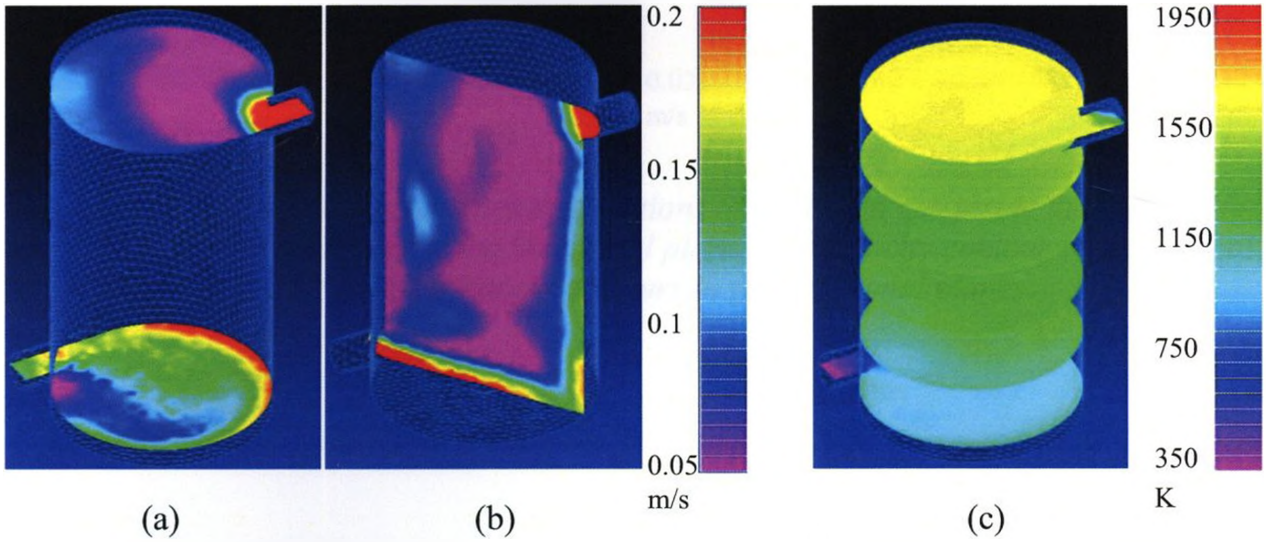

Fig. 4.11: Velocity and temperature distributions of the argon gas inside the receiver for case 1: (a) velocity contours in the horizontal planes; (b) velocity contour in the vertical plane; (c) temperature contours in the horizontal planes.

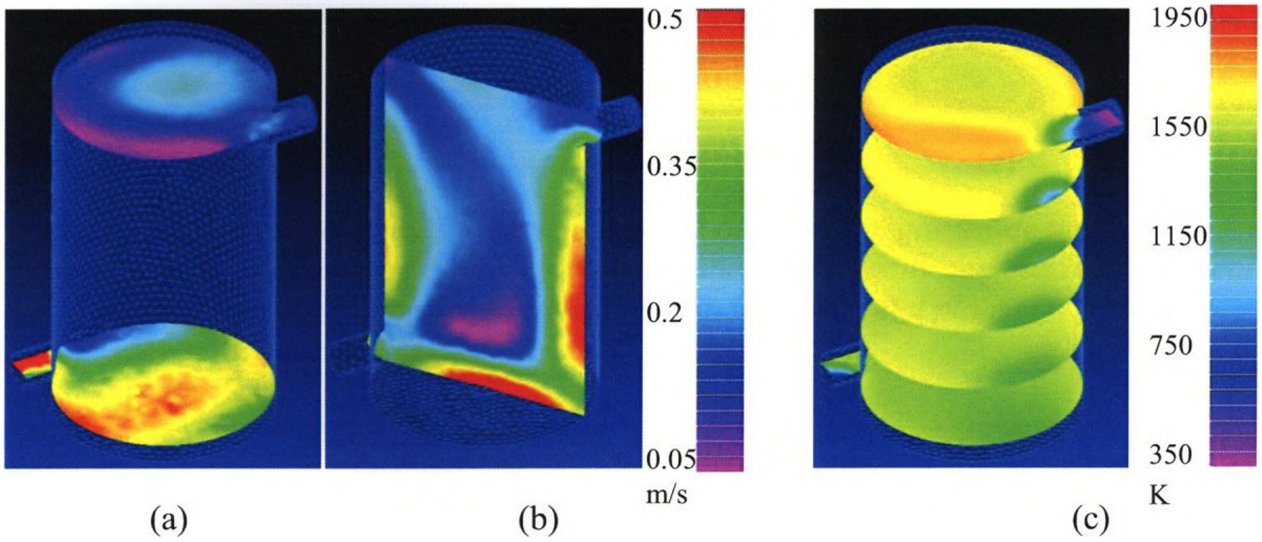

Fig. 4.12: Velocity and temperature distributions of the argon gas inside the receiver for case 2: (a) velocity contours in the horizontal planes; (b) velocity contour in the vertical plane; (c) temperature contours in the horizontal planes.

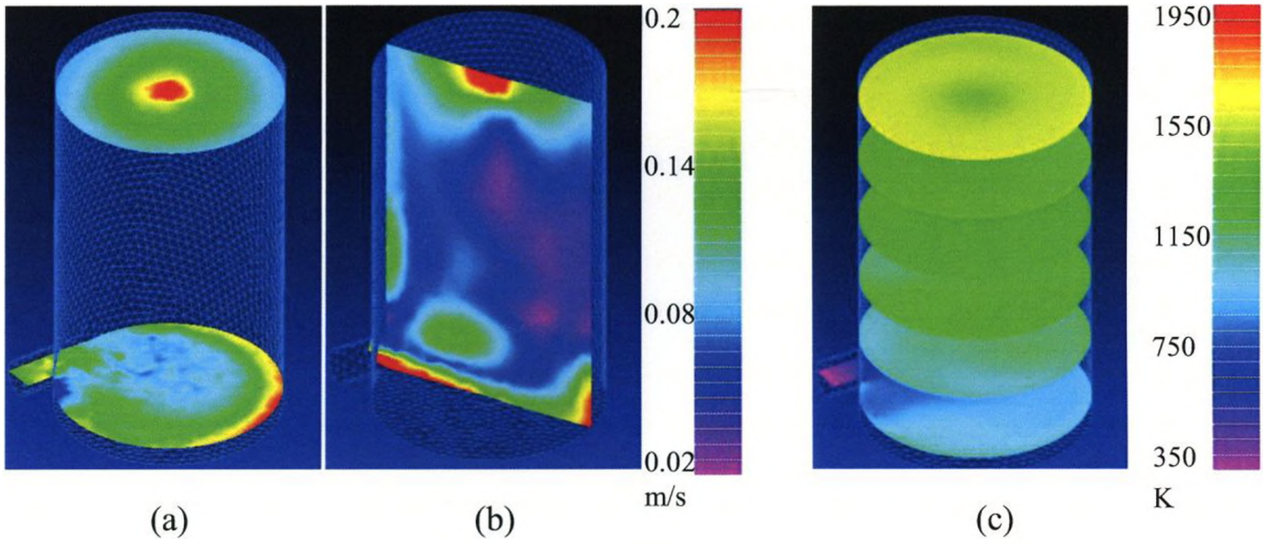

Fig. 4.13: Velocity and temperature distributions of the argon gas inside the receiver for case 3: (a) velocity contours in the horizontal planes; (b) velocity contour in the vertical plane; (c) temperature contours in the horizontal planes.

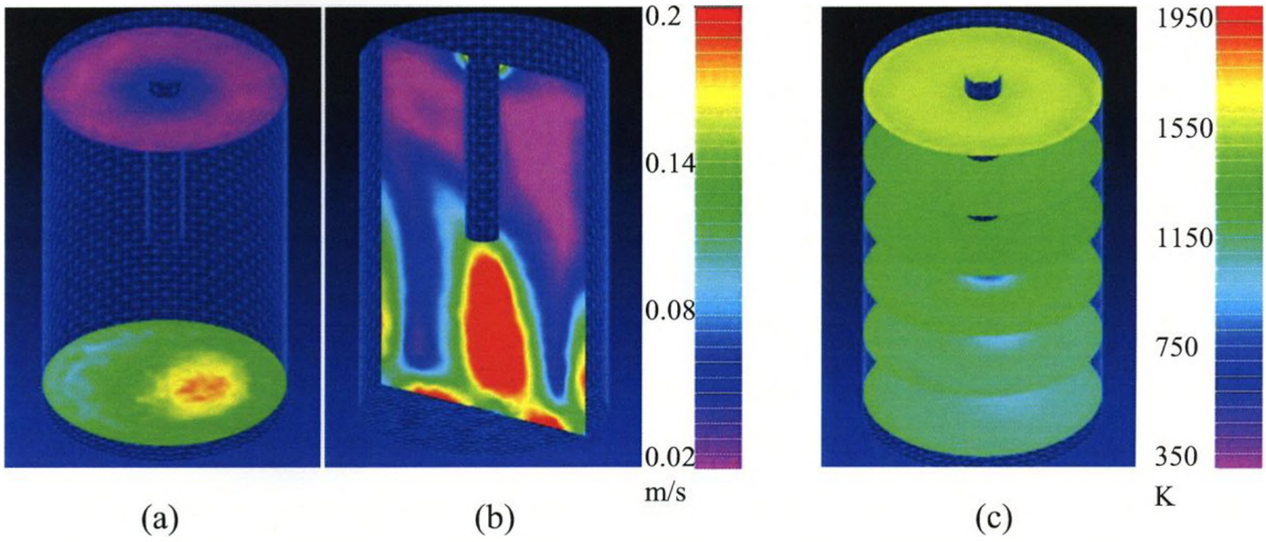

Fig. 4.14: Velocity and temperature distributions of the argon gas inside the receiver for case 4: (a) velocity contours in the horizontal planes; (b) velocity contour in the vertical plane; (c) temperature contours in the horizontal planes.

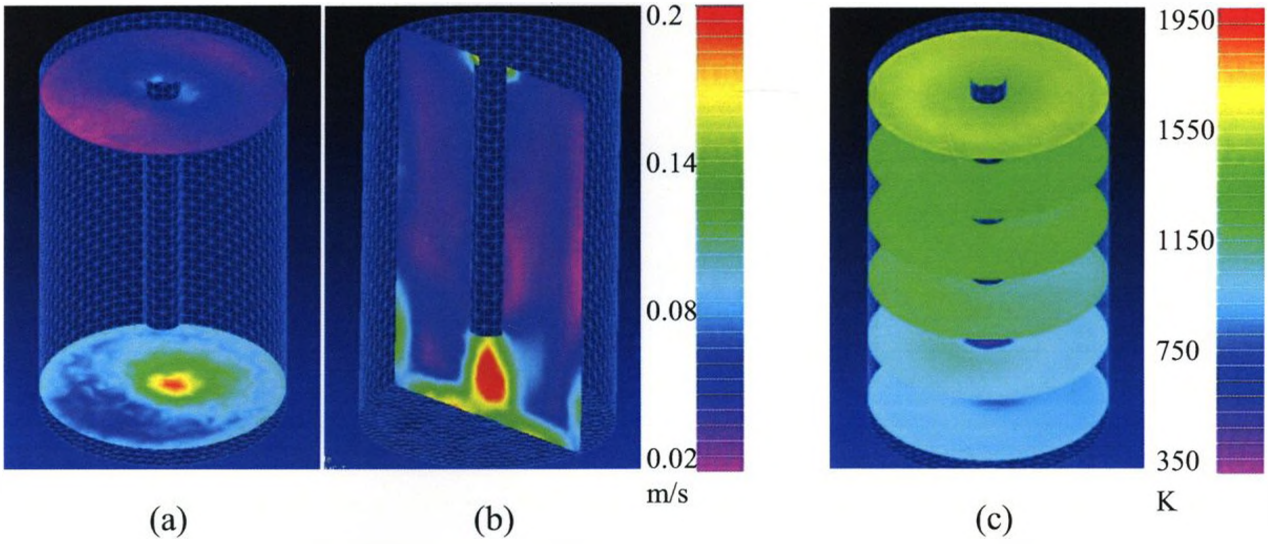

Fig. 4.15: Velocity and temperature distributions of the argon gas inside the receiver for case 5: (a) velocity contours in the horizontal planes; (b) velocity contour in the vertical plane; (c) temperature contours in the horizontal planes.

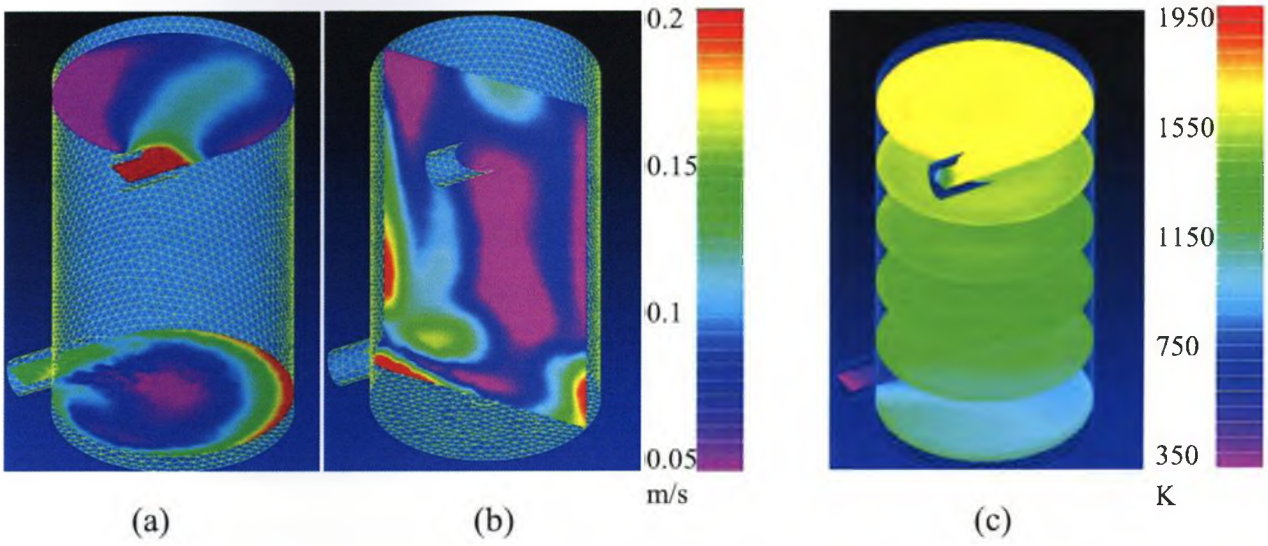

Fig. 4.16: Velocity and temperature distributions of the argon gas inside the receiver for case 6: (a) velocity contours in the horizontal planes; (b) velocity contour in the vertical plane; (c) temperature contours in the horizontal planes.

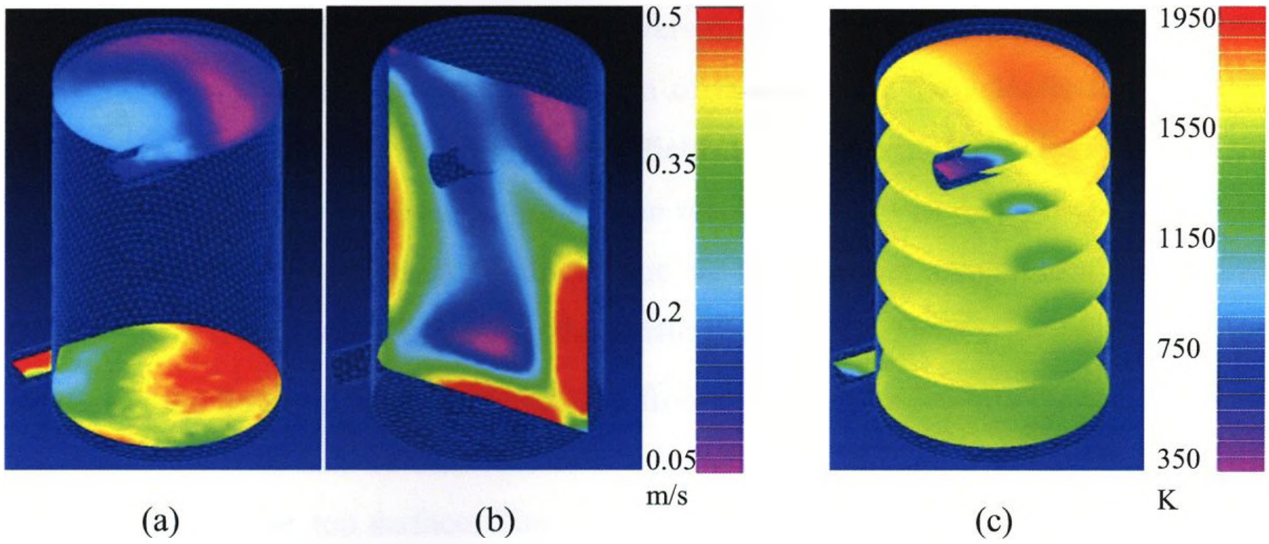

Fig. 4.17: Velocity and temperature distributions of the argon gas inside the receiver for case 7: (a) velocity contours in the horizontal planes; (b) velocity contour in the vertical plane; (c) temperature contours in the horizontal planes.

In case 2, the flow enters from the top and exits from the bottom for the same geometry as in case 1. The plots in Fig 4.12 show that the flow gets deccelerated soon after it enters from the inlet. As the cooler and dense flow enters from the top inlet, the buoyancy tends the fluid to fall. Thus, the flow in this configuration also undergoes the combined effects of inertia and buoyancy. The stronger velocity magnitudes in the outer section as compared to the inner section of the receiver (as observed in the vertical plane) indicates that the swirling effects are significant. However, the velocity magnitudes along the wall are more strong in the region close to the inlet, which indicates that the buoyancy-driven flow is superimposed on the velocity field in this region. In comparison with case 1, the velocity field in case 2 is stronger and has higher variability. The plots also show that the velocity magnitudes in case 2 are in general, more than a factor of two larger than that in case 1. The temperature contours show that the temperature distribution in horizontal planes is not uniform. The stronger velocities and their higher variability is responsible for this variation in the temperature field. The comparison of velocity and temperature fields in the top horizontal plane confirms this trend.

In case 3, the flow enters tangentially from the bottom and exits from an opening in the middle of the top wall. The velocity plots for this case (Fig. 4.13) show that the swirling effects are mainly restricted to the bottom section of the receiver. The velocity

magnitudes in the central region of the receiver are very low. As the flow converges near the top exit, it accelerates. In the top region of the receiver, the velocity field is quite uniform except at the exit. The temperature fields show quite uniform distribution in the upper two-thirds of the receiver. In the bottom section, higher variability in the horizontal temperature field is observed which is due to the stronger magnitudes and higher variablility of the velocity field due to the swirling effects.

In case 4, the flow enters via a tubular inlet from the top, extended into the receiver up to a distance equal to half of the receiver height and exits through a concentrical normal outlet located at the top surface. The velocity contours in Fig. 4.14 show that the flow forms a jet as it exits the inlet pipe. The flow then rises towards the top with higher velocity magnitudes near the receiver wall. In the upper half section of the receiver the velocity field is quite uniform indicating that the flow is relatively well mixed in this region. The temperature plot shows some variability in the lower half of the receiver where the variability and magnitude of velocity field is strong. In the upper half section where the velocity field is uniform, the temperature field also shows uniform behavior. In case 5, the length of the inlet tube is extended to two-thirds of the receiver height. The rest of the geometry is same as in case 4. The velocity fields in Fig. 4.15 show the jet behavior similar to that for case 4 however, the jet flow is restricted to lower one-third of the receiver. The velocity field in the upper two-thirds of the receiver is relatively uniform. The temperature contours show uniform temperature field in the upper section of the reciver where the velocity field is uniform. Variability in temperature field is observed in the jet region.

In case 6, the flow enters from the tangential inlet at the bottom and exits from the tangential outlet at the top. Fig. 4.16 shows the velocity and temperature contours for case 6. The difference between case 1 and case 6 is that the outlet in case 6 is streamlined with the swirling flow. Swirling flow patterns are more dominant in this case as compared to case 1. The comparison also shows that the disruption of the swirling flow pattern in case 1 due to non-streamlined outlet is not present in case 6. The temperature fields for case 6 show signficant variation in the temperature magnitude in the lower and upper sections of the receiver, while the temperature field is relatively uniform in the middle section of the receiver. In case 7, the flow enters from top tangential inlet and

exits from the bottom tangential inlet for the same geometry as in case 6. The velocity plots for this case (Fig. 4.17) show no strong swirling flow in the inlet plane. This could be due to the reason that the buoyancy effects tend to push the swirl downwards. In the middle section of the resonator, higher velocity magnitude are observed near the walls. Since the magnitude of this strong flow velocity is almost symmetric, it indicates that the buoyancy effects are not as significnat as observed in case 2, but rather the swirling effects are more dominant. The temperature field shows higher variability particularly in the upper section which is likely due to the higher variability in the velocity field.

The temperature distribution of the argon gas for different inlet/outlet configurations in Fig. 4.11 to 4.17 shows that the highest temperature occurs at the top for all seven configurations which is expected. Cases 2 and 7 show highest temperature regions close to 2000 K. Case 5 shows smaller temperature gradients in the vertical direction as compared to the other five configurations. The plots show that the change in the argon gas temperature with height is different for different configurations. For case 1, the temperature distribution in horizontal planes is more uniform than other cases. Cases 2 and 7 showed the largest temperature variation in the horizontal planes. These were the cases when the argon gas at the ambient conditions entered the receiver from the tangential inlet at the top section. The plots for cases 4 and 5 show that the length of inlet pipe has an impact on the argon gas temperature distribution. Lower argon gas temperatures are observed for the longer inlet pipe (case 5). As the argon gas at the ambient temperature enters through these pipes, the temperature of these pipes is significantly low which reduces the temperature of argon flowing over these pipes.

The circumferentially-averaged temperatures of the argon gas for different inlet/outlet configurations are shown in Fig. 4.18. Although the temperature of the argon gas at the top section of the receiver is almost identical for all configurations, the plot shows that the variation of gas temperature along the receiver height is different for different configurations. Furthermore, the temperature at the bottom section of the receiver also varies for different configurations. The highest gas temperatures in the receiver are observed for the configurations in cases 2 and 7, i.e. when the gas is injected tangentially from the top and exited from the bottom. There is a small difference in the orientation of the outlet tangential pipes for cases 2 and 7, but the results show that the orientation does

not have a signficant influence on the average gas temperature. The results show that the temperatures in the lower section of the receiver for cases 2 and 7 are on average 300 to 400 degress higher than the other cases. Cases 1 and 6 are identical in geometry to cases 2 and 7, respectively, except the switching of inlet and outlet positions. These results indicate that just the switching of inlet and outlet positions has a significant influence on the argon gas temperature. Cases 4 and 5 which have similar geometry except the for the length of the inlet pipe which is longer for case 5. The results show that the effect of differnt pipe lengths on the argon temperature is relatively small in the upper section of the receiver but in the lower section, it has a significant impact which is likely due to the extent of the jet zone. The gas temperature in the lower section of the receiver is almost 200 degree lower for the case with longer pipe.

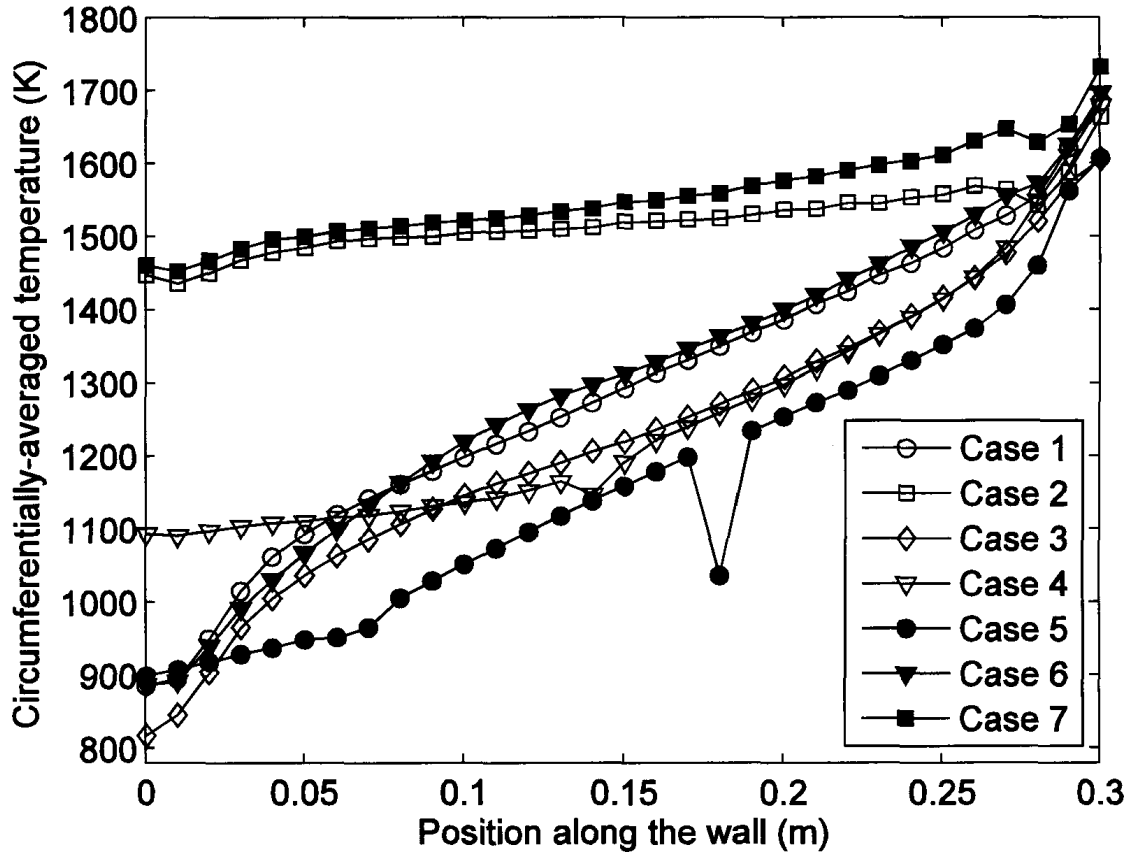

Fig. 4.18: Circumferentially-averaged temperature of argon with different inlet/outlet configurations.

Fig. 4.19 shows the average temperatures of the wall, argon gas in the receiver and at the outlet for different inlet/outlet configurations. The trends for the variation of average wall

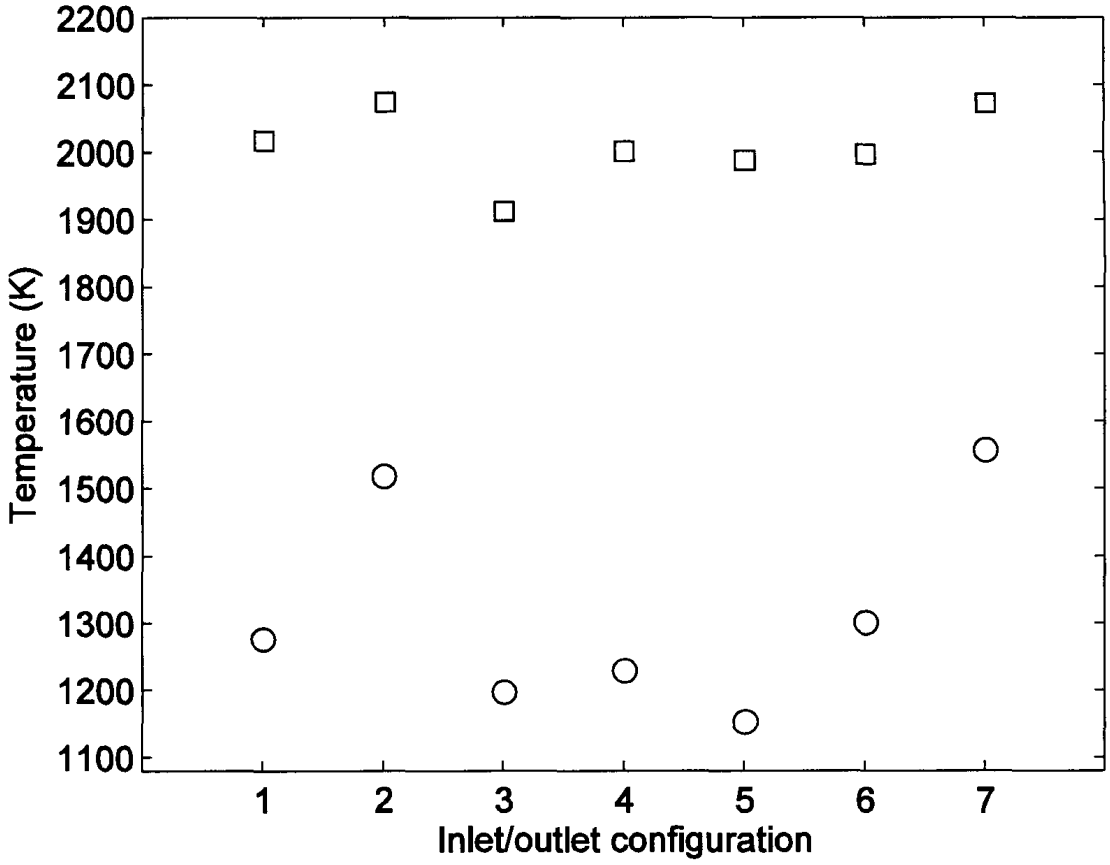

Fig. 4.19: Average wall temperature (square) and average fluid temperature (circle), for different inlet/out configurations.

temperature are similar to that for the average gas temperature for different configurations. Cases 2 and 7 show the highest wall temperature which are close to 2100 K. The argon gas temperature is also higher for these two cases as compared to the other cases, where case 7 has relatively higher gas temperature than case 2. The average argon gas temperature for case 7 and case 2 are 1560 K and 1520 K, respectively. The lowest wall temperature is observed for case 3 which is slightly above 1900 K. The average gas temperature for this case is also relatively low (about 1200 K). The lowest gas temperature of about 1150 K is observed for case 5. The variations in the wall and gas temperatures within the receiver are further quantified in terms of the standard deviations. Fig. 4.20 shows the standard deviations of wall and gas temperatures for each case. It is

found that case 4 has the smallest standard deviation for the wall temperature. This indicates the more uniform temperature distribution on the wall occurs when a pipe of length equal to half the receiver height is used as an inlet and concentrical normal outlet is located at the top surface of the receiver. It is also found that case 2 shows smallest standard deviation of argon gas temperatures. This implies when the tangential inlet located at the top and the tangential outlet located at the bottom, the temperature distribution is more uniform due to better mixing of fluid. The unstable stratification due to the injection of cooler dense fluid from the top also plays a role in enhancing the mixing.

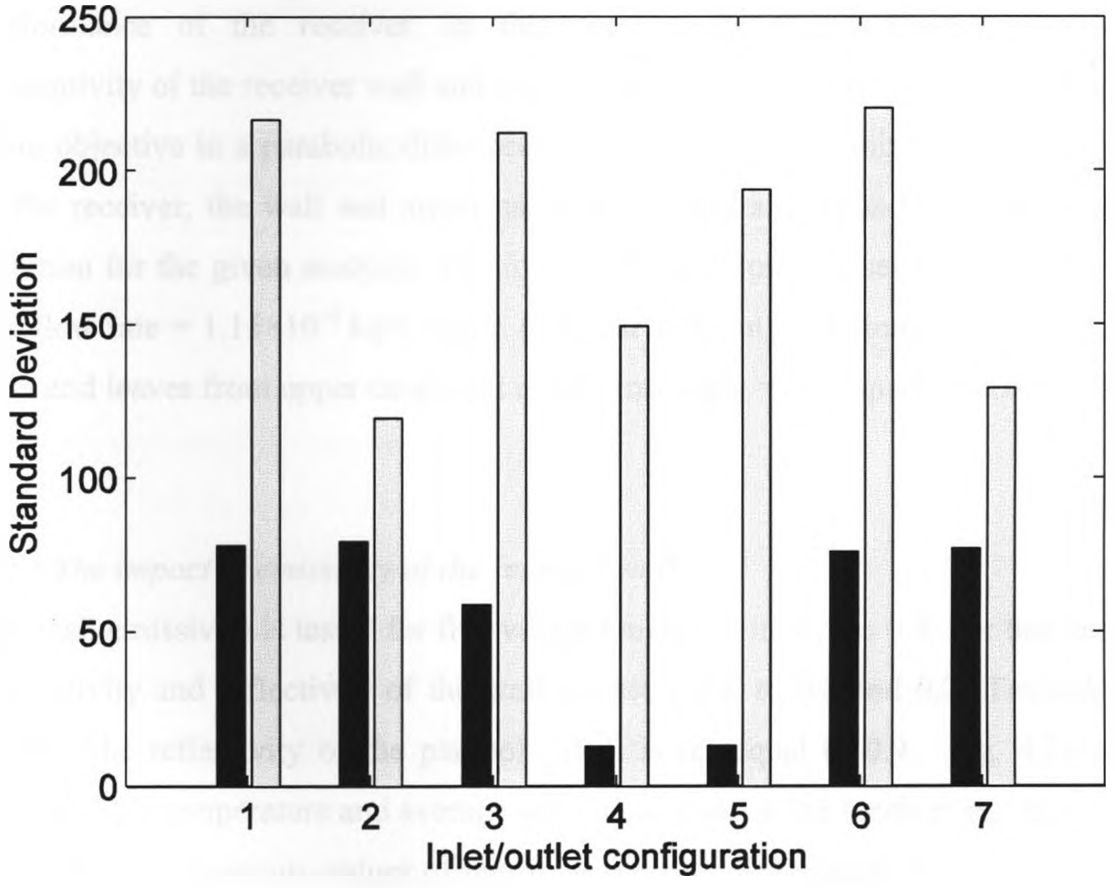

Fig. 4.20: Standard deviation numbers for different inlet/outlet configurations(black bar: wall temperature, white bar: argon temperature).

4.2 Thermal Radiative Properties

Since radiation is a surface phenomenon, the radiative properties of the surface material play a very crucial role in the radiation exchange between the surfaces and the radiation absorbed by the surfaces. As the incident flux on the receiver wall is solely radiative and furthermore, due to the radiation exchange between the walls of the receiver, the radiative properties of the wall of the receiver could have a significant impact on the heat transfer process inside the receiver. The radiative properties of the ceramic materials which are typically recommended as the receiver material are listed in the literature with wide variation. Furthermore, in real applications, these properties may vary with the change in the surface conditions. For example, the reflectivity of the parabolic dish can change due to the environmental conditions such as the dust accumulation on the dish surface. Thus, it is important to investigate the sensitivity of different radiative properties on the thermal performance of the receiver. In this section, the sensitivities of emissivity and absorptivity of the receiver wall and reflectivity of the parabolic dish are analyzed. As the main objective in a parabolic dish-receiver system is to maximize the solar energy input to the receiver, the wall and argon gas temperatures are set as the performance testing criterion for the given analysis. The following conditions are set for this analysis: argon gas flow rate = 1.15×10^{-4} kg/s, argon enters at ambient conditions from lower tangential inlet and leaves from upper tangential outlet, rim angle = 45°, aperture size = 0.025 m.

4.2.1 The impact of emissivity of the receiver wall

The wall emissivity is tested for five values ranging from 0.5 to 0.9. For this analysis, the absorptivity and reflectivity of the wall are set equal to 0.8 and 0.2 [Touloukian et al., 1972]. The reflectivity of the parabolic dish is set equal to 0.9. Fig. 4.21 shows the average wall temperature and average gas temperature in the receiver and at the outlet for five different emissivity values of the receiver wall. The results show that the emissivity of the receiver wall has negligible effect on the thermal performance.

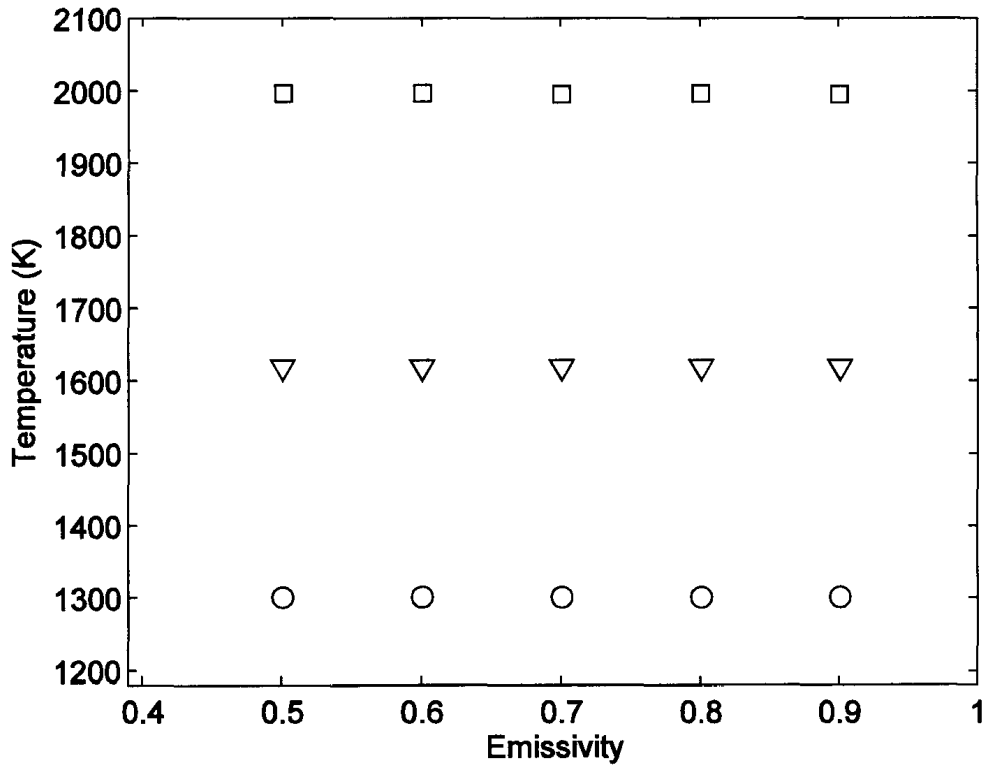

Fig.4.21: Average wall temperature (square), average fluid temperature (circle), and average fluid outlet temperature (triangle) for different emissivity values of the solar receiver wall.

4.2.2 The impact of absorptivity of the receiver wall

The wall absorptivity is tested for five values ranging from 0.5 to 0.9. For this analysis, the emissivity and reflectivity of the wall are set equal to 0.8 and 0.2, respectively. The reflectivity of the parabolic dish is set equal to 0.9. Fig. 4.22 shows the average wall temperature and the average gas temperature in the receiver and at the outlet. The results show that similar to emissivity, the absorptivity of the receiver wall has negligible effect on the thermal performance, even though the average temperatures increase slightly. The negligible effect of radiative properties of the receiver wall could be due to the reason that since the aperture diameter is very small, the re-radiation loss through the aperture is also small and thus, most of the thermal radiation that entered the receiver eventually gets absorbed by the receiver irrespective of the radiative properties of the surface.

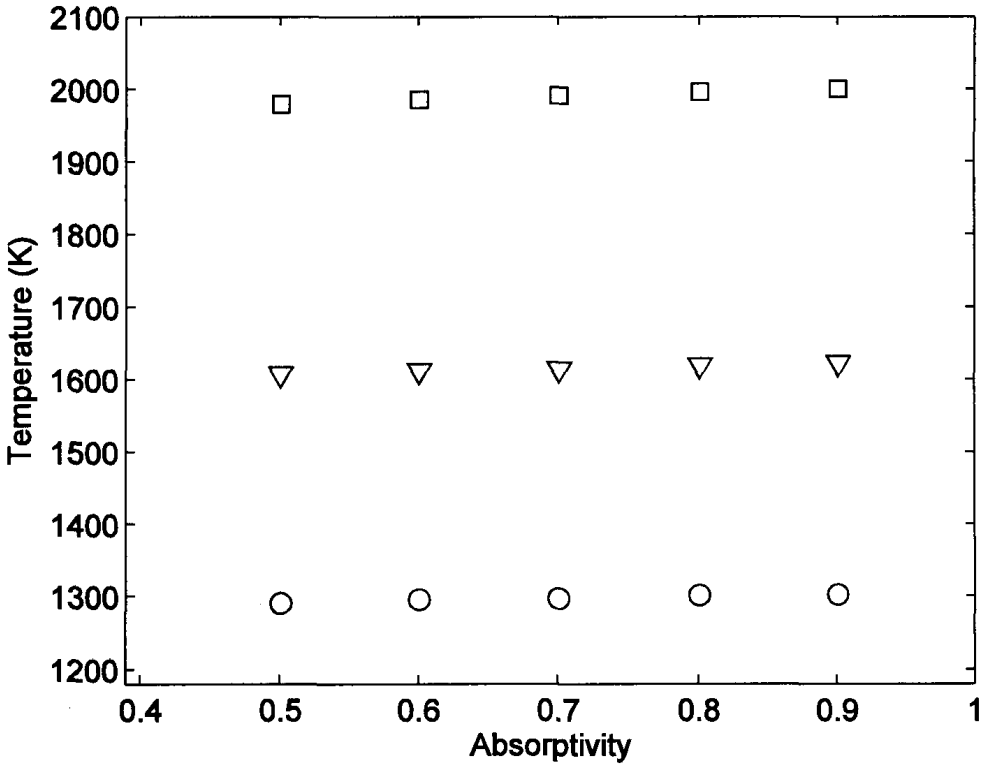

Fig.4.22: Average wall temperature (square), average fluid temperature (circle), and average fluid outlet temperature (triangle) for different absorptivity values of the solar receiver wall.

4.2.3 The impact of reflectivity values of the parabolic dish

The impact of the change in reflectivity of the parabolic dish is investigated for five values ranging from 0.5 to 0.9. For this analysis, the emissivity, absorptivity and reflectivity of the receiver wall are set equal to 0.8, 0.8 and 0.2, respectively. Fig. 4.23 shows the average receiver wall temperature and average temperature of argon in the receiver and at the outlet for different values of dish reflectivity. The plot show that the dish reflectivity has a signficant impact on the receiver's performance. The results indicate that the temperatures of the receiver wall and argon gas increases almost linearly with the dish reflectivity. By decreasing the dish reflectivity from 0.9 to 0.5, the average receiver wall temperature decreased from 2000 K to 1450 K (i.e. by 28%). Similarly, the average argon gas temperature in the receiver decreased from 1300 K to 1000 K (i.e. by

23%). To further investigate the temperature behavior of the receiver wall and argon gas, the circumferentially-averaged temperatures of the receiver wall and argon gas in the receiver are shown in Fig. 4.24 and Fig. 4.25, respectively. Fig. 4.24 shows that the temperatures increase along the wall with an increase in dish reflectivity. It is also found that from 0.12 m to 0.26 m along the wall, the temperatures are almost constant. By increasing the dish reflectivity from 0.5 to 0.9, the peak circumferentially-averaged temperatures of the receiver wall increased from 1487 K to 2033 K (i.e. by 37%) and the peak values occur at approximately 0.14 m along the wall. Fig. 4.25 shows the gradual increase in the gas temperature with the receiver height. Almost the same increasing trend is observed for all cases. The above results show that the reflectivity of the parabolic dish has a significant impact on the thermal performance of the receiver. In practical applications, these parabolic dish systems are installed in open area where they are exposed to dust and other particulates that could deposit on the dish surface and reduce its reflectivity and hence reduces the performance of the dish-receiver system in the long run.

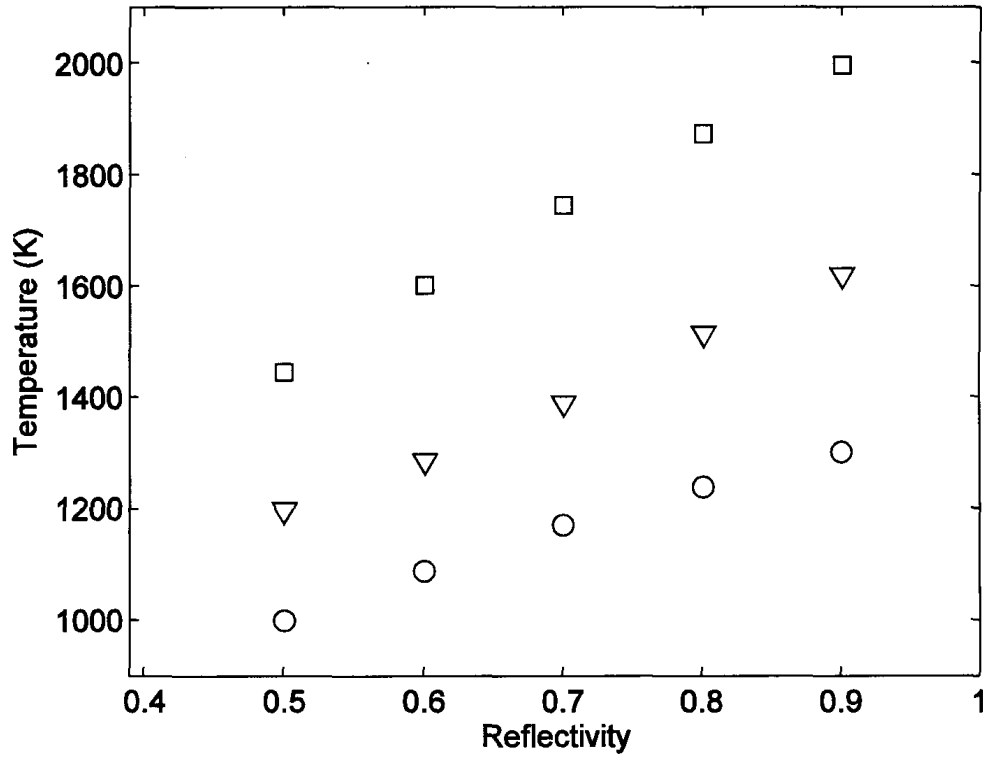

Fig. 4.23: Average wall temperature (square), average fluid temperature (circle), and average fluid outlet temperature (triangle) for different reflectivity values of the parabolic dish.

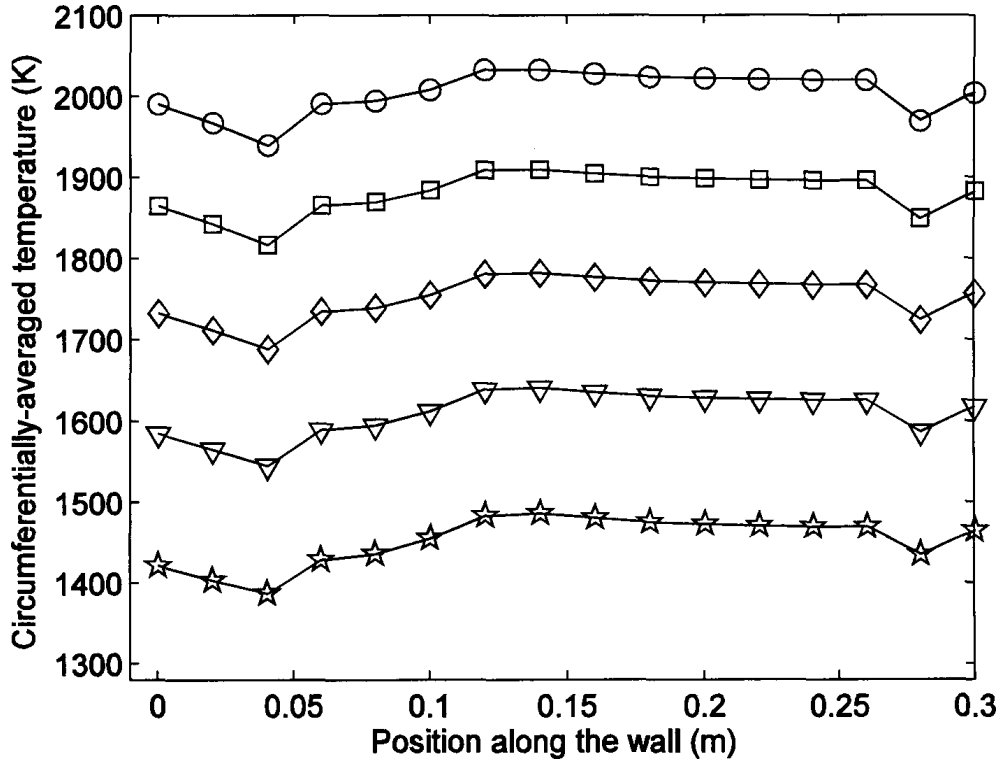

Fig. 4.24: Circumferentially-averaged temperature of the receiver wall for different reflectivity values of the parabolic dish. (Circle: reflectivity=0.9; square: reflectivity =0.8; diamond: reflectivity =0.7; triangle: reflectivity =0.6; star: reflectivity =0.5)

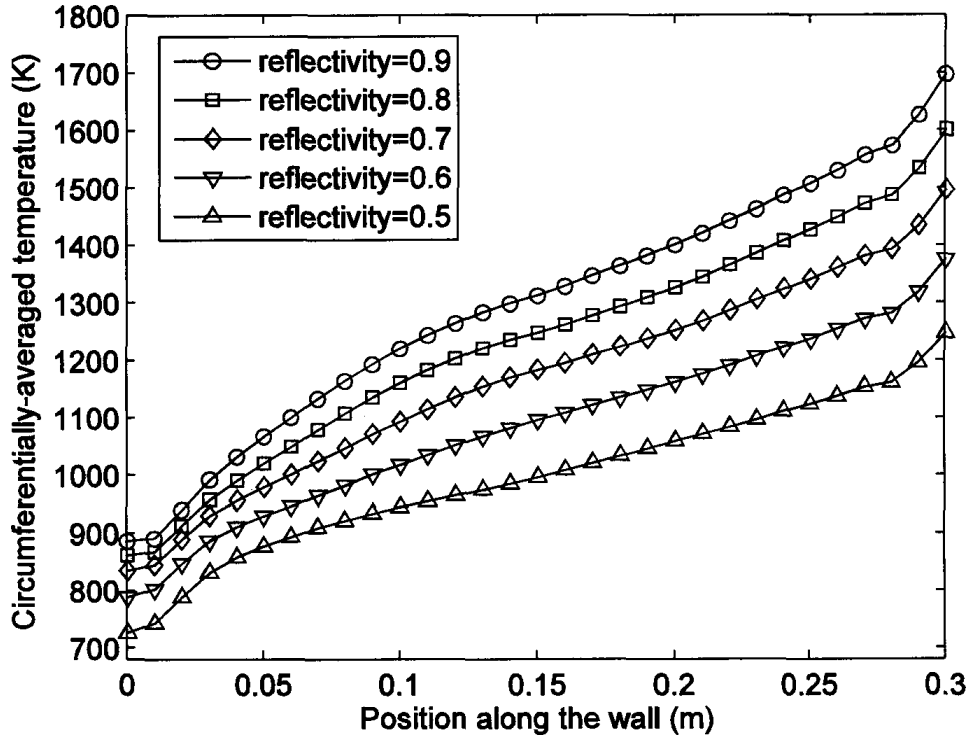

Fig. 4.25: Circumferentially-averaged temperature of argon for different reflectivity values of the parabolic dish.

4.3 Operational Parameters

In the section, the impact of flow rate and pressurization of the argon gas is discussed. In addition, different working fluids such as, steam, helium and air, are taken into consideration and the results are compared with argon. The following parameters are set for this set of simulations: reflectivity of the parabolic dish = 0.9, emissivity of the solar receiver = 0.8, absorptivity of the solar receiver = 0.8, working fluids enter from lower tangential inlet and leave from upper tangential outlet, buoyancy effect is considered, rim angle = 45°, aperture size =0.025 m.

4.3.1 The impact of flow rate

The impact of flow rate was investigated for a range of flow rates from 2.87×10^{-5} to 9.18×10^{-4} kg/s. The corresponding Reynolds numbers based on the inlet ambient conditions are 25 to 811. The circumferentially-averaged receiver wall temperature for different flow rates are shown in Fig. 4. 26. The results show that the wall temperature increases with an increase in the gas flow rate. At the two highest mass flow rates, i.e. 6.88×10^{-4} kg/s and 9.18×10^{-4} kg/s, the gas temperature along the wall shows the same trends with peak values of 1032 K and 933 k, respectively, occurring at 0.12 m along the wall. Whereas the gas temperature at the two lowest mass flow rates, i.e. 2.87×10^{-5} kg/s and 5.74×10^{-5} kg/s, shows the same trend with peak values of 2514 K and 2403 K, respectively, occurring at 0.1 m along the wall. It is also found that by increasing the mass flow rate from 2.87×10^{-5} kg/s to 9.18×10^{-4} kg/s, the peak temperature decrease by 63%.

The circumferentially-averaged values of the argon gas for different flow rates are shown in Fig. 4.27. The results show that the argon gas temperature increases with the receiver height for all cases. However, the temperature magnitude increased with a decrease in the gas flow rate. The results also show that the increase in the gas temperature with respect to the receiver height changes with the flow rate. At the highest flow rate, the gas temperature is increased from the inlet temperature of 300 K to 550 K at the outlet i.e. the temperature is increased by about 85%. Whereas at the lowest flow rate, the gas temperature is increased from the inlet temperature of 300 K to 2200 K i.e. the temperature is increased by a factor of more than 6. The results also show that the

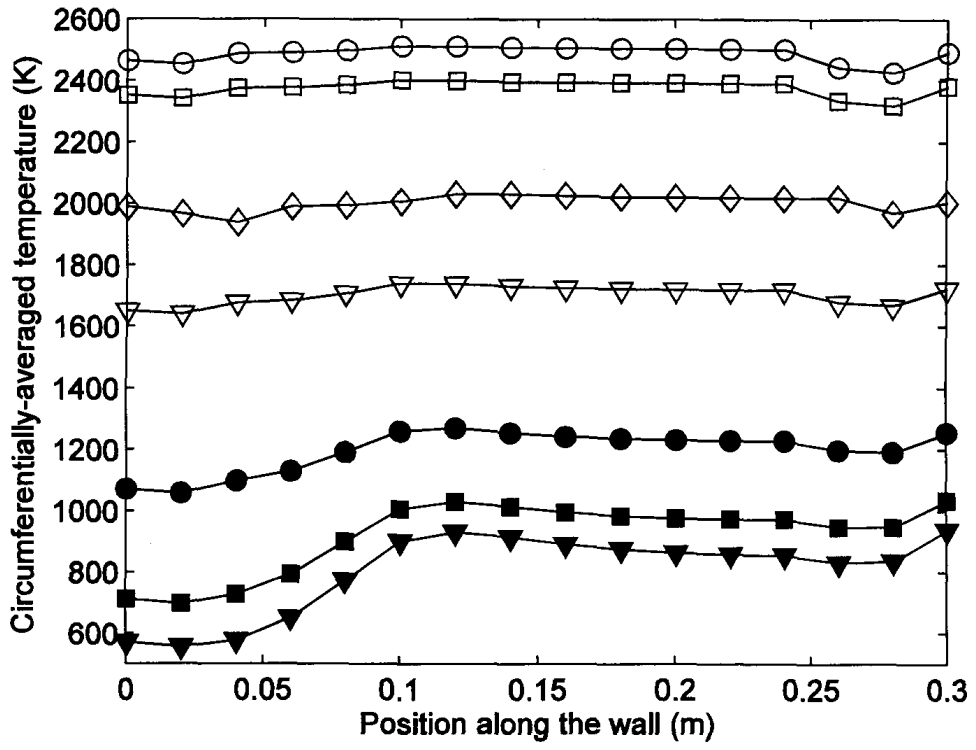

Fig. 4.26: Circumferentially-averaged receiver wall temperature for different flow rates. (Open circle: mass flow rate=2.87×10^{-5} kg/s; open square: mass flow rate=5.74×10^{-5} kg/s; open diamond: mass flow rate=1.15×10^{-4} kg/s; open triangle: mass flow rate=2.29×10^{-4} kg/s; solid circle: mass flow rate=4.59×10^{-4} kg/s; solid square: mass flow rate=6.88×10^{-4} kg/s; solid triangle: mass flow rate=9.18×10^{-4} kg/s)

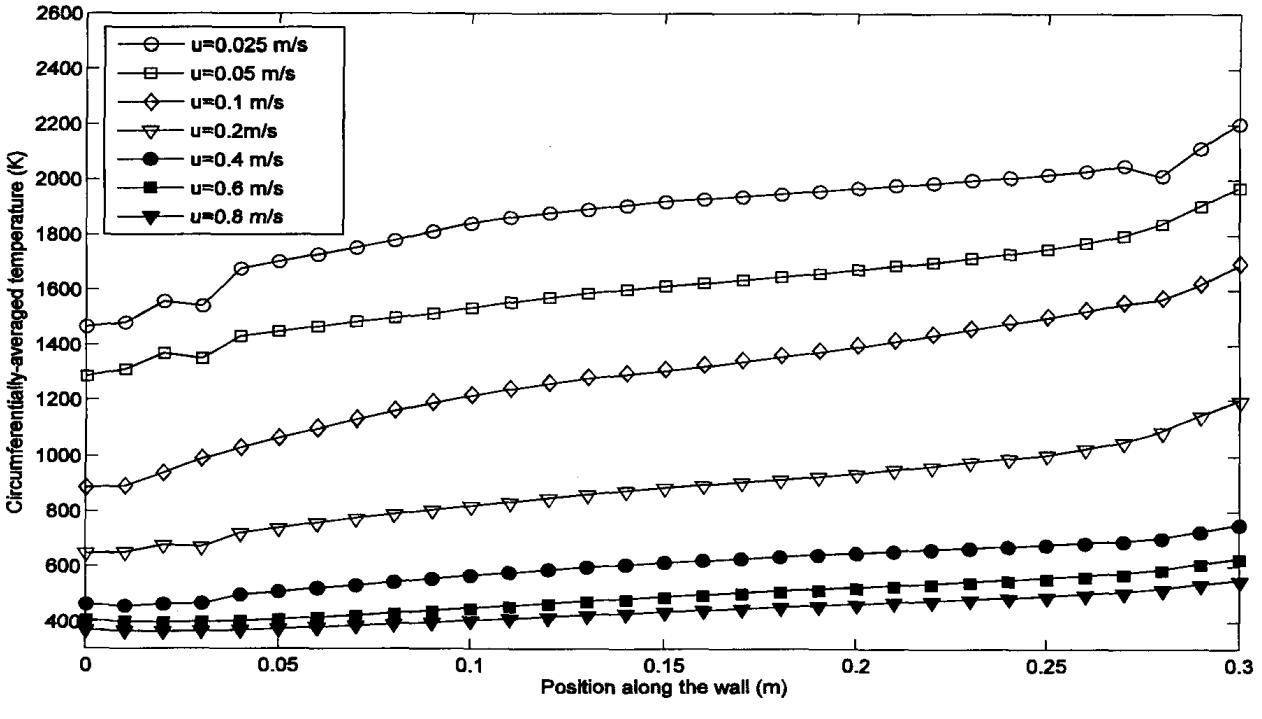

Fig. 4.27: Circumferentially-averaged temperature of the argon gas for different flow rates.

increase in the gas temperature within the bottom region of the receiver is significantly high at the lower flow rate. The average temperature in the bottom region of the receiver increased from 370 K at the highest flow rate to 1470 at the lowest flow rate. Since the buoyancy effects are also significant under these conditions, thus, the heat transfer in the receiver is of mixed convection type.

The average temperature of the receiver wall and the average temperature of argon gas in the receiver and at the outlet for different flow rates are shown in Fig. 4.28. The results show a significant increase in all temperatures with the decrease in flow rate. The results also show that the increase in receiver wall and argon gas temperatures with a decrease in flow rate is exponential. That is, the temperature increases more sharply as the flow rate decreases. As the flow rate decreased from 9.18×10^{-4} kg/s to 2.87×10^{-5} kg/s (i.e. when the flow rate is decreased by 96.9%), the average wall temperature increased by more than a factor of two and the average argon temperature in the receiver increased by more than a factor of three. The results show that at the lowest flow rate of 2.87×10^{-5} kg/s, the receiver wall temperature reaches close to 2500 K and the average gas temperature reaches close to 1900 K.

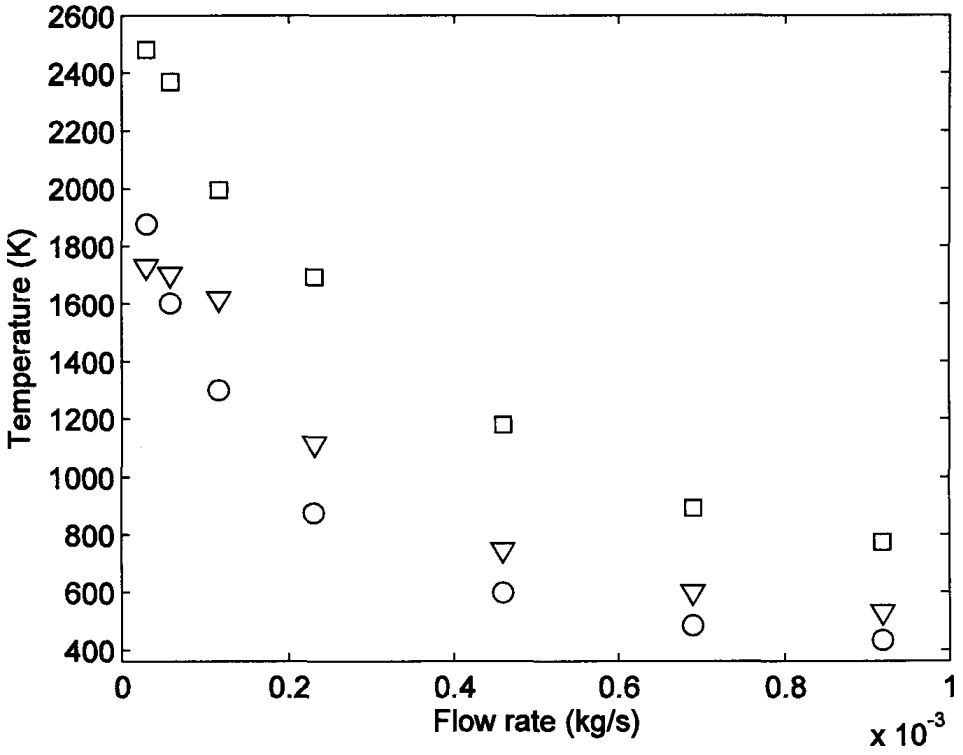

Fig.4.28: Average wall temperature (square), average fluid temperature (circle), and average fluid outlet temperature (triangle) at different flow rate.

The heat gained by the argon gas is computed for different flow rates using the following form of the energy equation,

$$q = \dot{m} c_p (T_{out} - T_{in}) \tag{4.1}$$

The values of heat gain by the argon gas for different flow rates are plotted in Fig. 4.29.

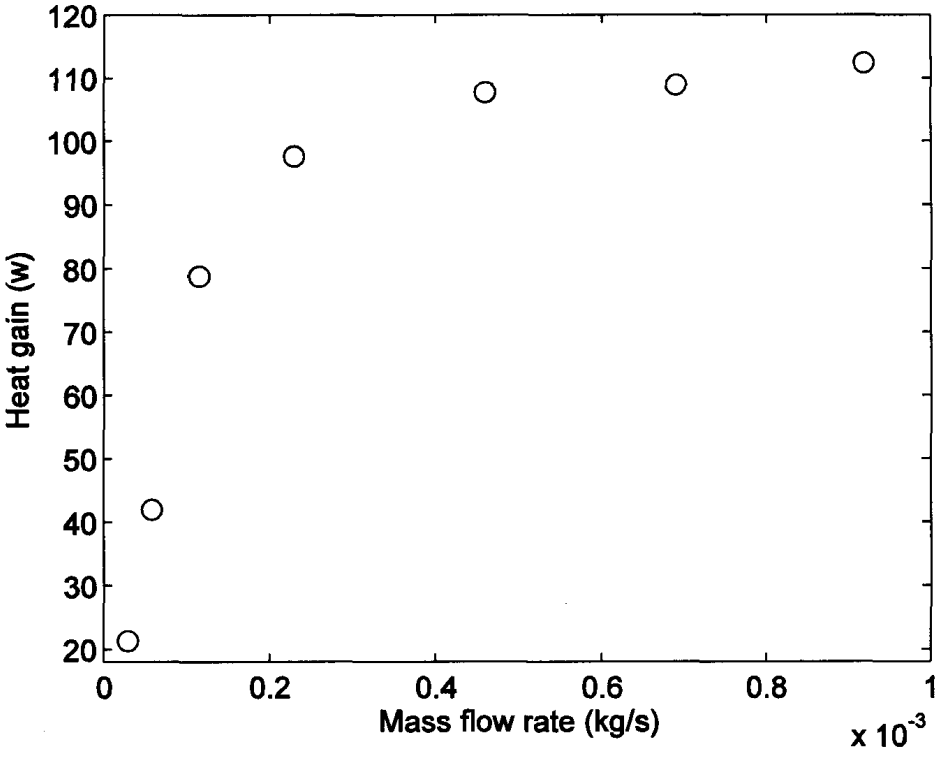

Fig. 4.29: Heat gain by the argon gas for different flow rates

The results show a significant increase in the heat transfer rate with the increase in flow rate. The heat gain increases more sharply as the flow rate increases from 2.87×10^{-5} kg/s to 2.29×10^{-4}. As the flow rate increases from 2.87×10^{-5} kg/s to 9.18×10^{-4} kg/s, the heat gain increases by more than a factor of four. The results also show that the at flow rates higher than 4.59×10^{-4} kg/s, the increase in heat transfer rate is almost negligible. The above results show that the selection of the suitable flow rate in the parabolic dish system depends on its application. If the main purpose of the parabolic dish system is to gain the

heat, then the flow rate has to be increased to a value where the heat transfer rate reaches its maximum value. As the results in Fig. 4.29 shows, further increase in the flow rate will not improve the heat transfer rate but it will increase the pressure losses which will increase the flow pumping cost. If the given dish-receiver system has to be used for thermo-chemical reaction where the high gas temperature is desirable, then the system has to be operated at lower flow rate to achieve the higher gas temperature.

4.3.2 Different working fluids

The impact of different working gases is investigated by considering four gases which are argon, air, helium and steam. The following conditions are considered for these simulations: flow rate of 1.15×10^{-4} kg/s, argon, air and helium entered at the ambient conditions, and steam entered at an initial temperature of 448 K at 1 atm through the lower tangential inlet. The radiative properties of the receiver and dish are kept same as in the previous section. The values of circumferentially-averaged wall temperature for different working gases are shown in Fig. 4.30. The results show that argon gas has the highest wall temperatures and helium has the lowest. It is also found that the wall temperatures of argon, steam and air have same trends with peak temperatures of 2033 K, 1459 K and 1564 K, respectively, occurring at 0.14 m along the wall. The peak temperature of helium occurs at the same position along the wall with a value of 680 K however, its trend is different from that for the other gases. The circumferentially-averaged argon gas temperatures for different gases are shown in Fig. 4.31. The lowest temperature increase in observed for the helium whose temperature increased from 300 K at the inlet to 500 K at the outlet. The air and steam showed a similar behavior up to almost one-third of the receiver height. With a further increase in height, the air temperature increased relatively more than the steam temperature up to the receiver outlet. At the receiver outlet, the temperature of air is about 140 degrees higher than the steam. The increase in temperature of argon is highest among the four gases which increased from 300 K at the inlet to almost 1700 K at the outlet. The specific heats of the gases play an important role in the rise of gas temperature in the receiver. Argon has the lowest specific heat (520 J/kg.K) among these four gases and thus, has the highest

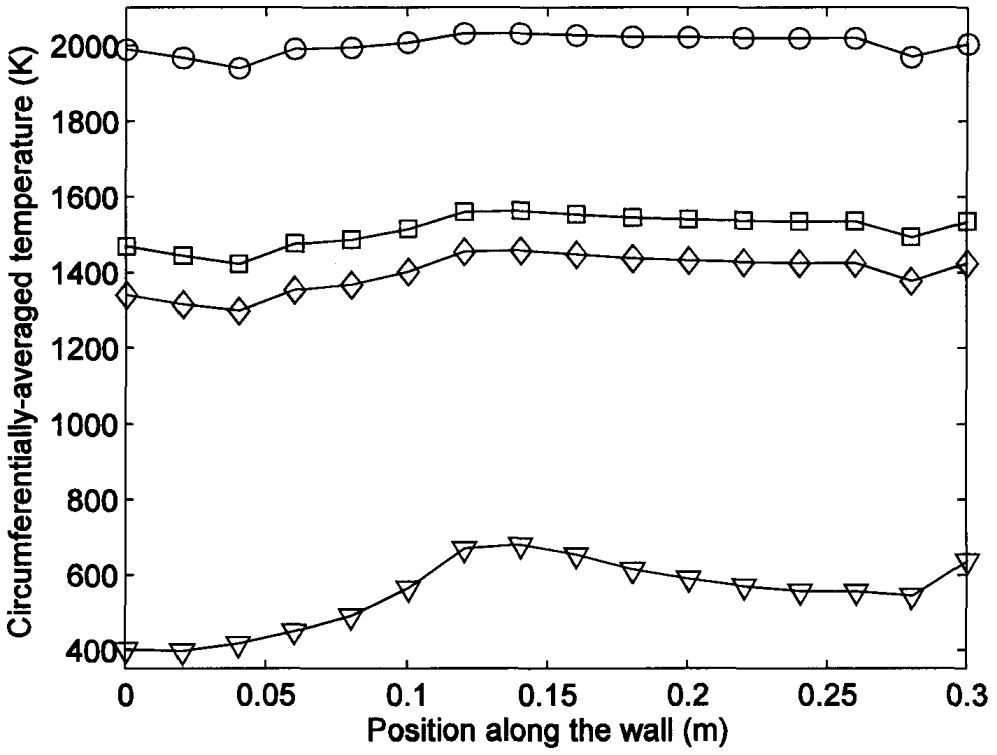

Fig.4.30: Circumferentially-averaged wall temperatures for different working gases. (Circle: argon; square: air; diamond: steam; triangle: helium)

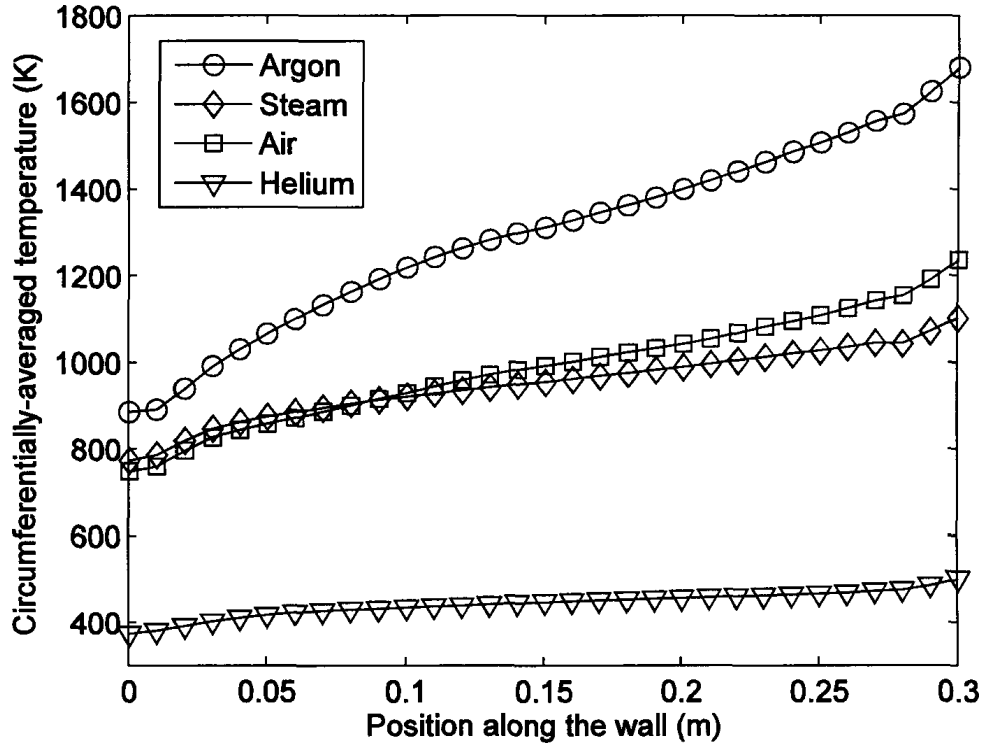

Fig.4.31: Circumferentially-averaged temperatures of different working fluids (water steam enters at 448 K)

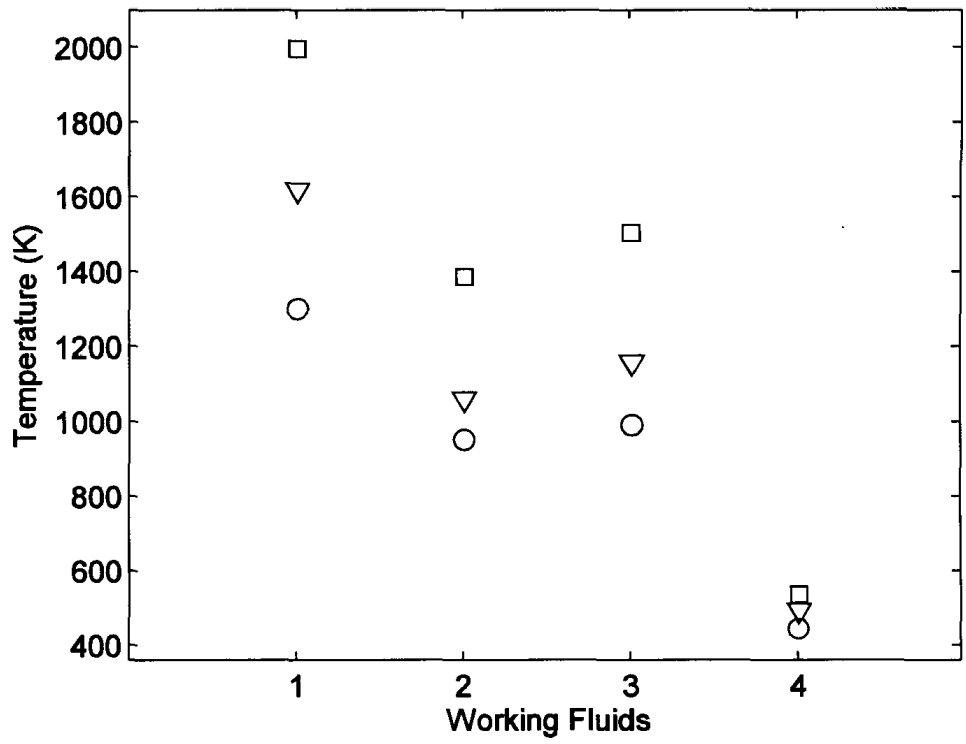

Fig.4.32: Average wall temperature (square), average fluid temperature (circle), and average fluid outlet temperature (triangle) for different working fluids (argon=1, steam@448K=2, air=3, helium=4).

increase in temperature. On the other hand, helium has the highest specific heat (5200 J/kg.K) and thus, has the lowest increase in temperature. The average temperature of the receiver wall and the average gas temperature in the receiver and at the outlet are shown in Fig. 4.32 for all four gases. As the results show, the average wall and gas temperatures are highest for the argon gas which are 73% and 69% higher than helium, 25% and 24% higher than air and 30% and 27% higher than steam, respectively.

The values of heat gain by the all gas are computed using Equation 4.1 and are plotted in Fig. 4.33. The heat transfer rate of steam is highest in four working fluids and argon has the lowest. It is also found that the heat gain of steam is 44% higher than argon. The above results only illustrate the behavior of different gases in a parabolic-dish system under identical conditions. The selection of the suitable working gas is mainly dependent on the nature of the application.

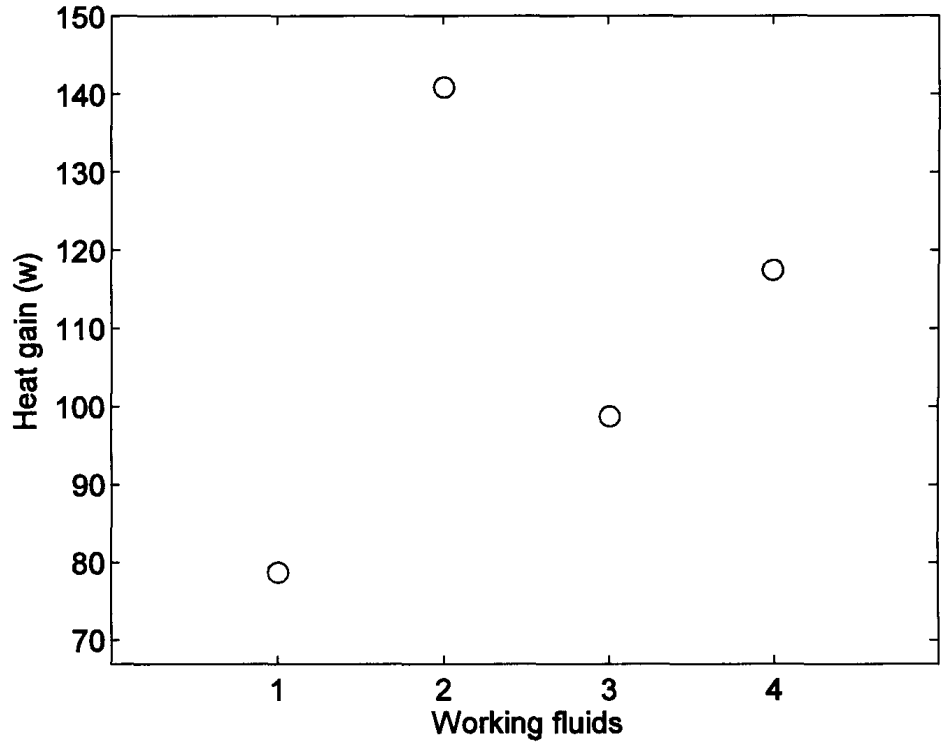

Fig. 4.33: Heat gain for different working fluids (argon=1, steam=2, air=3, helium=4).

4.3.3 The impact of pressurized gas

The impact of gas pressurization is investigated for the inlet gas pressures of 1 atm and 2 atm. Fig. 4.34 shows the temperature distribution of the receiver wall at different pressures. The results show that gas pressure variation has a significant impact on the wall temperature field. The wall temperature tends to decrease substantially with an increase in the gas pressure. The results show that as the gas pressure increased from 1 atm to 2 atm, the overall magnitude of the wall temperature decreased considerably. The results also show that the temperature field in the upper three-quarters of the receiver wall at 2 atm gas pressure is not as uniform as in the case of 1 atm gas pressure. The gas temperature field in figure 4.35 shows similar behavior i.e. the argon gas temperature reduced significantly when it is pressurized. The results show that in the bottom section of the receiver, the gas temperature increased to about 400 K at 2 atm, while in the same region the argon gas temperature increased to 1100 K at the pressure of 1 atm. It is found that by increasing the gas pressure from 1 at m to 2 atm, the average wall temperature and the average argon temperature are reduced by approximately 60% and 64%, respectively.

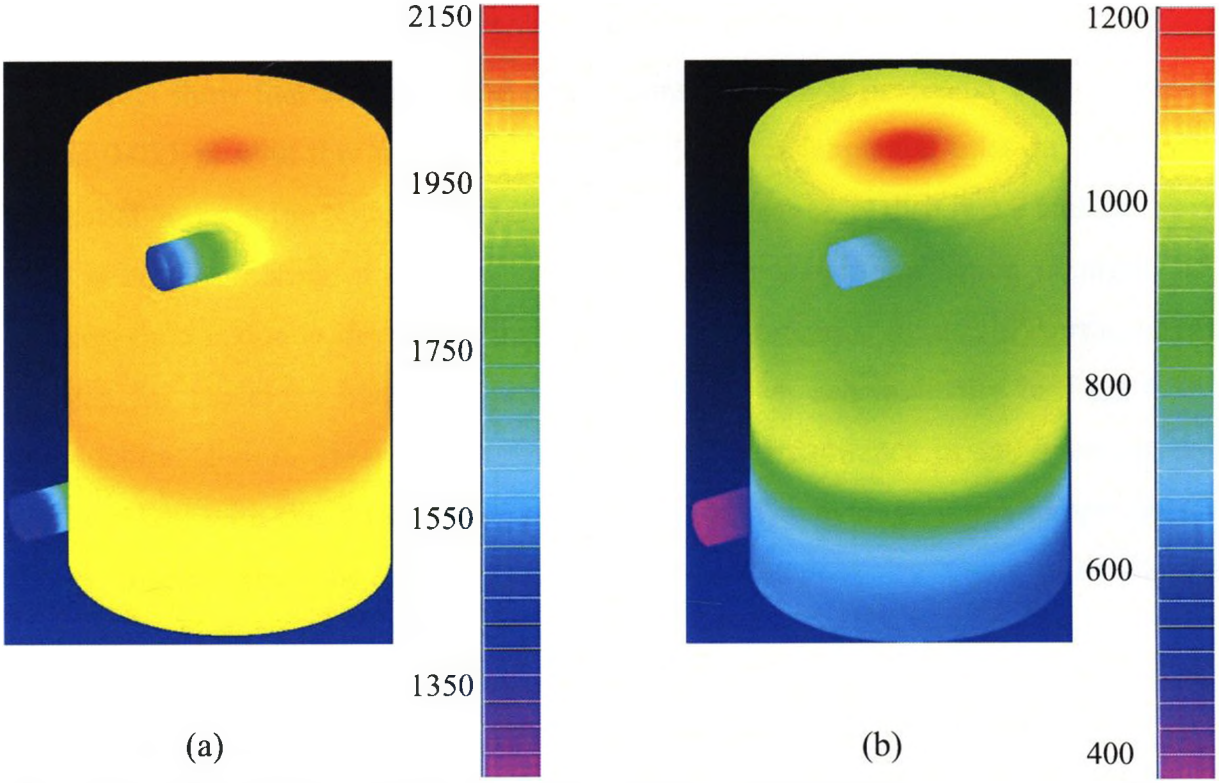

Fig. 4.34: Temperature distribution of the receiver wall at different pressures: (a) 1 atm (b) 2atm. The colorbar is in Kelvin.

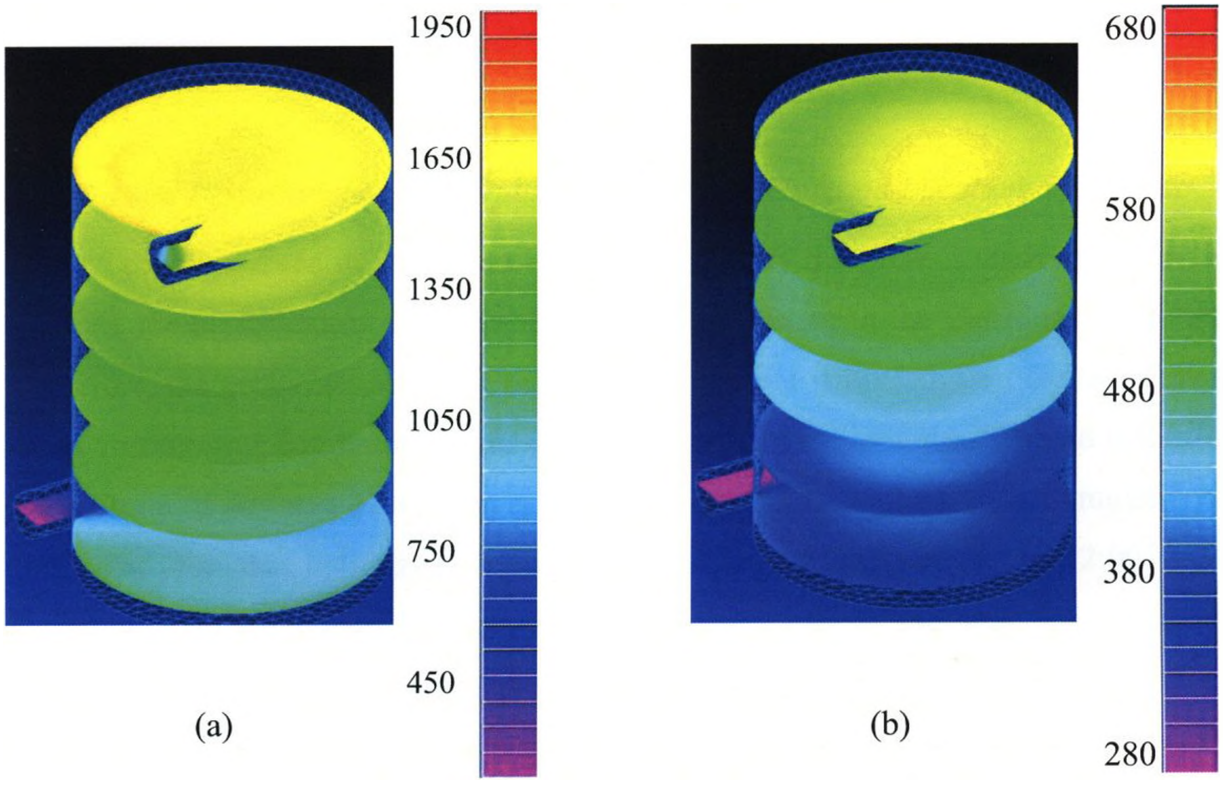

Fig.4.35: Temperature distribution of the argon gas at different pressures: (a) 1 atm (b) 2atm. The colorbar is in Kelvin.

4.4 Optimum Design Configuration

The results show that the optimized design configuration is presented when the aperture size is 0.025 m with the inlet/outlet configuration of a tangential inlet on the top and a tangential outlet at the bottom, the reflectivity of the parabolic dish is 0.9 and the working fluid is argon entering at ambient conditions. Note that the selection of argon as the working fluid is due to the reason that this system is intended for use in thermo-chemical reaction for the clean hydrogen production as shown schematically in Fig.1.5 in the introduction section. Table 4.1 shows the thermal performance of the optimum design configuration with the flow rate of 1.15×10^{-4} kg/s. The average argon temperature is is 16.4% higher than the average temperature calcualted by using the inlet/outlet configuration of a tangential outlet on the top and a tangential inlet at the bottom.

	Average wall temperature (K)	Average argon temperature (K)
Optimized design	2480	2188

Table 4.1 Thermal performance of the optimum design configuration

4.5 Thermal Performance of the Optimized System in Different Locations of Canada

One of the objectives of the overall project of which the present study is a part, is to evaluate the performance of a parabolic-dish CSE system in the Canadian environment. Therefore, the performance of the dish-receiver system is investigated for two Canadian cities Toronto and Edmonton which are located at different latitudes. Toronto is located at the latitude of 43° and Edmonton is located at the latitude of 53°. The simulations are conducted for the optimized design configuration stated above, at 12:00 PM on December 21 (the winter solstice, i.e. the shortest day of the year for the northern hemisphere) and June 21 (the summer solstice, i.e. the longest day of the year for the northern hemisphere). The ambient temperatures of Toronto are set to 293 K in June and 268 K in December, and that of Edmonton are set to 288 K in June and 258 K in December (source: Environment Canada). From Fig. 1.12 in the introduction section, we

can see that Toronto, Ottawa, Winnipeg, Regina, and Calgary are in the region with same amount of solar radiation; also Edmonton, Montreal, Quebec, Fredericton and Halifax are in the region with same amount of solar radiation. Therefore, only Toronto and Edmonton are simulated to represent the two regions with different insolation. The results are summarized in Table 4.2. The results show that Toronto has relatively higher average temperatures than Edmonton, because of higher solar radiation. It is found that, in December, the average wall temperature and the average fluid temperature of Toronto are 19.4%, 21.7% higher than Edmonton, respectively. It is also found that, in June, the average wall temperature and the average fluid temperature of Toronto are 18.3%, 21.6% higher than Edmonton, respectively. Both of the average wall temperature and average fluid temperature in Toronto can achieve approximately 400 K and 200K more than Edmonton in summer and in winter, respectively.

	Average wall temperature (K)	Average fluid temperature (K)
Toronto (Dec)	975	860
Edmonton (Dec)	786	673
Toronto (Jun)	2057	1810
Edmonton (Jun)	1680	1419

Table 4.2 Average wall temperature, average fluid temperature for different locations in canada

CHAPTHER 5: CLOSURE

5.1 Conclusion

A three-dimensional model of parabolic dish-receiver system is developed to simulate the solar energy concentration into the receiver. The model is developed in FEMAP and validated against the experimental data of Melchior et al. [2008]. For the given operating conditions, as the aperture size reduces from 0.05 m to 0.025 m, the average wall temperature, and average argon temperature in the receiver increased by 7.5% and 9.2%, respectively. However, the rim angle of the parabolic dish has no impact on the thermal performance. The configuration with argon coming from the top tangential inlet and leaving from the bottom tangential inlet shows better thermal performance.

The impact of the reflectivity of the parabolic dish, the absorptivity and the emissivity of the solar receiver is also investigated. It is observed that the thermal performance of the solar receiver is sensitive to the reflectivity of the parabolic dish, but insensitive to the absorptivity and the emissivity of the inner wall of the receiver. The results show that the wall and gas temperatures increase almost linearly with the dish reflectivity. By decreasing the dish reflectivity from 0.9 to 0.5, the average receiver wall temperature decreased from 2000 K to 1450 K (i.e. by 28%). Similarly, the average argon gas temperature in the receiver decreased from 1300 K to 1000 K (i.e. by 23%) .

The impact of the mass flow rate of working gas on the system performance is also conducted. The results show an exponential increase in all temperatures with a decrease in the gas flow rate. As the flow rate decreased from 9.18×10^{-4} kg/s to 2.87×10^{-5} kg/s, the average wall temperature increased by more than a factor of two and the average argon temperature in the receiver increased by more than a factor of three. The results show that at the lowest flow rate of 2.87×10^{-5} kg/s, the receiver wall temperature reaches close to 2500 K and the average gas temperature reaches close to 1900 K. Different working fluids, argon, steam, air and helium are simulated. The results show the average wall and gas temperatures are highest for the argon gas which is 73% and 69% higher than helium, 25% and 24% higher than air and 30% and 27% higher than steam, respectively. Much

lower average temperatures for both the wall and the gas are observed when the argon gas at the inlet is at 2 atm, which is not desired in this design. An optimized design configuration of the parabolic dish receiver system is proposed based on the parametric study.

The performance of the optimized parabolic dish receiver system is simulated in two Canadian cities; Toronto and Edmonton.. The results show that the performance of the system is relatively higher in Toronto than in Edmonton. It is also found that, in December, the average wall temperature and the average fluid temperature obtained in the Toronto-based system are 19.4%, 21.7% higher than that in Edmonton, respectively. In June, the average wall temperature and the average fluid temperature of the Toronto-based system are 18.3%, 21.6% higher than Edmonton, respectively. The average wall temperature and the average gas temperature is almost doubled in summer than in winter for both of the cities.

5.2 Contribution

This research on the parabolic dish system was implemented to understand the fundamental thermal-fluids behavior of the solar reactor incorporated with three-dimensional parabolic dish, to advance the methodologies in developing CFD models to simulate solar collector systems, and to improve the design of high thermal efficiency parabolic systems. The specific contributions from the present study are summarized below.

- The first detailed investigation of the thermo-fluid behavior of parabolic dish receiver system in a three-dimensional domain. Another novelty of the present work is that the radiative exchange at the parabolic dish is coupled with the receiver.
- A systematic numerical procedure was introduced to simulate the coupled parabolic dish-receiver system.

- A comprehensive parametric study is conducted to investigate the impact of several geometrical, radiative and operations parameters on the performance of the dish-receiver system.
- An optimal configuration of the system is proposed based on the parametric study.

5.3 Future Recommendation

Some recommendations are listed to further extend this research in the future study:

- Future study is required to simulate large scale systems which can present the available commercialized solar power systems in order to further increase the thermal efficiency and reduce the cost. Large scale CFD model with chemical reactions involved must be conducted to give details on the actual hydrogen production rate.
- Experimental studies are needed to provide benchmark data for the validation of CFD models and also to obtain more realistic insight into thermal-fluids behavior of parabolic dish system.

REFERENCES

Ayoub, J., National survey report of PV power applications in Canada. Natural Resources Canada, Varennes, Quebec, 2006.

Berman, A., Karn, R.K. and Epstein, M., A New Catalyst System for High-Temperature Solar Reforming of Methane, Energy & Fuels, 20, 455-462, 2006.

Eckert, E., and Diaguila, A.J., Convective heat transfer for mixed, free and forced flow through tubes, Trans. ASME, vol. 76, pp. 497-504, 1954.

FEMAP-TMG User's Guide, Maya Inc., 2006.

Fletcher, E.A, and Moen, R.L. , Hydrogen and oxygen from water, Science 197, 1050-1056, 1977.

Fluent 6.3 User's Guide, Fluent Inc., 2006.

Funken, K.H., Pohlmann, B., Lupfert, E., and Dominik, R., Application of concentrated solar radiation to high temperature detoxification and recycling processes of hazardous wastes. Solar Energy 65, 25-31, 1999.

Hirsch, D., Zedtwitz, P. V., and Osinga, T., A new 75 kW high-flux solar simulator for high-temperature thermal and thermochemical research, Journal of Solar Energy Engineering, 125, 117-119, 2003.

Ihara, S., On the study of hydrogen production from water using solar thermal energy. Int.J. Hydrogen Energy 5, 527-534, 1980.

Kreith, F. and Bohn, M.S., "Principles of Heat Transfer", Sixth Edition, Brookes/Cole, Pacific Grove, CA, 2000.

Meier, A., Ganz, J., Steinfeld, A., Modeling of a novel high-temperature solar chemical reactor, Chemical Engineering Science, 51, 3181-3186, 1996.

Melchior, T., Perkins, C., Weimer, A. W., Steinfeld, A., A cavity-receiver containing a tubular absorber for high-temperature thermochemical processing using concentrated solar energy, Int. J. of Thermal Sciences, 47, 1496-1503, 2008.

Nepveu, F., Ferriere, A., Bataille, F., Thermal model of a dish/Stirling systems, Solar Energy, 83, 81-89, 2009.

Noring, J. E., Fletcher, E. A,. High Temperature Solar Thermochemical Processing — Hydrogen and Sulfur from Hydrogen Sulfide. Energy 7, 651-666, 1982.

Palumbo, R., Keunecke, M., Moller, S., Steinfeld, A., Reflections on the design of solar thermal chemical reactors: thoughts in transformation, Energy, 29, 727-744, 2004.
Price, H., Lupfert, E., Kearney, D., Zarza, E., Cohen, G., Gee, R., Advances in parabolic trough solar power technology, Transactions of the ASME. Journal of Solar Energy Engineering, v 124, n 2, p 109-25, 2002.

Shuai, Y., Xia, X.L., Tan, H.P., Radiation performance of dish solar concentrator/cavity receiver systems, Solar Energy, 82, 13-21, 2008.

Steinberg, M., Fossil fuel decarbonization technology for mitigating global warming. Int. J. Hydrogen Energy 24, 771-777, 1999.

Steinfeld, A., Kuhn, P., Reller, A., Palumbo, R., Murray, J., and Tamaura, Y., Solar-processed metals as clean energy carriers and water-splitters. Int. J. Hydrogen Energy 23, 767-774, 1998.

Steinfeld, A., Palumbo, R., Solar thermochemical process technology, Encyclopedia of Physical Science & Technology, R.A. Meyers Ed., Academic Press, 15, 237-256, 2001.
Steinfeld, A., Solar thermochemical production of hydrogen – a review, Solar Energy, 78, 603-615, 2005.

Stephane, A., Patrice, C., Gilles, F., Design and simulation of a solar chemical reactor for the thermal reduction of metal oxides: Case study of zinc oxide dissociation, Chemical Engineering Science, 62, 6323-6333, 2007.

Tiwari, G.N., "Solar energy: fundamentals, design, modeling and applications", Boca Raton : CRC Press ; New Delhi : Narosa, 2002.

Touloukian, Y.S., De Witt, D.P., Thermophysical Properties of Matter, Thermal Radiative Properties: Nonmetallic Solids, vol. 8, IFI/Plenum, New York, Washington, 1972.

Touloukian, Y.S., Powell, R.W., Ho, C.Y., Klemens, P.G., Thermophysical Properties of Matter, Thermal Conductivity: Nonmetallic Solids, vol. 2, IFI/Plenum, New York, Washington, 1970.